Study of the nuclear spin-orientation in incomplete fusion reactions. Measurement of the magnetic moment of the 2^+ states in ^{22}Ne and ^{2} Mg

Amar Boukhari

université PARIS-SACLAY

NNT : 2018SACLS596

Thèse de doctorat

UNIVERSITÉ PARIS SUD
Comprendre le monde, construire l'avenir

Study of the nuclear spin-orientation in incomplete fusion reactions. Measurement of the magnetic moment of the 2^+ states in ^{22}Ne and ^{28}Mg

Thèse de doctorat de l'Université Paris-Saclay
préparée à l'Uniersité Paris-Sud

Ecole doctorale n°576 particules hadrons énergie et noyau : instrumentation, image, cosmos et simulation (Pheniics)
Spécialité de doctorat : Structure et Réactions Nucléaires

Thèse présentée et soutenue à Orsay, le 20/12/2018, par

M. BOUKHARI AMAR

Sous la direction de Dr. GEORGIEV Georgi (Directeur de Recherche, CSMSN, Orsay, France)

Composition du Jury :

Dr. WOLFRAM Korten CEA/IRFU, Saclay, France	Président
Dr. REDON Nadine IPNL, Lyon, France	Rapporteur
Pr. MERTZIMEKIS Theo Université d'Athènes	Rapporteur
Dr. DIDIERJEAN François IPHC, Strasbourg, France	Examinateur
Dr. LJUNGVALL Joa CSNSM, Orsay, France	Co-encadrant de thèse

I am extremely thankful to my Mum and Dad and even that isn't enough.

I especially should many thanks to my dear wife and my son Nazim.

Contents

List of figures

List of Tables

Chapter 1

Introduction

Contents

1.1 Introduction

Atoms are constituted of a small, positively charged, massive nucleus, surrounded by electrons, which are orbiting at the distance of one hundred thousand times greater than the dimension of the nucleus. Nuclei, at the center of the atom, are quantum systems with Z number of protons, N number of neutrons and A = N + Z the total number of nucleons.
The study of nuclear data, which became more numerous and more precise, confirmed that some particular proton and neutron combinations result in nuclei with very high binding energy. Physicists call them magic nuclei [1]. This is the case for nuclei with 2, 8, 20, 28, 50, 82 or 126 protons and/or neutrons. An explanation of these magic number is given by a microscopic approach based on the shell model, which assumes that the nucleus can be described as a few valence nucleons interacting with the mean field created by an inert core formed by the remaining nucleons [2]. Many experimental data that could not be explained by this shell model, were understood by considering the nuclei as an object exhibits a collective phenomena. Nevertheless, the shell model remains one of the essential models used for the description of nuclei up to the intermediate masses.
The unification of the collective models and shell model was possible by the works of Bohr and Mottelson [3], which allowed the interpretation of collective phenomena from the movements of single particles. Just after the developments of the microscopic theory of superconductivity by Bardeen, Cooper and Schrieffer [4], Bohr, Mottelson and Pines finally suggested the analogy between the spectrum of the nucleus and those of superconducting medium [5], involving a component of pairing in the interaction between nucleons within the nucleus. It is therefore relevant to be interested in the way in which the nucleons that compose it interact with each other.
From a theoretical point of view, a microscopic description of nuclear structure and reactions is necessary for the interpretation of the many phenomena in nuclear physics. The fundamental force that glues the nucleons together originates from quantum chromodynamics theory (QCD), which characterizes the strong interaction between the nucleons. However, the exact form of this interaction is not known yet. Studying the nucleon-nucleon interaction, one sees that it is characterized as a repulsive force at short range ~ 0.4 fm (nucleons are kept at certain average separation), and as an attractive force beyond 1 fm. Nucleon-nucleon scat-

tering experiments have been performed to shed light on this interaction. Proton-deuteron scattering experiments allow determining properties of the nucleon-nucleon interaction outside the nuclear medium, or "bare interaction", which we know is different from that inside the nuclear medium with many nucleons. In addition, a description of the nucleus is based on the treatment of N-body problem. Using this nucleon-nucleon interaction in nuclear structure calculations quickly comes up against theoretical and numerical limitations because of the many degrees of freedom to be processed.

Currently, an adequate model to reproduce nuclear phenomena, including the description of the ground states, collective modes, as well as the description of nuclear reactions, is not yet well established. For the medium-to-heavy nuclei, the most successful models allowing the description of nuclear structure and dynamics is the method of the nuclear Energy Density Functional (EDF), also called Self-consistent mean-field [6]. Based on an empirical Energy Functional (for example Skyrme [7] or Gogny [8]), it allows a microscopic description of the collective movements of nucleons within the nucleus and during nuclear reactions.

The stable nuclei on the valley of stability in the chart of nuclides show a certain ratio of protons to neutrons with $N/Z \sim 1.0$ for the lighter nuclei. Nuclei that have an excess of protons or neutrons are unstable and these nuclei are characterized by $N/Z > 1$. Nuclides with $N/Z >> 1$, are called exotic.

The study of these nuclei is of key importance since their properties reveal new and unexpected features that help to deepen our knowledge of the nuclear system. Indeed, the experimental measurements have highlighted the weakening of certain magic numbers and the appearance of new ones in certain regions of the chart of nuclides. One region, where this breakdown occurs is at N = 20 around ^{32}Mg and it is called the "Island of Inversion". Many experiments have studied nuclei at N = 20 in the Island of Inversion, revealing a deviation from the expected systematics, interpreted as a sign of a modification of the N = 20 shell closure. The measurements on ^{32}Mg confirmed this hypothesis. Thus the energy of the first excited state is 885 keV [9], which is very low compared to what is expected for a magic nuclei and suggests that the energy gap is either weakened or has disappeared.

For this reason, the measurement of basic nuclear properties such as masses, nuclear lifetimes, excitation schemes, static and dynamic moments are required. These properties can be compared with theoretical models in order to test these models and improve effective

interactions.

The electromagnetic interaction plays an important role in the investigation of nuclei. A very useful way to study the properties of nuclei by using an electromagnetic interaction is to measure the interaction of their charge and current distribution with a well-known external electromagnetic field. The electromagnetic interaction is very well understood and therefore allows us to make model-independent measurements. Moreover, an electromagnetic "probe" disturbs the nucleus very little because the electromagnetic field has a small influence on the nucleons inside the nucleus.

The measurement of a magnetic dipole moment (μ) involves either the measurement of an interaction energy, $\vec{\mu} \cdot \vec{H}$ (Zeeman effect), of the magnetic moment interacting with an external or internal (hyperfine) magnetic field, or the precession $\Delta\theta = [\vec{\mu} x \vec{B}]dt$ of an aligned nuclear spin (or magnetic dipole moment) in a magnetic field. The quantity that is most often measured is the *g* factor. The *g* factor and the magnetic dipole moment are related by $\mu = gI$, where I is the nuclear spin. The *g* factor is a powerful tool in the study of nuclear excitations, being sensitive to the single-particle configuration of a nuclear state. It reveals what are the configurations and the position of single-particle orbits, and which are nucleons outside the filled shells, and can be used as a rigorous probe to explore the proton-neutron character of the nuclear states.

Forty years ago, *g*-factor measurements of the ground state and of the isomeric states were restricted only to the stable or nuclei close to β-stability line. Those nuclei close to the β-stability line are generally on the neutron-deficient side of the valley of stability, because the production of the nuclei has been done mainly in fusion-evaporation reactions. In the last two decades, this limitation is being overcome through the advent of post-accelerator facilities (such as CERN in Switzerland) producing radioactive ion beams (RIB). It has become possible to explore the regions of the nuclear landscape for beyond the valley of stability. A *g*-factor measurement on exotic nuclei with RIB are more difficult than stable beam measurements. The beam intensity of RIB is orders of magnitude weaker than stable beams. This low intensity lowers the yield of gamma rays and hence increases the statistical uncertainty of the measurement. This problem can be compensated by the use of advanced high-efficiency detector arrays with large solid angle coverage. Furthermore, RIBs can be contaminated with unwanted isobaric ions. Additionally, background radiation arises from the beam stopping

near the detection system. The production and selection of the exotic nuclei of interest in sufficient quantity (> 10^6 pps) has increased the attempts for g-factor measurements and requires new measurement methods. Therefore alternative methods need to be developed.
The measurement of the g factor of a state is based on the interaction of this nuclear moment with a magnetic field. The effect manifests itself as a modification of the angular distribution of the associated radiation. Several methods exist to study the magnetic moment of the state of interest, depending on its lifetime. In this thesis two different techniques are used:

- Time-Differential Recoil-In-Vacuum (TDRIV) for short-lived states (picoseconds),
- Time-Dependent Perturbed Angular Distribution (TDPAD) for relatively long-lived states (a few ns or higher).

While laboratory magnets can provide magnetic fields of the order of Tesla for isomeric states with lifetimes of hundreds of ns or longer, hyperfine magnetic fields are required to provide strong magnetic fields necessary (few KTesla) for lifetimes of the state of interest of the order of picoseconds.
The TDPAD [10] method is used to measure g factor of isomeric states. It has been widely used in fusion-evaporation reactions [10]. The first proof-of-principle TDPAD experiment with a projectile-fragmentation reaction at E_{beam} = 500 MeV/u, was in the case of ^{43m}Sc [11]. A significant amount of alignment was observed.
The first part of my thesis work is focused on the study of the nuclear spin-orientation which can be produced by an incomplete fusion reaction mechanism. The incomplete fusion processes are mainly the heavy-ion interactions that take place around the Coulomb barrier. The advantages of incomplete fusion are the population of higher spin, non-yrast states, few reaction channels opened, and a change of Z between the beam and the products. For that purpose, an experiment has been performed at the ALTO facility in Orsay, France [12]. The aim of this experiment was investigating the nuclear spin orientation in an incomplete fusion reaction using a ^{7}Li beam on a ^{64}Ni target, as well as in transfer reactions (^{7}Li,αpn) and (^{7}Li,αn). In this case, the level of nuclear spin orientation was determined by applying the TDPAD method to isomeric states in ^{65m}Ni, and in ^{66m}Cu.
The second part of my work was dedicated to the measurement of the g factor of the first 2^+ excited state in ^{28}Mg, which would reveal the position of $\nu d_{3/2}$ orbital at N= 16, define

the boundary of the N=20 Island of Inversion and impose a strong test on the shell model. This study will improve our knowledge in this region and opens the way for similar studies towards ^{32}Mg. The experiment was carried out at HIE-ISOLDE at CERN. A neutron-rich ^{28}Mg beam was post-accelerated until the MINIBALL set-up, impinged on a ^{93}Nb target located in the plunger device in the center of the MINIBALL array. The state of interest was populated through Coulomb excitation. In this case, the g factor of the first 2^+ excited state in ^{28}Mg was studied by applying the new TDRIV method, suited for radioactive beams.

1.2 Bibliography

[1] W. Elsasser. *J. de Phys. et Rad*, 5:625, (1934). 2

[2] M. G. Mayer. *Phys. Rev*, 75:1969–1970, (1949). 2

[3] A. Bohr et B. Mottelson. *Nuclear Structure*, 2, (1975). 2

[4] L. Cooper. *Phys. Rev*, 104:1189–1190, (1956). 2

[5] A. Bohr, B. R. Mottelson et D. Pines. *Phys. Rev*, 110:936–938, (1958). 2

[6] M. Bender, P.-H. Heenen et P.-G. Reinhard. *Rev. Mod. Phys*, 75:121–180, (2003). 3

[7] T. Skyrme. *Phil. Mag*, 1:1043, (1956). 3

[8] J. Dechargé et D. Gogny. *Phys. Rev*, C 21:1568–1593, (1980). 3

[9] S. Grevy,S. Pietri et al. *Nucl. Phys. A*, C 21:734,369, (2004). 3

[10] Goldring G and Hass M. *In Treatise in Heavy Ion Sciences*. edited by D.E.Bromley (Plenum Pres, New York) p 539, (1985). 5

[11] Schmidt-Ott W.-D. et al. Spin alignment of ^{43}Sc produced in the fragmentation of 500 MeV/u ^{46}Ti. *Zeitschrift für Physik A Hadrons and Nuclei*, 350:215–219, (1994). 5

[12] G. Georgiev et al. Proposal for experiment : Nuclear moments and nuclear orientation from incomplete fusion and transfer reactions. (2013). 5

Chapter 2

Theoretical background

Contents

2.1 Electromagnetic moments of nuclei

Nuclear electromagnetic moments (EM), i.e., the magnetic dipole and the electric quadrupole moments, are widely used in nuclear physics to study the structure of nuclei. Electric multipole moments provide us with information on the charge density in nuclei. They show the deviation of the nuclear charge from a spherical shape. The information on magnetization densities is provided by the magnetic multipole moments, which reveals the structure of the nuclei. These moments measure the interaction between nucleus and an external magnetic field in much the same way that the static electric moments measure its interaction with an external electric field gradient.

The potential of finite charge distribution at an observation point well outside the region of the nucleus can be expressed as following [1]:

$$\phi(\vec{r}) = 4\pi \sum_{l,m} \frac{1}{2l+1} \left[\int Y^*_{lm}(\theta', \phi') \vec{r'}^{l} \rho(\vec{r'}) d^3 r' \right] \frac{Y_{lm}(\theta, \phi)}{\vec{r}^{l+1}}, \tag{2.1}$$

the vector $\vec{r'}$ indicates the position of an element of charge within the nucleus, where, the vector $\vec{r}$ defines the position of the observation point and θ angle between them, where $Y_{lm}(\theta, \phi)$ are the spherical harmonics and $\rho(\vec{r'})$ is the charge density within the nucleus. The quantities in brackets are the Q_{lm} which are known as the static electric multipole moments of the nucleus,

$$Q_{lm} = \int \vec{r'}^{l} Y^*_{lm}(\theta', \phi') \rho(\vec{r'}) d^3 r' \tag{2.2}$$

The magnetic multipole moments can be defined in an analogous manner as :

$$M_{lm} = \int \vec{r'}^{l} Y^*_{lm}(\theta', \phi') \rho_M(\vec{r'}) d^3 r', \tag{2.3}$$

where the magnetic density is $\rho_M(r) = -\nabla.M(r)$.

By using known properties of the spherical harmonics, one can establish some rules on the measurement of the quantities Q_{lm} and M_{lm}. These selection rules do not allow us to measure the quadrupole moment of nuclear states having I=0 or 1/2. As well, the parity of electric moments is defined as $(-1)^l$ while the parity of the magnetic moments is defined as $(-1)^{l+1}$, where l is the order of the moment (l=0 for monopole, l = 1 for dipole, l = 3 for octupole, and l = 4 for hexadecapole, etc.). Thus static electric moments is given only for even l and magnetic moments for odd l.

2.1.1 The nuclear magnetic dipole moment

Classically, the magnetic dipole moment, μ, is defined as the vector product of a current i and enclosing area A the charge circulates. The magnetic dipole moment of the nucleus is induced from the current of the orbital angular momentum of the protons of mass m in the nucleus. Where the protons were moving in circle of radius r with a velocity v, the moment is given by:

$$|\vec{\mu}| = i\mathrm{A} = \frac{e}{2\pi r/v}\pi r^2 = \frac{evr}{2} = \frac{e}{2m}|\vec{l}|, \tag{2.4}$$

where $|\vec{l}|$ is the classical angular momentum with $|\vec{l}| = \vec{r} \times \vec{p} = mvr$. The magnetic moment, in a quantum system, is defined with respect to the direction of the greatest component of l, the moment is defined via the z axis where it has a maximum projection, $|\vec{l_z}| = m_l\hbar$, with $m_l = +l$.

$$\mu = \frac{e\hbar}{2m}\vec{l} \tag{2.5}$$

The unit $e\hbar/2m$ is named as the nuclear magneton (μ_N) if m corresponds to the proton mass, and the Bohr magneton (μ_B) if m is the electron mass. These units have a numerical values $\mu_N = 5.05084 \times 10^{-27}$ J/T and $\mu_B = 9.27408 \times 10^{-24}$ J/T. One can note, from the numerical values, that $\mu_N \ll \mu_B$ because of the difference of the masses.
In order to compare with experimental results, Equation (2.5) can be rewritten as :

$$\mu_l = g_l l \mu_N, \tag{2.6}$$

where g_l is the orbital gyromagnetic ratio and l is the orbital angular momentum in units of $\hbar$. The orbital g factor of the electron is g_l = -1. The free proton orbital gyromagnetic factor is g_l^π = +1. The neutrons have zero electrical charges thus there is no orbital magnetization, g_l^ν = 0. Otherwise, the intrinsic spin s=1/2 of the nucleons induces their own intrinsic magnetic field. The intrinsic magnetic dipole of the nucleons is given in terms of their spins by:

$$\mu_s = g_s s \mu_N, \tag{2.7}$$

where g_s is the spin gyromagnetic ratio and s is the intrinsic spin in units of $\hbar$. Protons, neutrons, and electrons are described within Dirac theory, if they are elementary particles the g_s should be g_s^π = 2, g_s^e = -2, and g_s^ν = 0 for protons, electrons and neutrons respectively. For electrons, the measurement is in agreement with g_s value equal to -2.0023. However, the free

proton and neutron gyromagnetic factors have been measured experimentally with resulting g_s^{π} = 5.5845 and g_s^{ν} = -3.8263. It is therefore evident that the nucleons are not fundamental particles, unlike electrons, and today they are understood to be composed of three quarks.
The measurement of the sign and the magnitude of the g factor provides useful informations. The sign of g_s changes depending on whether the particle is a proton or neutron, this information can show which particle is dominating the nuclear structure. Where the magnitude of the g-factor depends on the contributions of the protons and neutrons to the wavefunction of nuclear state.
Being sensitive to the configuration mixing of the wave function, a measurement of a nuclear g factor plays an important role in the understanding of nuclear structure.
The magnetic dipole moment of a particular state of a nucleus consisting of A nucleons is of resulting from the contribution of the magnetic moments of A nucleons :

$$\mu = \sum_{i=1}^{A} (g_l^i \vec{l}_i + g_s^i \vec{s}_i)\mu_N, \tag{2.8}$$

where $\vec{l}_i$, $\vec{s}_i$, g_l^i and g_s^i are the orbital and spin angular momentum, the orbital and the spin gyromagnetic ratios for i^{th} nucleon, respectively. Due to N − N pairing, the magnetic dipole moment of the ground state of even-even nuclei is equal to be zero. In odd-A nuclei the unpaired nucleon contribute mainly in determination of the magnetic dipole moment, if the unpaired nucleon is a neutron, there is only a spin contribution to the moment while if it is a proton there is both a spin and an orbital contribution.
One can rewrite the Equation (2.8) using the isospin formalism in the following way:

$$\mu = \sum_i \frac{1+\tau_z}{2}\vec{l}_i + \left(\frac{1+\tau_z}{2}g_{\pi}^s + \frac{1-\tau_z}{2}g_s^{\nu}\right)\vec{s}_i. \tag{2.9}$$

Putting in numerical spin g factor values, we obtain:

$$\mu = \left[\frac{1}{2}\sum_i^A (\vec{l}_i + \vec{s}_i) + 0.38\sum_i^A \vec{s}_i\right] + \left[\frac{1}{2}\sum_i^A \tau_z(\vec{l}_i + 9.41\vec{s}_i)\right], \tag{2.10}$$

where the isospin operators τ_z for protons and neutrons are $\tau_z^{\pi} = +1$ and $\tau_z^{\nu} = -1$.
To sum up, the magnetic dipole operator μ is one-body operator and the magnetic moment of a nucleus for a nuclear state $|IM\rangle$ with angular momentum I can be obtained by detemining the value of the z component of the operator in the magnetic substate M = I:

$$\mu = \langle I, M = I | \vec{\mu}_z | I, M = I \rangle . \tag{2.11}$$

And,

$$\vec{\mu} = g_I I \mu_N, \tag{2.12}$$

where μ is given in the units of nuclear magnetons μ_N and the angular momentum I is given in the units of $\hbar$.

2.1.1.1 Magnetic moments of Odd-mass nuclei

The borders of doubly-magic nuclei are often referred as the extreme single particle shell model since the model includes a single particle or a single hole outside a closed-shell core. Many nuclear properties for the ground state and low-energy excited states are predicted correctly by the model by assuming a single unpaired nucleon coupled to an inert core. The single particle magnetic moment of such a nuclear state with its valence nucleon can be evaluated using Equation (2.8) and Equation (2.11). Assuming a single nucleon moving in a potentiel generated by all other nucleons which are coupled to spin 0. The nucleon in mention has an orbit with orbital angular momentum l and that its spin s couples to form a total angular momentum j ($\vec{j} = \vec{l} + \vec{s}$). We obtain:

$$\mu = \langle \mu_z \rangle = g_l j + (g_s - g_l) \langle s_z \rangle . \tag{2.13}$$

The expectation value of $\langle s_z \rangle$ gives:

$$\langle s_z \rangle = \frac{j}{2j(j+1)} \left[j(j+1) - l(l+1) + s(s+1) \right] \hbar. \tag{2.14}$$

Substituting Equation (2.14) into Equation (2.13). We obtain:

$$\begin{aligned} \mu(l+1/2) &= \left[(j - \frac{1}{2}) g_l + \frac{1}{2} g_s \right] \mu_N, \\ \mu(l-1/2) &= \frac{j}{j+1} \left[(j + \frac{3}{2}) g_l + \frac{1}{2} g_s \right] \mu_N. \end{aligned} \tag{2.15}$$

These values are known as the Schmidt limits or Schmidt moments. We show in Figure(2.1) the Schmidt diagrams, where the magnetic moment depends directly on the angular momentum j. The full lines in these diagrams represent the Schmidt values for the magnetic moments as derived from Equation (2.15) by inserting the appropriate values for the g factors. If we compare the experimentally determined magnetic moments, for nuclei having one valence nucleon, with Schmidt limits one can see that the experimental values always

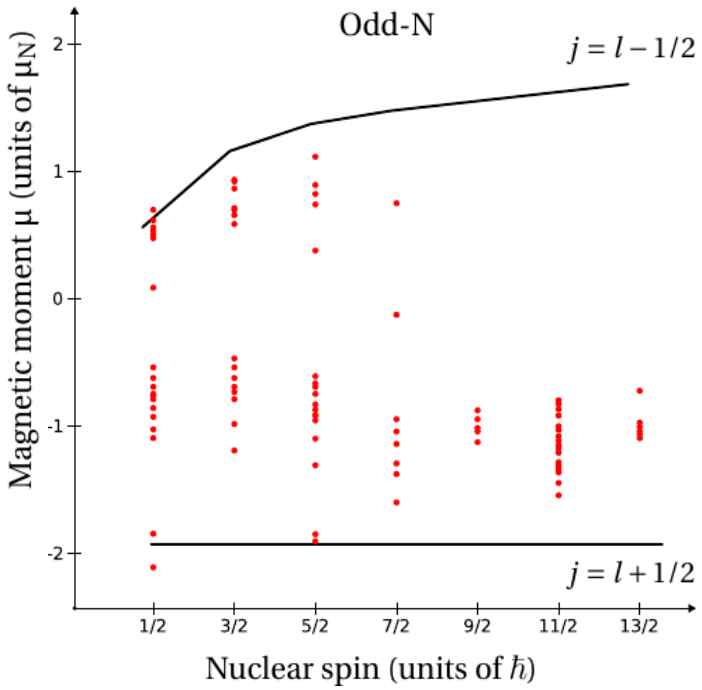

Figure 2.1 – Schmidt diagrams for odd-neutron nuclei, as a function of angular momentum. The dots are the experimentally measured values.

are between and/or more or less on Schmidt limits, but do not coincide with them exactly. Even if the single particle model can account for the general dependence of the moments on j, its fails to explain why the observed values of moments do not coincide with those obtained by the single-particle model. In a real nucleus, the magnetic moment of nucleons are influenced by the presence of other nucleons and give a different value from the free nucleon hypothesis[2][3]. Therefore the single particle moment for a nucleon in a particular state can be calculated using effective single nucleon moments. Usually, effective g factor are used to provide a correction for missing interactions.

Let us now proceed to estimate the magnetic moment of two or more particle states outside an inert core. If we consider two particles with angular momenta I_1 and I_2 coupled to the inert core with $I_{core} = 0$. The total angular momentum is given by the sum of these two angular momenta : $\vec{I}=\vec{I_1}+\vec{I_2}$. If we substitute the total angular momentum I with relation Equation (2.12) in Equation (2.11), we obtain:

$$\mu = \langle IM|g_1 I_{1z} + g_2 I_{2z}|IM\rangle_{M=I}, \tag{2.16}$$

where g_1 and g_2 are the g factors of the two nucleons. If the interaction between the two particles is neglected, the magnetic moment and g factor can be rewritten using the generalized Landé formula [4] as :

$$\mu = \frac{\langle IM|g_1 I_1 \cdot \vec{I} + g_2 I_2 \cdot \vec{I}|IM\rangle_{M=I}}{I(I+1)} \langle IM|I_z|IM\rangle_{M=I}, \tag{2.17}$$

$$g = \frac{\langle IM|g_1 I_1 \cdot \vec{I} + g_2 I_2 \cdot \vec{I}|IM\rangle_{M=I}}{I(I+1)}. \tag{2.18}$$

The evalution of the matrix element of $\vec{I_1} \cdot \vec{I}$ and $\vec{I_2} \cdot \vec{I}$ is performed as follow:

$$\begin{aligned} \vec{I^2} = (\vec{I_1} + \vec{I_2})^2 = \vec{I_1^2} + 2\vec{I_1} \cdot \vec{I_2} + \vec{I_2^2}, \\ \vec{I_1} \cdot \vec{I_2} = \frac{1}{2}(\vec{I^2} - \vec{I_1^2} - \vec{I_2^2}), \\ \vec{I_1} \cdot \vec{I} = \vec{I_1} \cdot (\vec{I_1} + \vec{I_2}) = \vec{I_1^2} + \vec{I_1} \cdot \vec{I_2}. \end{aligned} \tag{2.19}$$

from which one can derive:

$$\begin{aligned} \vec{I_1} \cdot \vec{I} = \frac{1}{2}(\vec{I^2} + \vec{I_1^2} - \vec{I_1^2}), \\ \vec{I_2} \cdot \vec{I} = \frac{1}{2}(\vec{I^2} + \vec{I_2^2} - \vec{I_2^2}). \end{aligned} \tag{2.20}$$

Substituting this into Equation (2.18), we find:

$$g = \frac{g_1 [I(I+1) + I_1(I_1+1) - I_2(I_2+1)]}{I(I+1)} + \frac{g_2 [I(I+1) + I_2(I_2+1) - I_1(I_1+1)]}{I(I+1)}, \tag{2.21}$$

which can be written as:

$$g = \frac{1}{2}(g_1 + g_2) + \frac{1}{2}(g_1 - g_2)\frac{I_1(I_1+1) - I_2(I_2+1)}{I(I+1)}. \tag{2.22}$$

This relation is called the additivity relation.

The second part of the Equation (2.21) vanishes when the two particles occupy two levels with same g factors. In that case, the g factor will be independent of the total spin.

2.2 The hyperfine interaction

The hyperfine interactions is defined as the interaction of the nuclear charge and current distribution of the nuclei with electromagnetic fields in its immediate surroundings. These

interactions influence the atomic and nuclear energy levels. At the atomic level, the magnetic dipole interaction between the nuclear moments and the fields induced by the electrons will give rise to the hyperfine splitting of the electronic states. The hyperfine interaction is defined as a coupling between the atomic spin $\vec{J}$ to the nuclear spin $\vec{I}$ and gives the total spin $\vec{F} = \vec{I} + \vec{J}$, as shown in Figure(2.2).

At nuclear level as illustrated in Figure (2.3), the Zeeman splitting is induced by the mag-

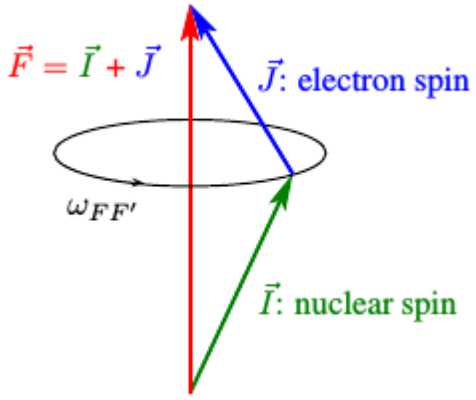

Figure 2.2 – A schematic drawing illustrating a vector model of the free-ion hyperfine interaction.

netic dipole interaction with a magnetic field. This hyperfine interaction is observed in the response of the nuclear spin system to the internal electromagnetic fields of the medium or the applied electromagnetic fields.

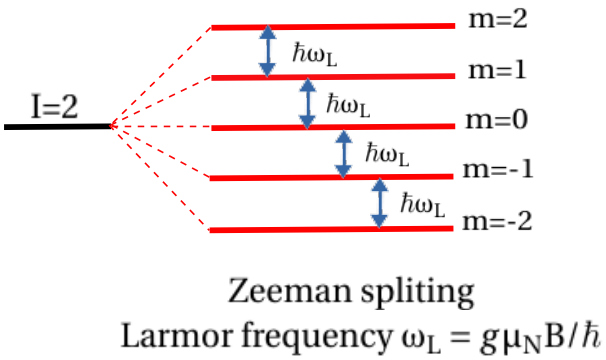

Figure 2.3 – A schematic drawing illustrating the Zeeman splitings with a Larmor frequency $\omega_L = g\mu_N B/\hbar$

When the atoms are implanted into a crystal with a cubic lattice structure and the nucleus

is positioned on one of its regular lattice position, the magnetic substates m of a nucleus with a spin I remain degenerate.
The magnetic field within medium causes the rise of m-degeneracy of the nuclear energy levels. This field can be achieved by applying an external field, of the order of a few hundred Gauss up to sevral Tesla, or via the hyperfine magnetic field of a host material, of the order of ten to hundred Tesla [5].

The interaction of the nuclear magnetic moment μ with a static magnetic field $\vec{B}$ is defined by the Zeeman Hamiltonian [6]:

$$H_B = -\vec{\mu} \cdot \vec{B} = -\frac{g\mu_N}{\hbar}\vec{I} \cdot \vec{B} = -\omega_L I_Z, \tag{2.23}$$

with $\omega_L = g\mu_N B/\hbar$ being the Larmor frequency and g is the nuclear g factor. The magnetic field $\vec{B}$ is defined in a reference frame with the z-axis ($\vec{B} = B\vec{e_z}$). The energy splitting of the Zeeman levels is propotional to m as defined in Equation (2.24). The substates of m of the spin operator are eigenstates of the Zeeman Hamiltonian.

$$E_m = -\hbar\omega_L m. \tag{2.24}$$

The Zeeman splitting levels are equidistant and propotional to the Larmor frenquency. As a descriptive picture, the splitting can be visualized as a precession of the spin I around the magnetic field direction $\vec{B}$ with a Larmor frequency ω_L.

2.3 Nuclear spin orientation

During any nuclear reaction mechanism, a spin-oriented ensemble of the nuclear states is formed to a preferential direction in space, the $|Im\rangle$ states are unequally populated. To study a spin-oriented ensemble, we deal with the angular distribution of γ-rays emitted from oriented states which are formed by nuclear reactions and also with particle-γ angular correlations. Usually, the measurement of γ-rays distributions and particle-γ correlations are used to assign the multipolarities of the γ-rays transitions, and therefore the spin of excited states. They also allow to estimating the mixing ratios of mixed multipolarity γ-ray transitions. But, one needs enough orientation in the excited state of interest to be able to distinguish between

different multipolarity transitions [7].

Let us consider a system of three groups, the original oriented state is denoted as I_0, the initial and final states are denoted as I_i and I_f, respectively. The initial oriented state is usually described by the orientation parameter B_k, however, if the orienting interaction lacks axial symmetry, it can be described by the general statistical tensors ρ_{kq} (See section 2.3.1.1). In the case of unobserved radiations between the I_0 and I_i, the orientation of the I_i is determined by a modification of I_0 with de-orientation coefficients U_k (See 2.3.1.4). In other hands, if the intermediate states between I_0 and I_i are sufficiently long lived, a perturbation of the angular distribution can take place by modification of the orientation by the direct interaction of the electromagnetic moments of that state with the nuclear environment. The perturbation coefficients are represented as G_k (See section 2.3.2.1).

2.3.1 Angular distribution of γ-rays

The angular distribution of a radiation emitted by an oriented state ensemble of I_i is given using the following expression:

$$W(\theta,\phi) = \sqrt{4\pi}\sqrt{2I_i+1}\sum_{k,q}\frac{\rho_{kq}(I_i)A_kY_{kq}(\theta,\phi)}{\sqrt{2k+1}}, \tag{2.25}$$

where $\rho_{kq}(I_i)$ are statistical tensors, A_k are the angular distribution coefficients and $Y_{kq}(\theta,\phi)$ are the spherical harmonics and the angles θ and ϕ are the direction of emission of the radiation.

In the case of an axially symmetric oriented state, Equation (2.25) is reduced to the most frenquently used form of the angular distribution at an angle θ with respect to the beam axis and has the form [8]:

$$W(\theta) = \sum_{k,q} B_k(I_i)A_kP_k(cos\theta). \tag{2.26}$$

The B_k coefficients are orientations parameters which depend on spin of the initial state to which the nucleus is excited, I_i. The angular distribution coefficients A_k depend on I_i, I_f and the multipolarity, which may be pure or mixed. The $P_k(cos\theta)$ are the Legendre polynomials. The γ-ray angular distribution is symmetric about $\theta = 90°$. Only the even-ranked

$P_k(cos\theta)$ are symmetric about $\theta = 90°$. Hence, the angular distribution is valid only for even values of k.

2.3.1.1 Statistical tensors

The non-axially symmetric orientation of the initial state is described by using the density matrix, which is propotional to the statistical tensor. The density matrix formalism is:

$$\rho_{mm'} = \langle m|\rho|m'\rangle\,, \tag{2.27}$$

where m is the projection of the nuclear spin I_i on a z-axis. Using the density matrix, a statistical tensor is given by the formula [9]:

$$\rho_{kq} = \sqrt{2I_i+1}\sum_{m,m'}(-1)^{I_i+m'}\begin{pmatrix} I_i & k & I_i \\ -m' & q & m \end{pmatrix}\langle m|\rho|m'\rangle\,, \tag{2.28}$$

$\begin{pmatrix} I_i & k & I_i \\ -m' & q & m \end{pmatrix}$: is the Wigner 3-j symbols.

If the spin has an axial symmetric orientation with respect to a chosen coordinate frame (Z_{OR} axis), only the q=0 components of ρ_{kq} are non-zero and the non-diagonal elements define the coherence between the different m-states. Using the diagonal elements of the density matrix as population parameters $P(m)$ with $m = m'$ implies that the Equation (2.28) becomes :

$$\rho_{k0} = \sqrt{2I_i+1}\sum_{m}(-1)^{I_i+m}\begin{pmatrix} I_i & k & I_i \\ -m & 0 & m \end{pmatrix}P(m). \tag{2.29}$$

The statistical tensor ρ_{kq} is related to the orientation parameters B_{kq} by:

$$\rho_{kq} = \frac{B_{kq}}{\sqrt{2k+1}}, \tag{2.30}$$

where

$$B_{k0} = \sqrt{2I_i+1}\sqrt{2k+1}\sum_{m}(-1)^{I_i+m}\begin{pmatrix} I_i & k & I_i \\ -m & 0 & m \end{pmatrix}P(m). \tag{2.31}$$

To sum up, B_{kq} are related to the distribution of the magnetic substates of a nucleus in an excited state with spin I_i oriented around a chosen coordinate frame (z-axis). The distribution of magnetic substate can be specified by the population $P(m)$ of the $2I_i + 1m$ substate [10], which are related to the amount of alignment in the excited state.
Due to their simple transformation under rotation, one can use the orientation tensor to transform the $f1$ frame into the $f2$ frame:

$$B_{kq}^{f2} = \sum_{Q} B_{kQ}^{f1} D_{qQ}^{k}(\alpha, \beta, \gamma), \tag{2.32}$$

where D_{qQ}^{k} are Wigner D-matrices and (α, β, γ) are Euler angles.

2.3.1.2 Alignment and polarization

In the case where all spins are pointing to random directions, the ensemble of spins show an isotropic distribution. The m-quantum states, which are the spin projection on the orientation axis, are equally populated.

$$P(m) = \frac{1}{2I_i + 1} \text{ for all m } ; B_k = 0 (k \neq 0) \tag{2.33}$$

However, if all spins are pointing one direction, we talk about an axially symmetric ensemble of spins. Two kinds of axially symmetric ensembles are defined as an aligned and polarized ensemble. The alignment produced in an excited state in the nucleus shows a reflection symmetry of all m-quantum states populations which are the spin projected states on the axial symmetry axis z_{OR}, which means that $P(m) = P(-m)$.

$$P(m) = P(-m); B_k = 0 \text{ for odd } k \tag{2.34}$$

This case has two different types. If the angular momentum of the nucleus is aligned perpendicular to the symmetry axis z_{OR}, then the preferential population of the $m = 0$ substate dominates and the alignment is named as oblate alignment ($B_k < 0$). If the angular momentum of the nucleus is aligned parallel and anti-parallel to the symmetry axis z_{OR} then the $m = \pm I_i$ substates are preferentially populated and the alignment is referred to as prolate alignment ($B_k > 0$) [11].

When, the reflection symmetry is broken, the ensemble is called as polarized and it is described as:

$$P(m) \neq P(-m); B_k \neq 0 \text{ for odd } k \tag{2.35}$$

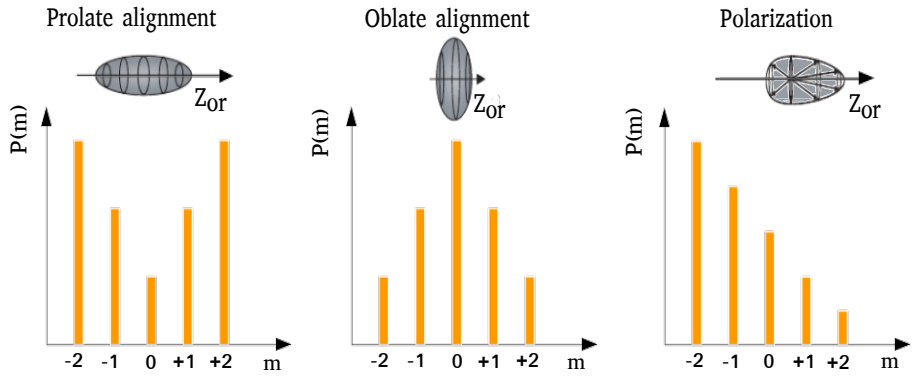

Figure 2.4 – Schematic drawing of different types of nuclear spin orientation (Prolate, oblate alignment and polarization)

The degree of normalized alignment, A, is defined as:

$$A \equiv \frac{\sum_m \alpha_2(m)P(m)}{|\alpha_2(max)|} = \frac{\sum_m (I_i(I_i+1)-3m^2)P(m)}{|\alpha_2(max)|}, \tag{2.36}$$

where $\alpha_2(m) = I_i(I_i+1)-3m^2$ [12]. The value of the normalization depends on whether the alignment is oblate ($A<0$) or prolate ($A>0$).

If $A=-1$ means that the ensemble is oblate-aligned. When the states of ensemble are given with integer spins, the dominant population is in the $m=0$ substates. One can see this alignment in fast-fragmentation reactions. For oblate-aligned half-integer spins, the population is equally distributed in the $m=\pm 1/2$ substates. Thus $\alpha_2(max)$ for full oblate alignment is:

$$\begin{aligned} |\alpha_2(m=0)| &= I_i(I_i+1) \quad \text{for integer spin,} \\ |\alpha_2(m=\pm 1/2)| &= I_i(I_i+1)-3/4 \quad \text{for half-integer spin.} \end{aligned} \tag{2.37}$$

For prolate alignment $A=+1$, only the magnetic substates with $m=\pm I_i$ are populated. Then the $\alpha_2(max)$ for full prolate alignment is:

$$|\alpha_2(m=\pm I_i)| = I(2I-1) \quad \text{for any spin.} \tag{2.38}$$

In practice to refer to the alignment, one can define the alignment in terms of B_k with $k=2$, but not for the higher-order terms which have a small effect on the observables compared

with the $k = 2$ term. The alignment is then related to the $k = 2$ orientation tensor as follows:

$$A = \frac{\sqrt{I(I+1)(2I+3)(2I-1)}}{\sqrt{5}|\alpha_2(max)|} B_2. \tag{2.39}$$

The nuclear polarization is defined in terms of the $k = 1$ orientation tensor. The normalized polarization is defined as:

$$P = \frac{\sum_m mP(m)}{I}, \tag{2.40}$$

and the relation between the polarization and $k = 1$ orientation tensor is:

$$P = -\sqrt{\frac{I+1}{3I}} B_1. \tag{2.41}$$

2.3.1.3 The distribution coefficients

The angular distribution coefficients $A_k(I_i -> I_f)$ are described by the formula:

$$A_k = \frac{1}{1+\delta^2}[F_k(L,L',I_f,I_i) + 2\delta F_k(L,L',I_f,I_i) + \delta^2 F_k(L,L',I_f,I_i)]. \tag{2.42}$$

Where the mixing ration δ is defined as:

$$\delta = \frac{\langle I_f||\pi(L+1)||I_i\rangle}{\langle I_f||\pi'(L)||I_i\rangle}, \tag{2.43}$$

where π and π' specify the type of radiation, electric or magnetic. Thus, the angular distribution coefficients A_k depends on the transition multipolarity.

However, the A_k are insensitive to the character of the transition for pure multipole transitions and it is not possible to determine the parity of the nuclear states of interest. In other words, if the A_k coefficients depend on the multipole mixing ration δ, therefore, the parity information can be obtained.

The F_k coefficients in Equation (2.42) are defined as:

$$F_k(L,L',I_f,I_i) = (-1)^{I_f+I_i+1}\sqrt{(2k+1)(2L+1)(2L'+1)(2I_i+1)} \times \begin{pmatrix} L & L' & k \\ 1 & -1 & 0 \end{pmatrix} \begin{Bmatrix} L & L' & k \\ I_i & I_i & I_f \end{Bmatrix} \tag{2.44}$$

where the $\begin{pmatrix} L & L' & k \\ 1 & -1 & 0 \end{pmatrix}$ is a Wigner 3-j symbol, and $\begin{Bmatrix} L & L' & k \\ I_i & I_i & I_f \end{Bmatrix}$ is a 6-j symbol.

For a pure multipole transition, e.g. a pure E2 transition, $L = L' = 2$. The F-coefficients are tabulated in the Ref [13].

2.3.1.4 The deorientation coefficients

If there are one or more unobserved radiations between the oriented parent state I_0 and the intermediate state I_i, the orientation of the I_i is determined by a modification of I_0 with deorientation coefficients U_k. Therefore, the orientation of the state I_i will be less than the parent state I_0. The orientation tensors of the intermediate state I_i in the cascade becomes [8]:

$$B_{kq} = U_k(I_0 \rightarrow I_i)B_{kq}(I_0). \tag{2.45}$$

For a pure transition of multipole order L, emitted between I_0 and I_i, the deorientation coefficient is given by:

$$U_k(I_0, I_i, I_L) = (-1)^{I_0+I_i+k+L}\sqrt{(2I_0+1)(2I_i+1)}\begin{Bmatrix} I_0 & I_0 & k \\ I_i & I_i & L \end{Bmatrix}. \tag{2.46}$$

For the mixed multipolarity L and $L+1$ between levels of spin I_0 and I_i, the dorientation coefficients becomes:

$$U_k(I_0 \rightarrow I_i) = \frac{U_k(I_0, I_i, I_L) + \delta^2 U_k(I_0, I_i, L+1)}{1+\delta^2}. \tag{2.47}$$

2.3.2 Perturbed angular distribution of γ-rays

In general the perturbed angular distribution of radiation emitted from an axially symmetric oriented states can be expressed by:

$$W(\theta, t) = \sum_k B_k G_{kk}(t) A_k P_k(cos\theta), \tag{2.48}$$

where A_k are the angular distribution coefficients, B_k are the orientation coefficients, G_{kk} are perturbation factors, and $P_k(cos\theta)$ are the Legendre polynomials. The angle θ gives the direction of observation of the radiation emitted with respect to the symmetry axis z of the oriented state, often the beam direction.

2.3.2.1 The perturbation coefficients

The perturbations are provoked by the interaction of nuclear moments with the electromagnetic fields in the medium. They depend mainly on the nuclear moments of the state I_i, the electromagnetic fields of the nuclear environment and the lifetimes τ of the state I_i.

Interaction of nuclear dipole moment with a static magnetic field can modify the m-state populations and thus affect the angular distribution of the subsequent γ-rays.
The perturbing Hamiltonian K is assumed to be a static Hamiltonian. The spin orientation of the state I_i evolves with time under the influence of K. The time evolution of the statistical tensors can be evaluated with the time evolution of the density operator:

$$i\hbar\frac{\partial\rho(t)}{\partial t} = [K, \rho(t)], \tag{2.49}$$

which is known as the Von Neumann equation. The solution is:

$$\rho(t) = e^{-iKt/\hbar}\rho(0)e^{+iKt/\hbar}. \tag{2.50}$$

The time evolution of the statistical tensors is described by the perturbation coefficients:

$$\rho^{\overline{k}}_{\overline{q}}(I_i, t) = \sum_{kq}\rho^{k}_{q}(I_i, 0)G^{q\overline{q}}_{k\overline{k}}(t). \tag{2.51}$$

The perturbation coefficients describe the influence of the extra-nuclear on the orientation of the nuclear state I_i and are given by [14]:

$$\begin{aligned} G^{q\overline{q}}_{k\overline{k}}(t) = \sqrt{(2k+1)(2\overline{k}+1)}\sum_{m\overline{m}}(-1)^{\overline{m}-m}\begin{pmatrix} I_i & I_i & k \\ -m & m' & q \end{pmatrix} \\ \times\begin{pmatrix} I_i & I_i & \overline{k} \\ \overline{-m} & \overline{m'} & q \end{pmatrix}\langle\overline{m}|e^{-iKt/\hbar}|m\rangle\langle m'|e^{+iKt/\hbar}|\overline{m'}\rangle. \end{aligned} \tag{2.52}$$

2.3.2.2 Spin-oriented ensemble pertubed by the static magnetic interactions

Producing a spin-oriented ensemble of excited nuclear states I_i by a suitable reaction is the first step, in order to measure a magnetic dipole moment μ. This ensemble can be perturbed with a magnetic field, either an external one or hyperfine field, which causes a precession of the spin-oriented ensemble with Larmor frequency ω_L around the magnetic field direction. If the magnetic of the interacting field $\vec{B}$ is known, the g factor can be extracted from ω_L. On the other hand, if the nuclear g factor is known, the magnetic field at the site of nuclei can be determined.
When the perturbation of the ensemble is caused by the interaction with an external magnetic field, the perturbation coefficients can be described classically. If the symmetry axis is

chosen to the z-axis of the S_K system and the Hamiltonian K is diagonal, the perturbation coefficients of Equation (2.52) become:

$$G_{k\bar{k}}^{qq}(t) = \sqrt{(2k+1)(2\bar{k}+1)} \sum_{m\bar{m}} \begin{pmatrix} I_i & I_i & k \\ -m & m' & q \end{pmatrix} \times \begin{pmatrix} I_i & I_i & \bar{k} \\ -m & m' & q \end{pmatrix} \times e^{-i(E_m - E_{m'})t/\hbar}, \tag{2.53}$$

where E_m are the eigenvalues of K. The magnetic splittings of the state I_i are uniform:

$$E_m - E_{m'} = (m - m')\hbar\omega_L = q\hbar\omega_L, \tag{2.54}$$

and $q = m - m'$ is fixed. The perturbation coefficients are reduced by using the orthogonality of the $3-j$ symbols to give the form:

$$G_{k\bar{k}}^{q\bar{q}}(t) = e^{-i\omega_L t}\delta_{q\bar{q}}\delta_{k\bar{k}}. \tag{2.55}$$

2.3.3 Particle-γ angular correlation

Consider now that the state I_i decays to state I_f by th emission of γ-ray at the spherical polar and azimuthal detection angles, respectively, θ_γ and ϕ_γ in coincidence with a particle at the spherical polar and azimuthal detection angles, respectively, θ_p and ϕ_p. The beam axis is the z axis in the coordinate system used. The θ_γ and θ_p are measured with respect to the beam axis. $\Delta\phi = \phi_\gamma - \phi_p$ is the difference between the azimuthal detection angles of the particles and γ-rays. Thus, the angular correlation function has the form and references therein [10]:

$$W(\theta_p, \theta_\gamma, \Delta\phi, t) = \sum_{kq} a_{kq}(\theta_p) G_k(t) D_{q0}^{k*}(\Delta\phi, \theta_\gamma, 0). \tag{2.56}$$

With $a_{kq}(\theta_p) = B_{kq}(\theta_p) Q_k F_k$. The $B_{kq}(\theta_p)$ is the statistical tensor in (2.31), which is determined by the segmented particle detector's position. F_k represents the F−coefficient for the γ-ray transition in Equation (2.44), and Q_k is the attenuation factor for the finite size of the γ-ray detector (see Appendix A.1.1). The $D_{q0}^{k*}(\Delta\phi, \theta_\gamma, 0)$ is the Winger-D matrix (see Appendix A.1.2). The G_k is the attenuation coefficient. For an example of E2 excitation, $k = 0, 2, 4$ and $-k \leqslant q \leqslant k$. The sum above is only valid for even k values. For the k odd values the statistical tensor are zero due to the parity conservation symmetry of the electomagnetic interaction.

2.3.3.1 Attenuations coefficients

The time-dependent vacuum de-orientation effect is specified by the attenuation coefficients, $G_k(t)$. For H-like J = 1/2 configurations the $G_k(t)$ are cosine functions[10]:

$$G_k(t) = 1 - b_k(1 - cos\omega_L t), \tag{2.57}$$

where t is the mean life of the nuclear state, and b_k is written:

$$b_k = \frac{k(k+1)}{(2I+1)^2}. \tag{2.58}$$

The ω_L is the Larmor frequency which is determined by the nuclear g factor

$$\omega_L = g(2I+1)\frac{\mu_N}{\hbar}B_{1s} \simeq g(2I+1)800Z^3 \quad MHz. \tag{2.59}$$

The B_{1s} is the hyperfine field at the nucleus due to a 1s electron:

$$B_{1s} = 16.7Z^3R(Z)Tesla. \tag{2.60}$$

with the relativistic correction factor:

$$R(Z) \simeq [1 + (Z/84)^{2.5}]. \tag{2.61}$$

2.4 Techniques to orient nuclei and their applications

It is necessary to produce a spin-oriented ensemble of excited nuclear state, in order to measure the nuclear moment. From a suitable reaction mechanism and nuclear spin interaction with surrounding environment, after the production of the nuclear state, the spin-oriented nuclear ensemble can be produced with some degree of orientation which depends on the formation process and reaction mechanism.

The orientation methods differ with the different reaction mechanisms. Usually, the polarizations methods used experimentally are optical pumping, low temperature nuclear orientation, tilted foil and projectile fragmentation, while alignment methods are related to the reaction mechanisms such as fusion evaporation, direct transfer reactions, incomplete fusion reactions, multinucleon transfer reactions, projectile fragmentation, knock-out and intermediate-energy Coulomb excitation, etc.

The optical pumping is described as the hyperfine interaction between the electron spin J and the nuclear spin I [15]. The atomic spin is polarized after several excitation/decay processes of photons and transfers this polarization to the nuclear ensemble which can be polarized of typically 30-50%. Where, the low temperature nuclear orientation method [16] is based on the interactions of nuclear electromagnetic moments with very strong electromagnetic fields at very low temperature (mK). Because of the large Zeeman spliting and the low temperature of the environment, the Boltzmann distribution of the nuclear spins have the non-degenerate m-quantum states. Therefore, the nuclear spins become polarized. From this technique, the typical amounts of polarization that can be observed are of the order of 20-80%. In another technique which is named Titled Foils (TFT), when an atom passes through a thin foil that is tilted with respect to the beam direction, the electron spins of the ions leaving the foil become polarized. This polarization is transferred to the nuclear spin via the hyperfine interaction in flight in vacuum after polarization of the ensemble when passing through the foil surface. One can place a several foils after each other at well defined distance to increase the nuclear polarization.
Another simple way to get a spin-oriented ensemble of nuclei is via the spin-orientation produced during the reaction itself.

2.4.1 The spin-oriented ensemble in fusion-evaporation reactions

In fusion-evaporation reactions, the spin alignment of the excited states, including isomers, can be described by a Gaussian distribution function:

$$\mathrm{P}(m) = \frac{e^{-m^2/2\sigma^2}}{\sum_{n=\mathrm{I}_i} e^{-n^2/2\sigma^2}}. \tag{2.62}$$

The width of the Gaussian distribution, σ, is related to the amount of alignment in the excited state. The orientation mechanism in fusion-evaporation reactions is illustrated by the large orbital angular momentum of the projectile ions which produce compound systems which have strong alignment of their angular momenta in the plane perpendicular to the beam direction. The rapid decay of these highly excited compound systems, by neutron and gamma emission, leaves the angular momentum vector of the populated states still strongly aligned, thus causing considerable anisotropies in the angular distributions of the γ-rays de-exciting the excited states. Using this kind of reaction mechanism allow to obtain a spin alignment

of states typically between 25% and 75% and a spin polarization up to 40% [9], when the reaction products are selected at an angle with respect to the incoming beam. However this type of production mechanism is not suitable to produce neutron-rich nuclei lying far from the stability line. Therefore, one can not consider this reaction mechanism to investigate isomeric states for neutron-rich nuclei. Other reactions can be applicable with radioactive ion beams (RIB) and, at the same time, provide sufficient degree of spin orientation.

2.4.2 The spin-oriented ensemble in Direct transfer reactions

The Direct transfer or single-neutron transfer reactions have been demonstrated to be widely applicable for the population of excited states using radioactive beams. The degree of 13% spin alignment was obtained with stable beam and reaction ^{65}Cu(d,p)^{66m}Cu [17] and ^{65}Ni(d,p)^{65m}Ni [18]. Although the production yield of exotic nuclei is higher in intermediate and high-energy projectile-fragmentation reactions (See section 2.4.4), the low energy transfer reactions show a higher level of spin-orientation. On the other hand, several difficulties oppose to the application of single-nucleon transfer reactions for nuclear moment studies of isomeric states with radioactive beams. The main difficulty comes from the energy/momentum transfer between the projectile and target nuclei for single-nucleon transfer reactions, which is relatively small. This does not allow for an efficient separation between projectile that needs to go away from the target, and the reaction products that need to remain in the target. Therefore the single-nucleon transfer reaction is not a simple production mechanism to use for isomeric-states studies with RIB.

2.4.3 The spin-oriented ensemble in incomplete fusion reactions

In the case of incomplete fusion, sometimes is called multinucleon transfer reactions, the energy/momentum transfer between the projectile and target nuclei can be large. The incomplete fusion processes are described to take place around the Coulomb barrier. When the incident energy of the projectile in the center of mass frame is sufficient to vanquish the Coulomb barrier, then the incident ion fuses with the target nucleus to form a composite system. As we can imagine, the projectile comes near the field of the target nucleus, it may break up and one of the fragments may fuse. One can cite several advantages of the incom-

plete fusion, one of these advantages is the population of higher spin, a few reaction channels opened and change of Z between the beam and the products. In order to reach to the neutron rich side of the nuclear chart, two reaction channels ^{7}Li(^{64}Ni,α n)^{66m}Cu and ^{7}Li(^{64}Ni,α p n)^{65m}Ni were performed at the ALTO facility in Orsay, France in December 2013 [19]. The results from this experiment are discussed in details in this reference (See section 4.1).

In fellowing works [20][21], it is shown that in multinucleon transfer reactions of neutron-rich Ca isotopes, with using the ^{48}Ca beam on ^{64}Ni at energies approximately twice the Coulomb barrier, the maximum alignment is of the order ≃ 70% perpendicular to the reaction plane. This can be used in determination of spin and parity of the neutron-rich nuclei which are hard to reach by standard fusion-evaporation reactions.

2.4.4 The spin-oriented ensemble in projectile-fragmentation reactions

Projectile fragmentation can be described as a peripheral collision between the projectile and a target nucleus. In this reaction mechanism the spin-orientation is described by the participant-spectator model [1] or, more commonly, the abrasion-ablation model. More details can be found at this reference [22]. In the participant-spectator model, the spin orientation of the fragments results from the orbital angular momentum left in the fragments during the projectile-target interaction, named also abrasion stage. The general principle is first suggested by Asahi et al. [23] [24]. When a projectile with an initial momentum $\vec{p}_0$ collides with the target, a participant part of nucleons at the position $\vec{R}_0$ with momentum $\vec{p}_n$ is removed from the projectile. The $\vec{p}_n$ is the sum of momenta of the removed nucleons. Thus the nuclear spin $\vec{I}_{PF}$ of the fragments is given with respect to the centre of mass as:

$$\vec{I}_{PF} = \vec{R}_0 \times (\vec{p}_n) \tag{2.63}$$

Using the momentum conversation in the projectile-rest frame, the momentum $\vec{p_{PF}}$ of the fragment can be written as $\vec{p_{PF}} = \vec{p}_0 - \vec{p}_n$. Thus the orientation of the spin is determined as a function of the momentum $\vec{p_{PF}}$:

$$\vec{I}_{PF} = \vec{R}_0 \times (\vec{p}_0 - \vec{p_{PF}}) \tag{2.64}$$

1. The "participant" zone is consists of highly excited prefragments. The outer projectiles which are called “spectators” are only slightly affected by the collision.

The resulting spin orientation produced in the projectile fragmentation reaction is partially or completely attenuated because of the removal of nucleons from the projectile.

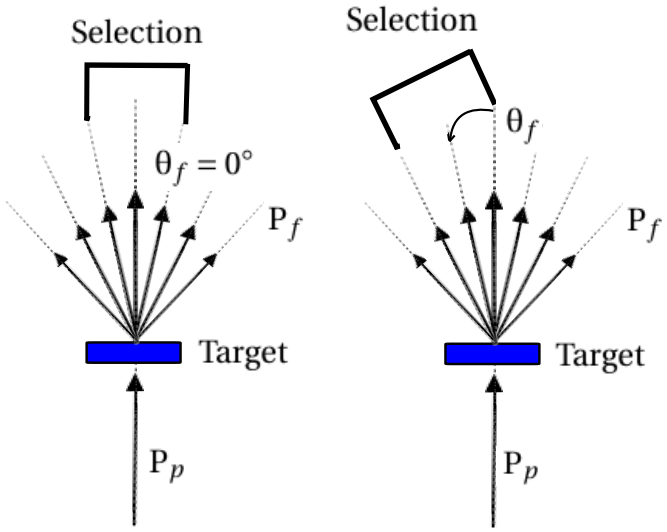

Figure 2.5 – Schematic drawing of the fragment selection. On the left side, the selected fragments ($\theta_f = 0°$) are spin aligned, where, on the right side the fragments selected under an angle θ_f with respect to the primary beam direction are spin polarized (right).

If the fragments produced in an intermediate or high-energy projectile fragmentation reaction are selected symmetrically around angle 0° with respect to beam direction, the fragment spins are spin aligned (see Figure 2.5). If fragments are selected at a finite angle with respect to the primary beam direction, the fragments are spin-polarized (see Figure 2.5).
The amount of alignment produced in fragmentation reactions varies considerably between 5% and 35% due to a range of experimental conditions.

2.4.5 The spin-oriented ensemble in Coulomb excitation reactions

The Coulomb force between a projectile of radius r_p with a mass A_p a nuclear charge $Z_p e$ and a target nucleus of radius r_2 with mass A_t charge $Z_t e$ is : $Z_p Z_t e^2/r^2$, where $r = r_p + r_t = r_0(A_p^{1/3} + A_t^{1/3})$ with $r_0 = 1.25$ fm is the average nucleon radius. The distance of the target from the asymptote of the hyperbola is called the impact parameter (See Fig 2.6). If the reduced de Broglie wavelength λ of the incoming particle is sufficiently short than the half-distance of

closest approach b for a head-on collision, the collision can be safely treated with semiclassical approximation. This yields an expression for the minimum distance of closest approach,

$$\lambda\!\!\!^{-} \ll \frac{b}{2} = \frac{Z_p Z_t e^2}{2E_p} \tag{2.65}$$

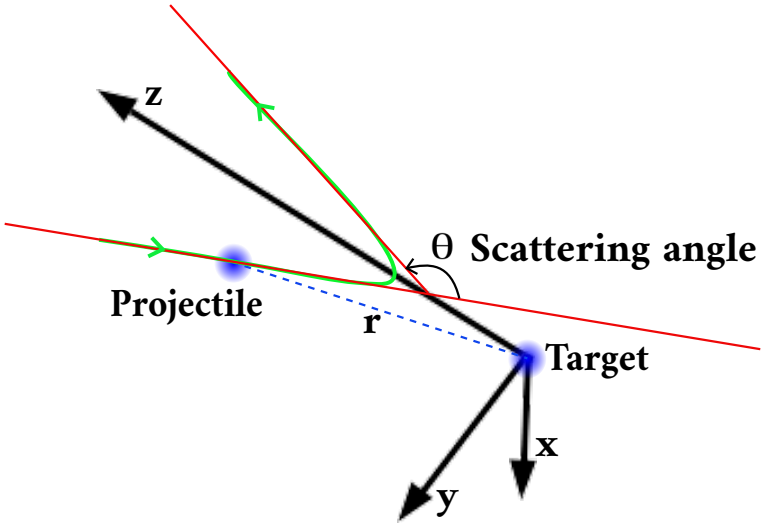

Figure 2.6 – Classical description of a projectile being scattered in the Coulomb field of a target nucleus. The hyperbolic orbit is essentially the same as that in Rutherford scattering.

The Coulomb excitation process can happen if the bombarding energy of charged particles is below the Coulomb Barrier. Thus the long-ranged and well known Coulomb force acts and the nuclear force is excluded, and it is considered as negligible compared to the electromagnetic interaction. In order to have a pure Coulomb excitation, one needs to keep the bombarding energy well below the Coulomb barrier. If the bombarding energy is above the Coulomb barrier, both type of forces act. In fact nuclear forces can have influence at energies below the Coulomb barrier. These effects are more important if Coulomb excitation cross sections are being measured to extract B(E2) values and quadrupole moments. In the present work where the angular correlations are of primary interest, the description will be restricted to the pure Coulomb excitation, thus, the "coulomb-nuclear" interference can be neglected.

The theory of Coulomb excitation is usually based on the semiclassical approximation, in which the source of the electromagnetic field is treated classically as a point charge moving along a Rutherford trajectory, whereas the nuclear excitation is calculated by quantum

mechanics methods. The ration $b/(2\lambda)$ is called the Sommerfeld parammeter η, written explicitly as

$$\eta = \frac{Z_p Z_t e^2}{2\hbar v_p}, \tag{2.66}$$

where Z_p and Z_t are the charge numbers of the projectile and target nucleus, respectively, while v_p is the velocity of the projectile. A classical description of the trajectory is ensured when $\eta \gg 1$. While the projectile moves along the classical hyperbolic orbit, the nuclear excitation is caused by the time-dependent electromagnetic field acting on the nucleus. The differential excitation cross section of a nuclear state can be determined in for low energies. At these energies, only electromagnetic interaction is allowed due to the Coulomb repulsion. The total differential cross section for exciting a definite state $|f\rangle$ from the state $|i\rangle$ is then given by

$$\left(\frac{d\sigma}{d\Omega}\right)_C = \left(\frac{d\sigma}{d\Omega}\right)_{Ruth} .P_{i\rightarrow f}, \tag{2.67}$$

where $(d\sigma/d\Omega)_C$ and $(d\sigma/d\Omega)_{Ruth}$ are the differential Colomb and Rutherford cross section, and $P_{i\rightarrow f}$ is the Coulomb excitation probability. The Coulomb excitation cross section σ from an initial state $|i\rangle$ to a final state $|f\rangle$ is determined by measuring the γ-ray yield $I_{f\rightarrow i}$ for the deexcitation $|f\rangle \rightarrow |i\rangle$. The Coulomb excitation probability is the square of the excitation amplitude b_{if} from the initial state $|i\rangle$ to final state $|f\rangle$, averaged and summed over magnetic sub-states as:

$$P_{i\rightarrow f} = \frac{1}{(2I_i+1)} \sum_{m_i m_j} |b_{if}|^2. \tag{2.68}$$

In time-dependent perturbation theory the excitation amplitude is found to be:

$$b_{if} = \frac{1}{i\hbar}\int_{-\infty}^{+\infty} \langle f|H_{int}(t)|i\rangle\, e^{\left(i\frac{E_f - E_i}{\hbar}\right)} dt. \tag{2.69}$$

where E_i and E_f are the energies of the initial and final nuclear state, respectively and $H_{int}(t)$ is the time-dependent electromagnetic interaction between the projectile and the target nucleus. The matrix element between the states of H_{int} that are describing the electromagnetic decay with the emission of γ radiation occurs in Equation (2.69). The initial and final states have definite spins and parities and it is convenient to expand the interaction in a multiple series. These series converge quite rapidly because of magnetic interactions can be neglected and only the lowest electric terms contribute. Thus the matrix element is proportional to

the electric multipole matrix element occurring in spontaneous gamma emission, predominantly E2 i.e quadrupole excitations [25].
The beam energy of the nucleus has a largest effect on population parameter P(m), thus affects W($\theta_p, \theta_\gamma, \Delta\phi, t$) significantly. The spin alignment in a Coulomb-excited nucleus depends on both the beam energy and the scattering angle. When the beam energy or scattering angle decreases, the alignment decreases, eventually changing the sign [26].

2.5 Experimental techniques for the measurement of g factors of nuclear states

Several techniques are used to measure g factors of the states of interest. The main idea is that a spin precession measurement allows determining the g-factor. The choice of a technique depends on the lifetime, spin, production method and decay mechanism of the state of interest.
To measure a g-factor, a spin oriented ensemble of nuclear states needs to be produced by a suitable reaction. By applying a magnetic field, either an external one or hyperfine field, one can perturb the oriented ensemble which causes a rotation of this ensemble with Larmor frequency ($\vec{\omega_L} = g\mu_N\vec{B}/\hbar$) around the magnetic field axis. The precession angle of the ensemble for a given time t can be determined as $\Delta\theta = \omega_L \cdot t$. One can observe the angle of precession of the ensemble by measuring the change of the angular distribution of associated γ-ray. Hence, if the lifetime of the state of interest is of the order of picoseconds, a strong magnetic field, an order of magnitude of kTesla, is required to induce a detectable precession effect. However, at the laboratory, our magnets cannot provide such strong fields, and to get around this issue one has to take advantage of hyperfine magnetic fields.

For this thesis work, a small external field combined with a known hyperfine field of Ni-Ni were used with Time-Differential Perturbed Angular Distribution (TDPAD) technique. For The Time-Dependent Recoiling In Vacuum (TDRIV) method, a hyperfine magnetic field with a free-ion recoiling in vacuum was used. These techniques are described in the following sections.

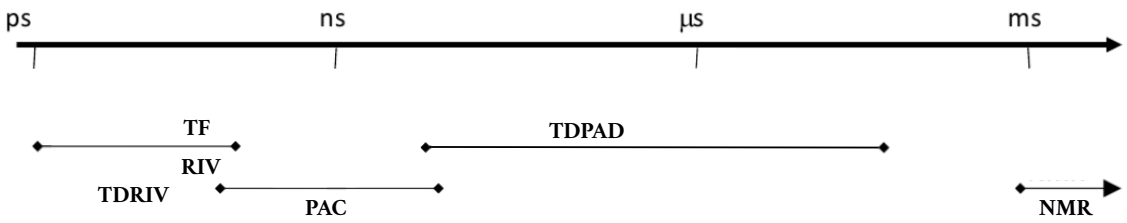

Figure 2.7 – Experimental techniques for the measurement of g factors of nuclear states, and their dependence on lifetime of states of interest.

All other techniques used for the measurement of g factors are detailed in this reference [27]

2.5.1 Time-Differential Perturbed Angular Distribution technique

This technique is suitable to be used for mean lives of nuclear states larger than about 10^{-9} second. In TDPAD experiment the spin-oriented ensemble is implanted into approriate host which is immersed in an external magnetic field provided by a permanent magnet. The applied magnetic field induces a precession of the nuclear spins about the magnetic field direction ($\vec{B}$) with Larmor frequency ω_L. For a specific position of detectors, in the plan perpendicular to magnetic field direction, one can gate on the energy of interest and get the intensities of γ-rays from de-excitation of state of interest as a function of the time $I(t,\theta)$. The $I(t,\theta)$ at different θ angle of detectors shows an oscillating behavior with a frequency ω_L proportional to the g factor, and the amplitude is proportional to the amount of spin-orientation in the nuclear state of interest.
For this work, the TDPAD is used to investigate the level of nuclear spin-orientation in incomplete fusion reaction mechanism applying on isomeric states in ^{65m}Ni and ^{66m}Cu.

2.5.2 Time-Dependent Recoil In Vacuum technique

As indicated by its name, the excited nuclei leave the target foil and recoil into the vacuum as charged ion where it decays in flight. In the vacuum, the electron atomic spin $\vec{J}$ of the recoiling ion is randomly oriented in space. Where the nuclear spin $\vec{I}$ is initially aligned by a nuclear reaction. During the travel of a free ion through the vacuum, the hyperfine interaction combines the atomic spin $\vec{J}$ to the nuclear spin $\vec{I}$ and together they precess around the

total spin $\vec{F} = \vec{I} + \vec{J}$ (See section 2.2). Hence, the hyperfine interaction is involved to attenuate the angular distribution of the γ-rays de-exciting the state of interest. Therefore, in order to measure the g factor, the impact of the hyperfine interaction can be observed via the reduced anisotropy of the angular correlation of the γ-rays.

The RIV compared to other techniques presents an appropriate way to measure g factor when used with a radioactive ion beam (RIB). The target can be thinner and neither the beam nor the Coulomb-excited ions stop in the traget, thus allow to remarkably reduce the radioactivity background. Also, the angular correlations can be extremely anisotropic which helps to measure the attenuations with low statistics.

The first use of RIV technique applied to the radioactive ion beam (RIB), to determine the g-factor of the 2_1^+ state in ^{132}Te, was carried out at the HRIBF Facility at Oak Ridge National Laboratory [28] [29].

TDPAD requires detector at specific positions, in plane perpendicular to the magnetic field, whereas the RIV method can use all angles in a γ-ray detector array with good coverage.

By using TDRIV technique we aimed to measure the g factor of 2_1^+ in ^{28}Mg.

More theoretical and technical details on both techniques will be developed a little further in this thesis (See 3.5.2 and 3.5.1).

2.6 The N=16 and 20 regions

Since the first paper published by Goeppert-Mayer (1948) showing that nuclei with 20, 50, 82 and 126 (called magic numbers) neutrons/protons exhibit a particular behavior, the nuclear shell structure has played an important role to shed light on a hidden structure of a nucleus. Today, the evolution of the shell model in nuclei far from the valley of stability is at the center of nuclear structure studies. The reader is referred to [30], where the different shell closures have been discussed in detail.

It has been reported that N = 20 loses its magicity for the exotic nuclei. The disappearance of N=20 and appearance of N=16 shell for neutron-rich, has been explained by the evolution of the gap generated by the neutron single-particle energy (SPE) difference between the $\nu 2s_{1/2}$ and $\nu 1d_{3/2}$ orbits. This sd-shell has been the object of several studies for many years, leading

to a new "Universal SD" (USD) shell Hamiltonian for realistic sd-shell wave functions to be used in nuclear structure investigations [31]. The first indication for the N =16 magic number came from the evaluation of the two-neutron separation energies S_{2n} in oxygen isotopes. A jump of S_{2n} in oxygen at N=16 can be interpreted as a new shell closure for oxygen[32]. Also, at the National Superconducting Cyclotron Laboratory (NSCL) at Michigan State University, USA, the measurement of the high energy of first excited state 2^+ in ^{24}O to be 4.72(11) MeV, provides a evidence that the ^{24}O behaves like a doubly magic nucleus[33]. Other papers on the fact that N=16 is a new magic number can be found at references [34] [30][35].

By adding protons to the $\pi d_{5/2}$ orbital the SPE of $\nu 1d_{3/2}$ orbital is reduced and gets more bound, in parallel, the N = 20 shell gap continues to widen[36]. This effect is due to the interaction between the $\nu 1d_{3/2}$ and $\pi d_{5/2}$ orbitals. Thus, the appearance of N=16 shell gap is due to the absence of the attractive interaction between $\nu 1d_{3/2}$ and $\pi d_{5/2}$ levels.

Another interesting feature is reported in [36], for Z=10 and Z=12. For these shells, the visibility of the gap is not clear. The nuclei around ^{32}Mg and ^{30}Ne isotopes show a ground state deformation. This behavior was considered to be the quadrupole collectivity intervention which develops a partial occupation of the pf shell and turns the ground state of N=20 isotones to the deformation. The region around the ^{30}Ne and ^{32}Mg is called "Island of Inversion"[37]. At the RIPS fragment separator at RIKEN, Japan, the "Island of Inversion" has been evident through the observation of increased collectivity of the supposed semi-magic ^{32}Mg and also other nuclei its vicinity[38][39]. Additionally, the nuclear moments of the single-particle/hole states in ^{32}Mg (i.e. respectively ^{31}Mg and ^{33}Mg) have been measured in order to determine their spin and parities, as well the underlying structure of those states[39][40]. However, until today the boundary of the Island of Inversion is still not defined and we are still lacking more experimental and theoretical efforts to determine if the nuclear wave function is understood in this mass region[34][41][42][43].

The nuclear moment with its particular sensitivity to the detailed composition of the nuclear wave function can provide a deeper insight into the interplay between spherical and deformed configurations in this key nucleus. The previous measurements of nuclear moments in ^{32}Mg were based on fits to the ground state of odd-A nuclides with a single particle/hole which is less sensitive to configuration mixing of a core. Thus, the 0^+ spin-parity of the ground state of the even-even Mg nucleus does not allow for an investigation of its single-

particle properties. As we will see later in this work, the closest approach one could have for it is the structure of the first 2^+ excited state, for which a nuclear moment measurement could disentangle the interaction of the different nuclear orbitals involved. Hence, the g factors of the 2^+ states are a sensitive probe to the shell modifications and to the delimitation of borders of the "Island of Inversion".

2.7 Bibliography

[1] Jackson J. D. *Classical Electrodynamics*. (John Wiley and Sons, New York), 1975. 8

[2] Miyazawa H. Deviations of nuclear magnetic moments from the schmidt lines. *Progress of Theoretical Physics*, 5:801–814, (1951). 12

[3] Arima A. and Horie H. Configuration mixing and magnetic moments of odd nuclei. *Progress of Theoretical Physics*, 4(509-511), (1954). 12

[4] Brussaard P. and Glaudemans P. *Shell Model Applications in Nuclear Spectroscopy*. (North-Holland Publishing Company, Amsterdam), 1977. 13

[5] Neugart R. and Neyens G. Nuclear moments. Lecture Notes in Physics. 700:135–189, (2006). 15

[6] Schneider W. Matthias E. and Steffen R. M. Nuclear level splitting caused by a combined electric quadrupole and magnetic dipole interaction. *Physical Review*, 125:261–268, (1962). 15

[7] Glasmacher T. Olliver H and Stuchbery A. E. Angular distributions of γ-rays with intermediate-energy beams. *Physical Review C*, 68:044312, (2003). 16

[8] Krane K.S. *in Low-Temperature Nuclear Orientation, Chap. 2*. (John Wiley and Sons, New York), 1986. 16, 21

[9] Alder K. and Winther A. *Electromagnetic Excitation. North-Holland*. Amsterdam, 1975. 17, 26

[10] Stuchbery A.E. γ-ray angular distributions and correlations after projectile-fragmentation reactions. *Nuclear Physics A*, 723(1-2):69–92, (2003). 18, 23, 24

[11] Glasmacher T. Olliver H and Stuchbery A. E. Angular distributions of γ rays with intermediate-energy beams. *Physical Review C*, 68:044312, (2003). 18

[12] Balabanski D. L. Borremans D. Coussement R. Daugas J. M. Georgiev G. Teughels S. Coulier N., Neyens G. and Vyvey K. β-level mixing resonance: A method to study the spin alignment and spin polarization of projectile fragments. *Physical Review C*, 63:054605, (2001). 19

[13] Frauenfelder H. and Steffen R. M. *In Alpha, Beta and Gamma-Ray Spectroscopy*. North-Holland, Amsterdam, 1965, 1965. 20

[14] Hamiltion W.D. *The Electromagnetic Interaction in Nuclear Spectroscoy*. North-Holland, Amsterdam, 1975. 22

[15] Carver T.R. Optical pumping. *Science*, 141:599–608, (1963). 25

[16] Brewer W.D. Recent developments in low-temperature nuclear orientation. *Reports on Progress in Physics*, 53(5):483–548, (1990). 25

[17] Lindenberger K.H. Ribbe W. Bleck J., Butt R. and Zeitz W. Magnetic moments, lifetimes and γ-decay of the lowest 6^- states in ^{64}Cu and ^{66}Cu. *Nuclear Physics A*, 197(2):620–630, (1972). 26

[18] Georgiev G.et al. g factor of the $9/2^+$ isomeric state in ^{65}Ni from transfer reaction. *The European Physical Journal A - Hadrons and Nuclei*, 30(2):351–356, (2006). 26

[19] Georgiev G. Nuclear moments and nuclear orientation from incomplete fusion and transfer reactions. *TANDEM-ALTO proposal for experiment*, page pages 1–6, (2013). 27

[20] Montanari D. et al. Probing the nature of particle–core couplings in ^{49}Ca with γ spectroscopy and heavy-ion transfer reactions. *Physics Letters B*, 697(4):288–293, (2011). 27

[21] Montanari D. et al. γ spectroscopy of calcium nuclei around doubly magic ^{48}Ca using heavy-ion transfer reactions. *Physical Review C*, 85:044301, (2012). 27

[22] Schardt D. Gunzert Marx K., Iwase H. and Simon R.S. Secondary beam fragments produced by 200 MeV/u ^{12}C ions in water and their dose contributions in carbon ion radiotherapy. *New Journal of Physics*, 10:075003, (2008). 27

[23] Asahi K. et al. New aspect of intermediate energy heavy ion reactions. large spin polarization of fragments. *Physics Letters B*, 251(4):488–492, (1990). 27

[24] Asahi K. et al. Observation of spin-aligned secondary fragment beams of ^{14}B. *Physical Review C*, 43(2):456–460, (1991). 27

[25] Alder K. and Winther A. *Coulomb Excitation. Academic Press.* New York and London, 1966. 31

[26] Stuchbery A.E. Some notes on the program GKINT: Transient-field g-factor kinematics at intermediate energies. *arXiv*, page pages 1–25, (2006). 31

[27] E. Bodenstedt et al. Hyperfine interactions. 24 - 26:pp 1069 – 1075, (1985). 32

[28] N. J. Stone et al. First Nuclear Moment Measurement with Radioactive Beams by the Recoil-in-Vacuum Technique: The g factor of the 2_1^+ state in ^{132}Te . *Physical Review Letters*, 94:192501, (2005). 33

[29] Stuchbery A. E. et al. Electromagnetic properties of the 2_1^+ state in ^{134}Te: Influence of core excitation on single-particle orbits beyond ^{132}Sn. *Physical Review C*, 88:page 051304, (2013). 33

[30] M.-G. Porquet O. Sorlin. Nuclear magic number: New features far from stability. *Prog. Part. Nucl. Phys.*, 61:602, (2008). 33, 34

[31] B. Alex Brown and W.A. Richter. New "USD" Hamiltonians for sd shell. *Physical Review C*, 74:034315, (2006). 34

[32] A. Ozawa et al. New magic number, N = 16, near the neutron drip line. *Physical Review Letter*, 84:5493, (2000). 34

[33] C.R. Hoffman et al. Evidence for a doubly magic ^{24}O. *Phys. Lett*, B672:17–21, (2009). 34

[34] Th. Glasmacher A. Gade. *Prog. Part. Nucl. Phys*, 60:161, (2008). 34

[35] R. V. F. Janssens. *Nature*, 459:1069, (2009). 34

[36] T. Otsuka et al. Novel Features of Nuclear Forces and Shell Evolution in Exotic Nuclei. *Phys. Rev. Lett*, 104:012501, (2010). 34

[37] J. A. Becker E. K. Warburton and B. A. Brown. *Phys. Rev. C*, C41:1147, (1990). 34

[38] T. Motobayashi et al. Large deformation of the very neutron-rich nucleus energy coulomb excitation. *Phys. Lett. B*, B 346:9, (1995). 34

[39] Guillemaud-Mueller D. et al. β-decay schemes of very neutron-rich sodium isotopes and their descendants. *Nuclear Physics A*, 426:37–76, (1984). 34

[40] Neyens G et al. Measurement of the spin and magnetic moment of ^{31}Mg: Evidence for a strongly deformed intruder groundstate. *Physical Review Letter*, 94:022501, (2005). 34

[41] W. Schwerdtfeger et al. *Physical Review Letter*, 103:012501, (2009). 34

[42] P. Doornenbal et al. *Physical Review Letter*, 103:012501, (2009). 34

[43] R. Kanungo et al. *Physical Letter B*, 685:253, (2010). 34

Chapter 3

Experimental setup and methodology

Contents

3.1 The HIE-ISOLDE facility

The g-factor measurement of the stable ^{22}Ne and unstable ^{28}Mg nuclei was performed at the ISOLDE facility, CERN in November 2017. The stable beam of ^{22}Ne was used to calibrate the system and to determine the HPGe positions on the frame (See section 3.2.4). In such an installation, the operators try to produce the radioactive ion beams (RIB) which correspond to the specifications required by physicists such as the intensity, purity and energy of RIB. Then, this RIB will be guided until a secondary target placed on the Miniball platform. This chapter describes the production of the nuclei of interest (See section 3.1.1) and their acceleration through the REX linac (See section 3.1.1.2) until the Miniball spectrometer (See section 3.2).

3.1.1 The radioactive isotope facility, ISOLDE at CERN

ISOLDE is a radioactive isotope facility utilising the Isotope Separator On-line technique. The ISOLDE facility benefits from a 1.4 GeV proton beam from the PS-booster (Proton Synchrotron Booster) at CERN installed on the border between France and Switzerland. The protons bombard the primary target with a maximum current of 2.0 μA to produce a wide range of radioactive isotopes. By applying a high electrical current to the target to provide heating , equivalent to around 2000°C for a UC_x (Uranium Carbide) target, the producted ions diffuse and effuse from the primary target and accelerated and transported by a ionisation source until a mass separator. Two separators are used at ISOLDE : The HRS (High Resolution Separator) and the GPS (General Purpose Separator).

3.1.1.1 Radioactive isotope beam production

To extract the species of interest with a high ion yield, the choice of the target material and ion source combination is crucial. The studied isotope (^{28}Mg) is localized on the neutron-rich side of the nuclear chart. In this case, a Silicon Carbide target (SiC) was used, where, it was irradiated with a proton beam with an energy of 1.4 GeV and an average intensity of $\simeq$ 1 μA. The chemical properties of the element of interest play an important role in the choice of the technique that is to be used in the extraction of this species. For Mg, which has an ionisation potential ~ 7.6462 eV, the resonance ionisation laser ion-source (RILIS) technique

was used. The process is performed with a laser beam tuned precisely to the energy of an atomic excitation in Mg. The atoms present in the transfer line are ionized only if the laser frequency corresponds to the selected atomic transition in Mg. After leaving the target, the ions present in the beam are accelerated to 30 keV and separated using the High Resolution Separator (HRS). The isotope of interest is selected according to the mass-to-charge ratio with a resolution of about M/ΔM = 5000. In order to examine the feasibility of any experiment, an "On-line" yield measurement is performed with taking into account the efficiency losses through the HRS ($\text{eff}_{\text{HRS}} \simeq 80\%$), trapping and charge breeding ($\text{eff}_{\text{REX}} \simeq 60-65\%$) and post-acceleration ($\text{eff}_{\text{EBIS}} \simeq 3-5\%$), the production yield of ^{28}Mg has been estimated at $1.5 \cdot 10^6$ pps.

3.1.1.2 Post-acceleration

The Radioactive beam EXperiment (REX) project was proposed in 1994 to accelerate the radioactive ion beams up to energies of 3 MeV/A. After the successful results of the REX project, it was decided to integer the project as a permanent setup at ISOLDE to bunch, charge breed and post-accelerate the RIB. One can refer to references [1] [2] to obtain more details about the REX project, also a wide technical details can be found on the design and commissioning report in reference [3]. In this section, we present a summary of the acceleration procedure and schematic representation can be seen in Figure 3.1.

Bunching and charge-breeding

A Penning trap, called REX-TRAP, is used to cool and bunch the ions beam delivered from HRS. The ions are decelerated from 30 keV to a few eV by collisions with an argon or neon buffer gas. Then the ions are bunched and extracted from the trap to be transported to the Electron Beam Ion Source (EBIS). In order to be able to post-accelerate the ions through the linear accelerator, a charge breeding operation is performed by using EBIS. The operation allows to increase the charge state of the ions by electron impact ionization process (A/Q < 4.5 required for mass seperation). The ions inside the EBIS are bombarded with beam of monoenergetic electrons with a current of 100-500 mA. Electrons are knocked out from ions. The charge breeding time depends on the required charge state. For the Mg nuclei with A = 28, a

charge state of $Q > 6^+$ is required to obtain a masse-to-charge ratio < 4.5. When a given equilibrium charge state (A/q~4)is achieved, the bunch is extracted from EBIS to pass through a mass separator and guided up to the REX-LINAC.

A/q separator

The ISOLDE's HRS separator perform an high resolution separation by mass. In addition the HRS is combined with an element-sensitive ionisation. As mentioned above, a laser ionisation device (RILIS) is used to have a good selection of nuclei of interest. However, after EBIS, the beam contains other components (comtaminants) coming from the residual gases (atmospheric and REX-TRAP buffer gas). Furthermore, other sources of contaminants come from the variety of charge states. For that, a A/q separator is built after EBIS to perform a mass separation with $\Delta(A/q)/(A/q) = 1/150$. In this thesis, we did not see a mass contaminants present in the $^{28}Mg(9^+)$ beam. The next phase is the injection of beam into the linear accelerator.

The Normal-conducting REX Linac

The first step of the post-acceleration of the RIB is performed with the Radio-Frequency Quadrupole (RFQ). At this step the RIB is accelerate from 5 keV/u to 300 keV/u. A rebunching takes place before injection to the interdigital H structure (IHS) to accelerate the beam up to about 1.1 and 1.2 MeV/u. The next step, the three 7-gap resonators (7GAP) increase the beam energy to 2.2 MeV/u. Finally, a nine-gap resonator (9GAP) accelerates the beam to the final energy of 3.0 MeV/u. All of these elements operate at the resonance frequency equal to 101.28 MHz, except the 9-gap which operates with resonance frequency of 202.56 MHZ.
The energy of the post-accelerated RIB is increased from the present ceiling of 3 MeV/u to over 5 MeV/u. Thus, a High Intensity and Energy at ISOLDE (HIE-ISOLDE) focuses on the upgrade of the existing installation (REX) with the addition of superconducting linac cavities
.

The Superconducting Linac

The goal of this structure is to post-accelerate RIB from 3 MeV/u up to 10 MeV/u. It receives a 3 MeV/u beam from the 9-gap, which is accelerated by using superconducting cryomodules. In order to synchronise with REX, they have to operate with the same resonance frequency. Actually two high-β cryomodules (β=10.3% with 6 cavities) are installed inside the Superconducting Linac beamline, increasing the beam energy up to 5.5 MeV/u for A/q = 4.5. This is the first phase. In the second phase, two others high-β cryomodules of the same type will be added, taking the beam energy up to 10 MeV/u for A/q = 4.5.

Bender

Finally, the beam can be distributed to different experimental stations. A bender with a mass-to-charge selection sends the beam to the experimental setup. The MINIBALL Spectrometer is installed at the first experimental station.

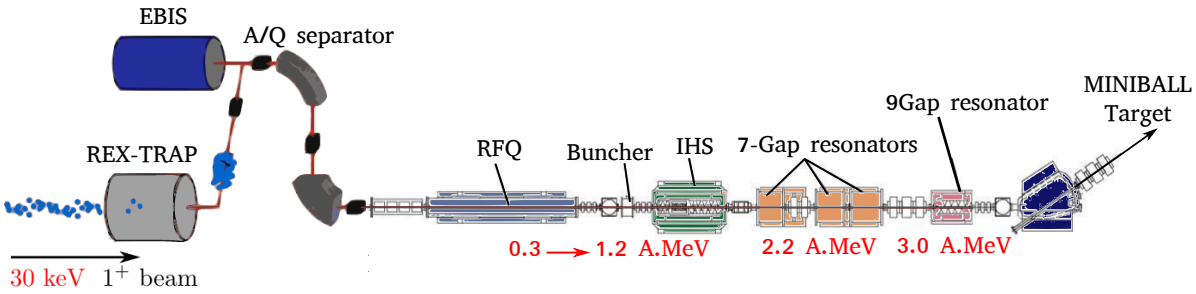

Figure 3.1 – A schematic diagram of the REX-ISOLDE accelator with indication of the energy that corresponds to each step

3.1.1.3 The time structure of the post-accelerated beam

The definition of the time structure is essential for the data acquisition (DAQ). We get several signals from ISOLDE. These are presented in figure 3.2.
The PS-Booster (PSB) delivers proton pulses every 1.2 seconde in Supercycle. The number of pulses in a Supercycle is variable between 24 and 38 pulses. These pulses are split between all CERN experimental platforms so that only a part of them are sent to ISOLDE. In the case of ^{28}Mg, 12 pulses were sent to ISOLDE target. The PSB signals, which come at the beginning of

each Supercycle, are sent to MINIBALL DAQ and labelled T1. After the REX-EBIS, the beam is injected into the Linac. A EBIS injection signal is sent to MINIBALL DAQ and is used to synchronize the Linac with the REX-EBIS extraction. This signal also is used to open an "on-beam" 800 µs windown for the Miniball spectrometer (see Section 3.2).

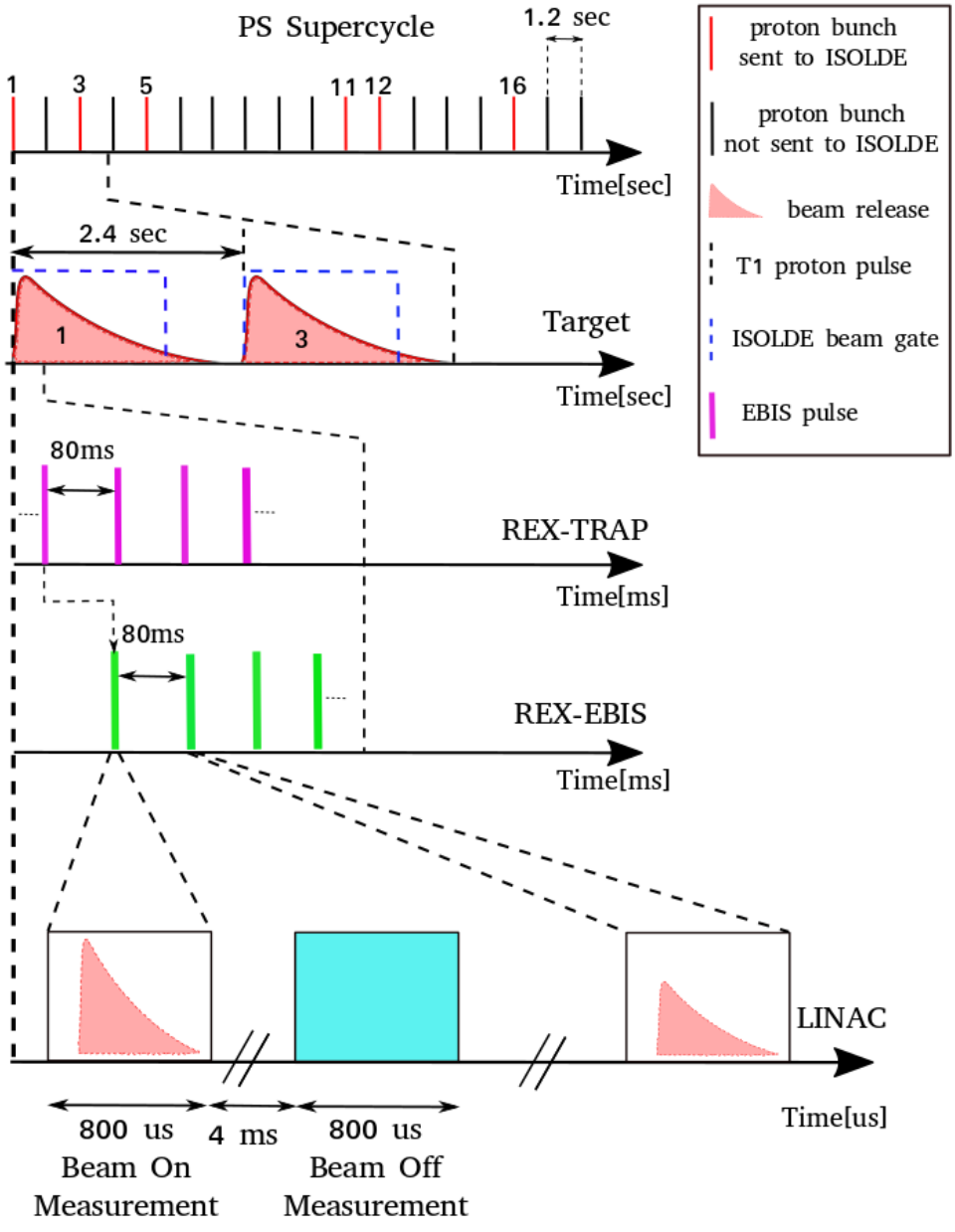

Figure 3.2 – Schematic of the time structure of the post-accelerated beam at ISOLDE.

3.2 The Miniball detection setup

When the beam impinges on the MINIBALL target, the projectile and target particles will be scattered. To ensure their detection we used a Double-Sided Silicon Strip Detector (DSSSD). While the emitted in-flight of γ-rays will be detected by the Miniball array.

3.2.1 Double-Sided Silicon Strip Detector (DSSSD)

The DSSSD [4] is placed in the target chamber at a distance of 33.2 mm from the target position. Usually, we call it a CD detector because visually it looks like a Compact Disk. The CD detector contains four quadrants each with 16-fold segmentation on the front side (called annular strips) and 24 radial strip on the back (called sector strips). On the back side, the sectors are electrically paired to give a twelve-fold. Using a segmented particle detector allows a better Doppler correction for the γ-rays, as one needs to know the trajectories of the scattered particles and the emitted γ-rays.
In addition, the energy deposited by the particles in the CD detector can be used to determine the velocity β as explained in Equation (3.4).

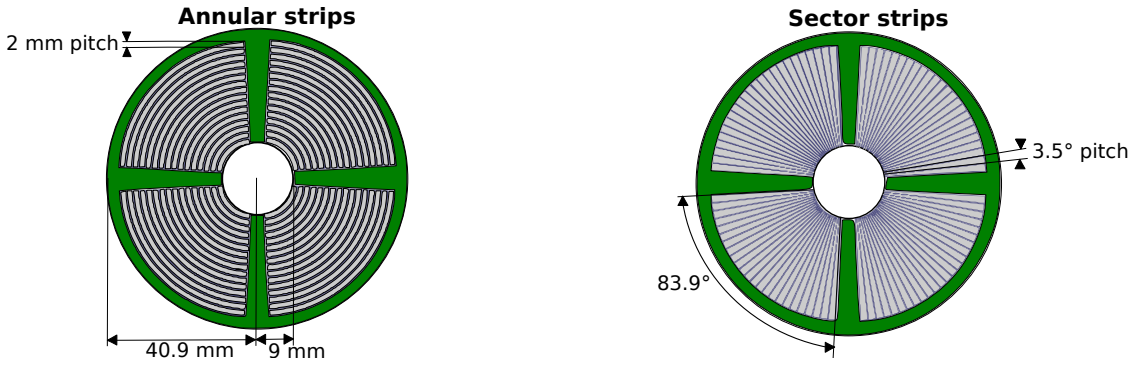

(a) front (b) back

Figure 3.3 – CD detector: A double sided silicon strip detector for radioactive nuclear beam experiments

One should note that the inter-strips have a thickness of between 0.3 and 0.8 µm of aluminium, which is not negligible for the stopping of heavy ions in this experimental campaign. Figure 3.3 shows a real picture of the CD detector, as well as its schematic drawing.

The quadrants and their characteristics, available for this experiment are listed in Table 3.1.

Quadrant number	Serial number	Thickness(μm)	Bias(Volt)	Leakage current(μA)
1 (left)	2892-3	138	-85	7.51
2 (top)	2892-27	138	-45	4.29
3 (right)	2892-26	138	-50	4.69
4 (bottom)	2892-28	136	-25	2.18

Table 3.1 – Details of quadrants are presented for this experimental campaign. The quadrants have been mounted on the holding plates with respect to the clockwise from beam direction.

Knowing the dimensions of the CD detector and its distance behind the target position, the angular coverage of each strip can be determined. The annular strips are counted from the outside (f15) to inside (f0) and from (b0) to (b11) on the back of the detector.

3.2.2 Miniball

The Miniball spectrometer, as shown in Figure 3.4, which is dedicated to high resolution γ spectroscopy at HIE-ISOLDE. The array consists of eight cluster HPGe detectors. Each cluster contains three individually encapsulated crystals, each with 6-fold electronic segmentation. The high granularity of the array from the segmented crystals allows a good Doppler shift correction. The HPGe detectors are mounted about 110 mm from the target which is located inside the target chamber.

As mentioned above, the electrical segmentation allows to improve the granularity of detectors to 144 detecting parts : 8 clusters x 3 crystals x 6 segments. A high standard voltage is applied to deplete the Ge crystals, a total of seven energy signals are collected in the segments and the core for a single crystal. The highest energy of the detected γ-ray is used to define the interaction point of the gammas within the Ge detector. The angular information coming from the segment is used to perform the Doppler correction of the in-flight γ-rays.

The collected signals from the Ge detectors are amplified, and shaped and integrated with pre-amplifiers associated to Digital Gamma Finder (DGF) modules. The DGF are modules with four inputs channel. Each crystal is attributed to two DGF modules with a total of eight

inputs. Therefore, to perform an experiment with eight HPGe clusters, a several DGF modules have been used.

During the experiment, the HPGe detectors are cooled by filling their dewars with a liquid nitrogen each 8 hours. Using a Cobalt source, the intrinsic energy resoultuion of segments are obtained to be ~2.8 keV and ~ 2.3 keV for the cores. More details about the Miniball set-up can be found in References [5].

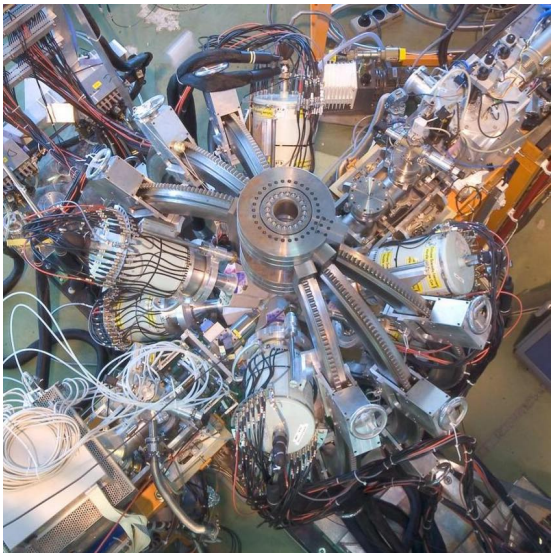

Figure 3.4 – Miniball setup picture taken from the top.

3.2.3 Efficiency determination

The relative detection efficiency for the responses of the detectors in the array was performed using a combination of a ^{152}Eu and ^{133}Ba calibration source. The ^{133}Ba is added because of low energy transition (at 80.9(3) keV) in order to cover a range from 80 keV to 1408 KeV. The measured intensities from the Evaluated Nuclear Structure Data File (ENSDF) at NNDC [6], and the peak area of γ-ray at various energies, one can obtain the relative efficiency by fitting the data points with their corresponding error bars to the function given below.

$$\varepsilon(\mathrm{E}) = exp\left(\sum_{i=0}^{4}(p_i log\mathrm{E})^i\right), \tag{3.1}$$

where ε is the relative efficiency and p_i are the parameters of the fit [7]. The relative efficiency curve with the experimental data points and the extracted total error is shown in Figure 3.5.

Symbols are the measured relatives' efficiencies, the solid line corresponds to a fitted function with Equation (3.1).

Parameters	2010	2011	2017
a =	2.683±0.010	4.238±0.011	2.574±0.008556
b =	-0.645±0.013	-0.529±0.015	-0.932±0.02731
c =	-0.04±0.02	-0.032±0.023	-0.01237±0.01237
d =	0.128±0.010	0.092±0.011	0.4006±0.0276
e =	-0.058±0.010	-0.048±0.011	-0.2±0.02044

Table 3.2 – Comparison of the relative efficiency parameters of Equation 2.1 for three different experimental campaigns

3.2.4 Ge-detector positioning

For the experiment analyzed in this thesis, the Ge-detector positioning is crucial to determine with a good precision the g factor of nuclear state of interest. Indeed, the γ-ray detection angles near $\theta = 90°$ present the strongest anisotropy around the ϕ direction. Therefore, the detector clusters were mounted on MINIBALL frame as a ring around the target chamber. Then, a calibration method was used to determine precisely the angles of clusters, which are polar (θ_{clu}) and azimuthal (ϕ_{clu}) angle with respect to the incident beam, as well as the rotation about its own axis (α_{clu}).
The calibration method consists to use the dependence of the Doppler shift on emission angle of γ-rays and particles (see Eauqtion (3.2)), and using the initial position values of clusters as read from the frame, one can fit the parameters determining the positioning of each crystal.

3.2.4.1 Calibration with ^{22}Ne

In order to calibrate the Ge-detector position. A ^{22}Ne beam is guided to the Miniball target position, which is called CD2 target. The latter is composed of 98% deuterated polyethylene with thickness of 1.1 mg/cm^2. Consequently, two reactions of types ^{22}Ne(d,γ p)^{23}Ne and

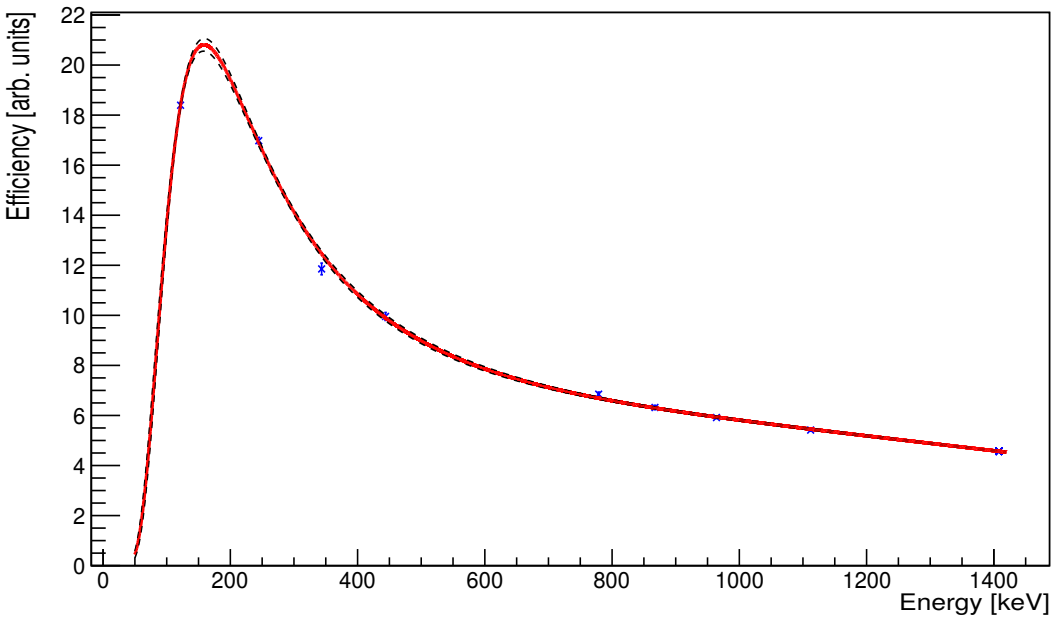

Figure 3.5 – Relative efficiency versus γ-ray energy fitted with Equation (3.1).

^{22}Ne(d,γ n)^{23}Na populate the first excited states in the product nuclei, then decay via 1017 keV and the 440 keV γ-ray transitions respectively. In this thesis, we used 440 keV γ-line to determine the position of the MINIBALL clusters.

In this case of a nuclear reaction, one can treat the angle of the γ-ray independently of the emitted nucleus, because of its small maximum scattering angle. Therefore, the calibration method consists in measuring the Doppler shift in each segment of the Miniball array, which is sensitive to the recoil velocity β, and the polar angle θ_{seg}. A fit of the Doppler shift in each cluster is performed with a total of 5 parameters (d_{clu}, β, θ_{clu}, ϕ_{clu} and α_{clu}), 33 values in all, the β being a common parameter for all clusters.

d_{clu} is the distance between the interaction point in the target and the interaction point in the Ge detector. Using the NIST Standard Reference Database [8], to calculate the mean-free path of γ-rays in Ge crystal equal to ∼ 10 millimeters, one can determine well the detector distance d_{clu}. β can be estimated using LISE++.

The fit logic is based on an iterative grid-search method, which starts from the initials values, including the angles of clusters read on Miniball support frame, and the fitted centroid of γ-line 440 keV in each segment Figure 3.6. The starting values are varied independently

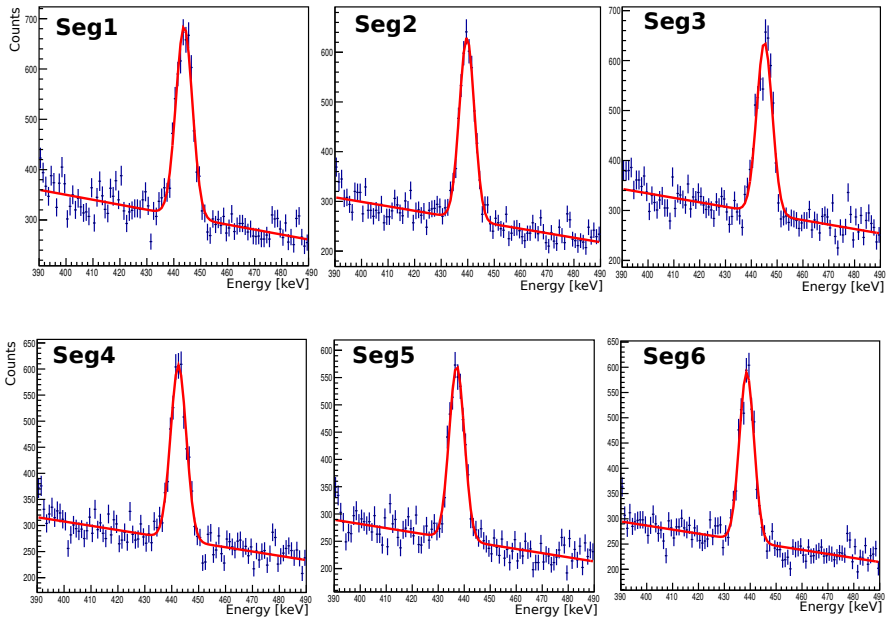

Figure 3.6 – Fit of the γ-line E = 440 keV. The centroid of the peak in each segment was used to define the angle positions of HPGe clusters in the MINIBALL frame.

until finding a local minimum by using χ^2 test. The cluster angles and detector distances are summarized in the table below 3.3.

Since the cluster angles are known, the angle of each segment can be determined 3.7. Therefore, the angular coverage of scattered particles and the emitted γ-ray angles will be used further in the data analysis.

3.2.5 Doppler correction

The long time, of scattered particles to travel from the interaction point into the target to the DSSSD (few ns) compare to short life times of the nuclear states of interest (few ps) is enough to cause an emission in-flight of γ-rays. The Doppler shift is given by the formula :

$$E_{lab} = \frac{\gamma E_0}{1 - \beta cos(\vartheta)}, \tag{3.2}$$

where γ is the Lorentz factor $1/\sqrt{1-\beta^2}$, E_{lab} correspond to the energy of the in-flight emitted γ-ray, E_0 is the original energy in the nucleus frame of reference, $\beta = v/c$ is the nucleus' velocity, ϑ is the angle between the scattered particle and the emitted γ-ray.
The segmented crystals and DSSSD detectors allow finding a combination between the tra-

Cluster number	d_{clu}(mm)	θ_{clu}(degree)	ϕ_{clu}(degree)	α_{clu}(degree)
17	115.42	107.35	141.7	333.73
12	89.20	72.54	36.20	280.21
16	106.96	64.95	107	256.49
13	97.05	117.91	77.3	70.03
22	103.36	112.03	256.90	252.93
18	109.25	75.14	218.2	90.49
14	105.37	102.65	323.50	275.42
23	106.15	65.69	282.10	69.04

Table 3.3 – Clusters numbering and angles in the Miniball array

jectory of the particle and the emitted γ-ray. Then, the angle ϑ can be constructed according to the formula:

$$cos(\vartheta) = sin(\theta_p)sin(\theta_\gamma)cos(\phi_p - \phi_\gamma) + cos(\theta_p)cos(\theta_\gamma), \tag{3.3}$$

where θ_p and θ_γ correspond to the angle of the scattered particle/emitted γ-ray with respect to the beam axis, and ϕ_p and ϕ_γ give the azimuthal angles of particle and γ-ray respectively.

The information of the particle energy, that is provided by the DSSSD detector, allows for the speed parameter β to be determined as shown in the formula below:

$$\beta = v/c = \sqrt{\frac{2E_p}{m_p c^2}}, \tag{3.4}$$

Where the particle energy E_p is expressed in units of MeV and its mass m_p in the units of MeV/c^2.

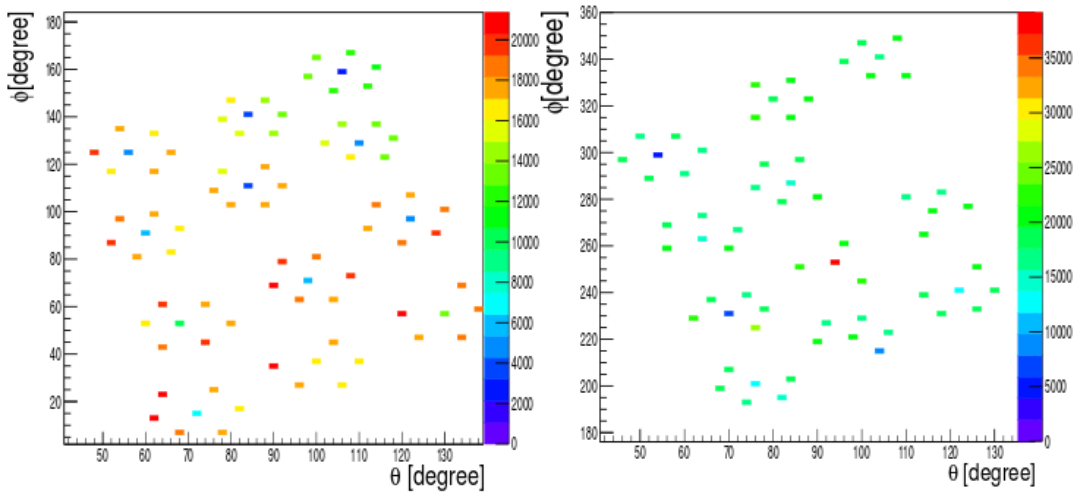

Figure 3.7 – Angle of each segment in MINIBALL HPGe defined from the core angles in the Table3.3.

3.3 Cologne Plunger

A plunger device has been developed at Cologne University to allow measurements of short lifetimes at HIE-ISOLDE with MINIBALL detector. The basic principle of the plunger device is based on a target and a stopper foil mounted parallel to each other at a well-controlled variable distance. The nucleus of interest is produced in the target foil and flies a given distance to the stopper foil. The γ-ray detectors observe the Doppler shifted energies for the γ-ray emitted in-flight.

A short-lived excited states decays while the recoil is traveling in flight between the two foils. In fact, by varying the distances between the foils such that the flight time of the recoil is of the same order as the lifetime of the state of interest, the γ-ray transition depopulating the state is then used to extract the lifetimes of the excited nuclear levels.

In our case, we replace the stopper material by a thinner foil (degrader) in order to reset the electron configuration of the mainly H-like ions. This foil slows the velocity of recoils only slightly and allows the detection of the reaction residues in the DSSSD. We refer to ions that decay between the target and the reset foil as "fast" and those that decay after the reset foil as "slow". A fast and slow peaks were not separated in the γ-ray spectrum at any detection angle (See 3.5.2).

The choice of the thickness of degrader foil and the plunger target is most important for the

application of the method for short lifetimes nuclear states. however, the lifetime of state being studied has to be long enough for the excited nuclei to emerge from the target and decay in the vacuum.

In the plunger, we have a fixed degrader and a movable target. The target holder is attached to the inner movable tube which connects the motor of the plunger to the target chamber. The degrader holder is attached to the outer not movable tube (see Figure 3.8) [9].

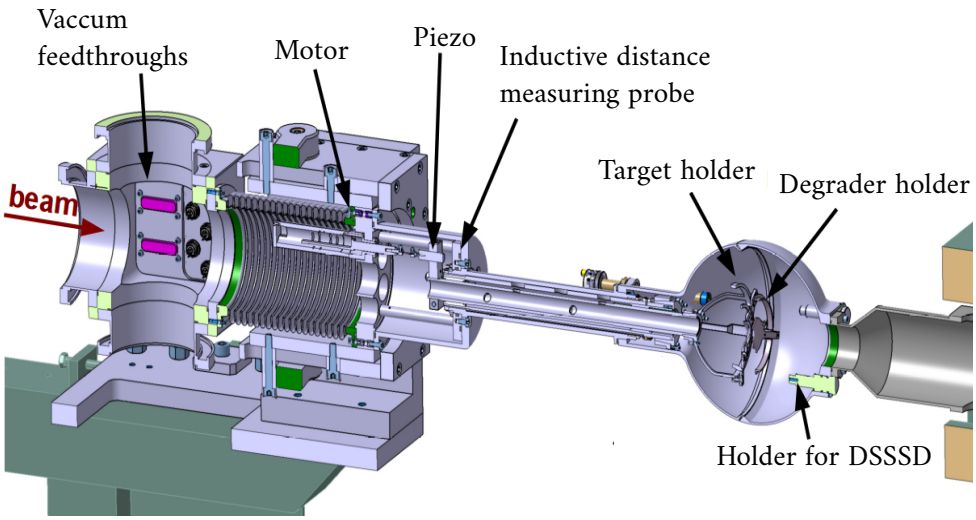

Figure 3.8 – A new plunger device for MINIBALL at HIE-ISOLDE.

The plunger calibration was performed using a 3.9 mg/cm^2 ^{93}Nb target and 1.1 mg/cm^2 degrader both in vacuum and in air. The calibration was made by measuring the capacitance between two foils as a function of the distances.

During the experiment, all distance and capacitances values were read by MINIBALL plunger computer (mbplungerpc01) and these values were stored on disk to be used during the analysis.

One can plot the inverse of Voltage as a function of the supposed distances (See Figure 3.9) to determine the offset value on the distances. Using the calibration parameters which are given by the plunger software of and the offset value defined from the Figure 3.9), one can determine the real distances. Table 3.4 presents the motor distance or the supposed distance (d_{motor}), micrometer distance or the distance given by the plunger software ($d_{position}$) and the real relative distance (d_{Real}).

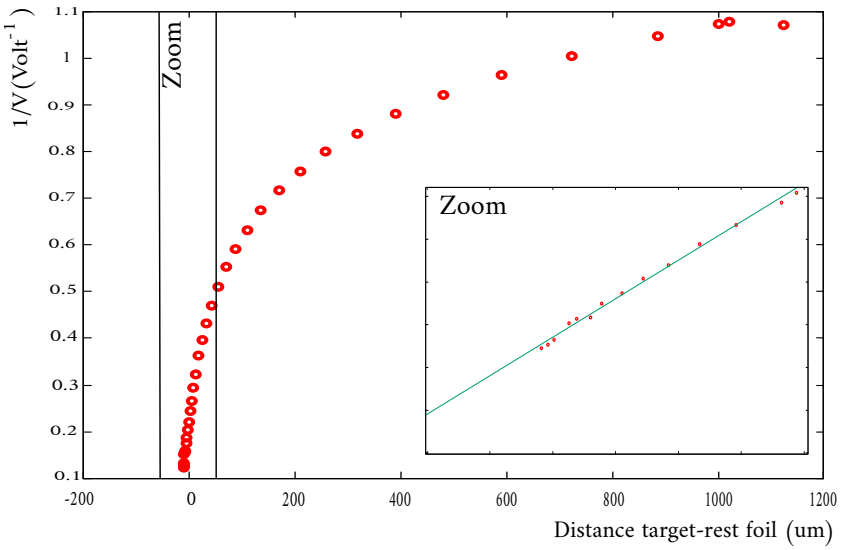

Figure 3.9 – Inverse of Voltage Vs. the motor distances. The fit of the lineaire part of curve gives an offset value of 11 µm between the motor distances and the micrometre reading distances.

d_{motor}(µm)	$d_{position}$(µm)	d_{Real} (µm)	d_{motor}(µm)	$d_{position}$(µm)	d_{Real}(µm)
-10.0	0.9	0.7	77.3	88.3	70.6
-4.0	6.9	5.5	84.0	95.0	75.9
2.5	13.5	10.8	90.3	100.5	80.3
9.0	19.9	15.9	102.5	113.2	90.4
15.0	25.8	19.2	115.0	126.0	100.7
27.5	38.1	30.5	127.5	138.4	110.6
34.0	45.0	35.9	152.5	163.3	130.5
40.0	51.0	40.7	166.0	176.0	140.6
52.5	63.0	50.3	177.5	188.0	150.2
59.0	70.0	55.9	190.0	200.0	159.8
65.0	76.0	60.7	202.5	216.0	172.6
71.0	82.0	65.5	227.5	240.2	191.9
			890.0	901.1	720.0

Table 3.4 – The real distances separated the target to degrader. The positions distances ($d_{position}$) are obtained by adding the offset value = 11 µm to the motor distance (d_{motor}). The real relative distance is obtained by dividing the $d_{position}$ by a calibration factor of 0.799.

3.4 Orsay-ALTO facility

A beam of ^{7}Li at an energy of 16 MeV (2.3 MeV/nucleon) from the ALTO accelerator facility at the Institute of Nuclear Physics of Orsay (IPNO), was implanted into enriched (95%) ^{64}Ni target of 4 mg/cm^2 thickness. The ^{65}Ni and ^{66}Cu nuclei were produced in a (^{7}Li, α n) and (^{7}Li, α pn) reactions respectively. At the same time the target serve as well as an implantation host due to the small recoil energy of ^{65}Ni and ^{66}Cu after the reaction. The beam intensity was about 1.0 pnA, pulse width of ~ 2 ns and time repetition of each pulse of about 2 μs.

The experimental set-up was comprised of the ORGAM (ORsay GAMma array) hyperpure germanium (HPGe) detector array surrounding an eight fold segmented plastic scintillation detector, located downstream from the target inside the beam line.

3.4.1 The Tandem-ALTO facility

ALTO (Accélérateur Linéaire et Tandem d'Orsay) is a facility located on the campus of the university Paris-Saclay (Orsay, France) and operated by IPNO. The historical part of this installation is constituted by the Tandem which is operational since 1972, in order to answer to the big questions of the time concerning the structure of the nuclei and the reaction mechanisms. It is an electrostatic negative ion accelerator of 15 MV, Van de Graaff type, consisting of three parts: the injector, the pulsation system and an accelerating part. It is designed to provide many stable beams, regularly producing beams ranging from proton to gold. It also has the possibility of delivering radioactive beams of ^{14}C and stable of ^{48}Ca. The Tandem can distribute stable beams to five experimental platforms through lines 210, 320, 410, 420, and 510.
ALTO, operational since 2006 is is an electron accelerator (50 MeV). Using a photofission method, ALTO is used as a driver to induce fission in a thick heated uranium carbide target.

3.4.2 ORGAM Array

The ORGAM array, as shown in Figure 3.10 which is dedicated to gamma spectroscopy at high resolution at ALTO. It has been assembled in the initial EUROGAM geometry. The

ORGAM array consists of 8 n type HPGe detectors from EUROGAM and EUROBALL collaborations. Each HPGe is located at 18 cm from the target.

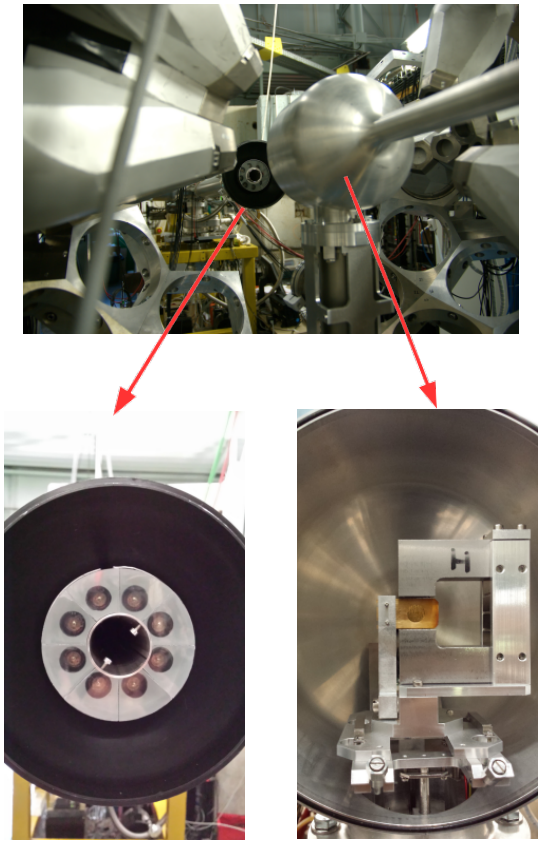

Figure 3.10 – Photo of the experimental setup installed at ALTO.

For a better ratio of full-energy to partial-energy events which is called the peak-to-total, or P/T ratio, each HPGe was surrounded by 10 dense scintillator BGO ($Bi_4Ge_3O_{12}$) Compton-suppression shield, being coupled to a photomultiplier (PM) (see Figure 3.11). They detect gamma rays Compton-scattered out of the Ge crystal. The reduction of Compton events can be achieved by requiring an anti-coincidence between the HPGe signal and the shield signal.

The detector angles are summarized in Table 3.5 Here ϕ is azimuth angle, with positive angles indicating clockwise rotation of the viewpoint and θ is the polar angle relative to the beam axis.

Energy, efficiency and FWHM calibrations for the response of the detectors in the array were performed using standard ^{152}Eu source placed at the target position. The FWHM depends on the energy of the gamma rays for transitions from the ^{152}Eu calibration source. For the 1408 keV γ-ray transition the energy resolution FWHM of the eight Ge crystal is given

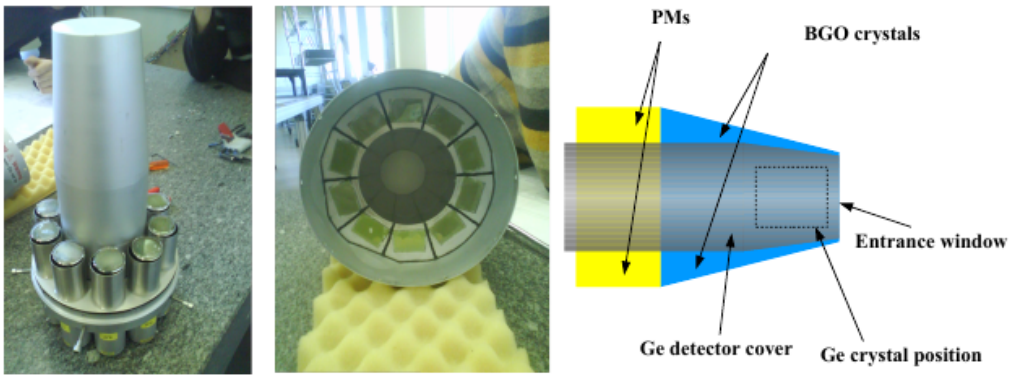

Figure 3.11 – The PM surrounding the inner cap of the BGO enclosure (left part), the 10 BGO crystals inside the anti-Compton enclosure (middle part), and the cap of the germanium detector inside the enclosure (right part).

between 2 keV and 2.8 keV. Relative efficiency is related to the peak area at a 1408 keV γ-ray transition to the number of γ-rays emitted by the ^{152}Eu source and depends on the geometrical arrangement of source and detector.

3.4.3 Segmented plastic scintillation detector

A segmented detector was located inside the target chamber to detect the particles. The plastic scintillator was segmented in eight parts, each of them coupled to a photomultiplier using a light guide. Here the z axis is the beam direction as shown in Figure 3.12. ϕ is the azimuthal angle in the x-y plane with positive angles indicating clockwise rotation of the viewpoint. θ is the polar angle measured from fixed beam direction. The numbering of the particle detectors was started at the vertically upward segment (ϕ_p= 0) and they were running anticlockwise when looking at the detector from the beam direction for negative ϕ angles.

3.4.4 Electronics and acquisition

The energy signal of each HPGe detector is shaped by a preamlifier and amplifier combination. The output signal from the amplifier is close to a Gaussian. The time signal of each HPGe is amplified by a fast timing amplifier. This type of amplifier provides voltage impulsions proportional to the incident (input or incoming) amplitude. The treatment is in this case much faster than for the spectroscopic amplifier, however one has a worse signal/noise

HPGe ID	θ_{det}(degree)	ϕ_{det}(degree)
2	46.5	90
8	133.6	90
16	46.5	-90
22	133.5	-90
1	72.1	85.6
10	22.4	72.4
18	72.1	-85.6
19	22.4	-72.4

Table 3.5 – Detector numbering and angles in the ORGAM array.

ratio. The resulting signal is then sent it to a CFD (Constant Fraction Discriminator). The input signal of the CFD is delayed and inverted, and undelayed signals are subtracted.

The current signal provided by each BGO anti-Compton shiled is integrated by a charge preamplifier (PAC) which produces a voltage output proportional to the integrated value of the input current in other words deposited energy. The signal from the PAC is sent to a threshold discriminator. The discriminator responds only to the input signals with a pulse greater than a given threshold value. When BGO signals coincidence with HPGe signals, time signal is sent to marker.

The output signal of each segment of the plastic detector were split to a spectroscopic amplifier and the output for energy signal and to a low-threshold discriminator for time signal.

The data acquisition system at ALTO is based on the use of the COMET– 6x (COMET = Encoding and time marking) ADC (Analog-to-Digital Converter) cards associated with the data acquisition system NARVAL and the visualization software CVISU. A COMET – 6 x card is composed of 6 channels. At our experiment a total of 16 channels were used, which were the 8 germanium and the 8-fold segmentated detectors. The COMET cards determine the

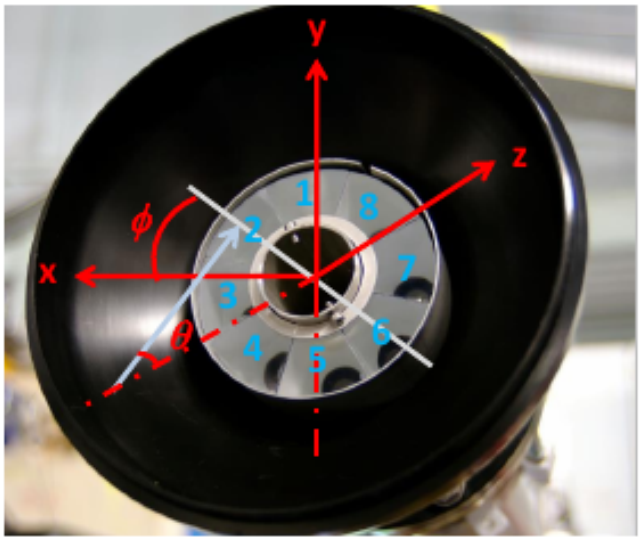

Figure 3.12 – Segmented scintillator detector inside the target chamber.

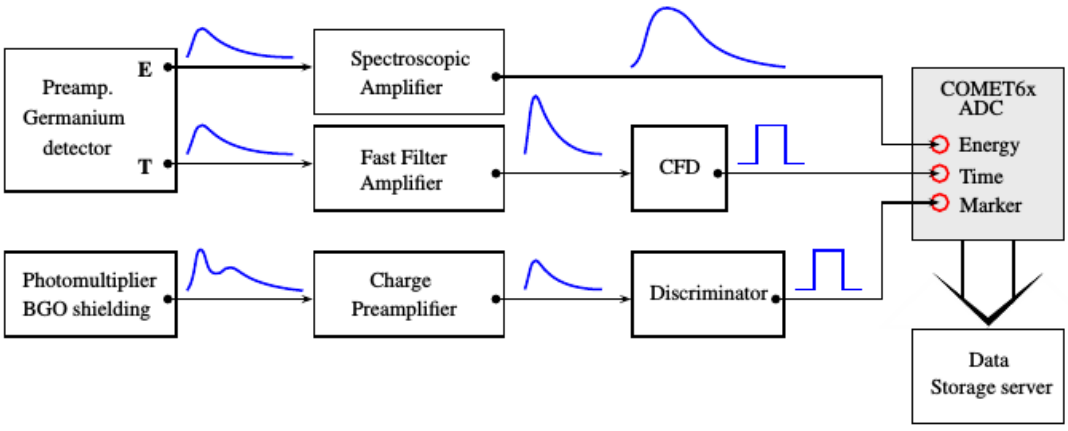

Figure 3.13 – Readout electronics.

energies and the time of signals, detected during the experiment. Data were recorded in event-by-event mode, the time and amplitude of the detected radiation from each event are recorded. The results of these amplitude and time coding are associated to a single event. Data are transferred in an event by event mode to the data storage server, to the acquisition computer via a 1 Gbit Ethernet link in order to visualize online the spectra to control.

3.5 Measurement methodologies

In this thesis, the Time-Dependent Perturbed Angular Distribution (TDPAD) used for the study of the level of spin-orientation in incomplete fusion nuclear reaction of the (6^-) isomeric state in ^{66}Cu and $(9/2^-)$ in ^{65}Ni, a precise measurement of the g factor of the first-excited state in ^{28}Mg was performed by new Time-Differential recoil in Vacuum (TDRIV) method.

3.5.1 TDPAD method

Depending on the lifetime of the isomer, several methods exist to study the magnetic and quadrupole moments of γ decaying isomeric states. TDPAD method has been used to measure nuclear moments of isomeric states, with a lifetime between 10 ns and 10 µs, produced and spin-aligned by fusion-evaporation and transfer reactions since the seventies [10]. The lower lifetime limit is determined by the fact that the Larmor precession period needs to be smaller or of the order of the nuclear lifetime. Thus this condition requires magnetic fields of the order of 1 Tesla to allow a fast enough precession for short-lived isomers. It is also limited by the 5-15 ns (200 ps) of typical time resolution of HPGe (LaBr) detectors. The upper limit of the lifetime is determined by the spin-spin and spin-lattice relaxation effects [11].
In a TDPAD experiment a spin-oriented ensemble of the isomeric states is implanted into a suitable host.
In the case of a g-factor measurement, if the implantation host is placed into a sufficiently strong static field, oriented perpendicular to the symmetry-axis of the ensemble orientation, the anisotropy is maintained. The interaction of the magnetic moment of the spin-oriented nuclear ensemble of the isomeric state with an external magnetic field $\vec{B}$ causes a rotation of

the spin-symmetry axis with a Larmor frequency:

$$\vec{\omega}_{\mathrm{L}} = -\frac{g\mu_{\mathrm{N}}\vec{\mathrm{B}}}{\hbar} \tag{3.5}$$

where g is the nuclear gyromagnetic factor, μ_{N} is the nuclear magneton, $\vec{\mathrm{B}}$ is the strength of the applied magnetic field and $\hbar$ is the Planck constant. This spin precession gives rise to a time-dependent change in the angular distribution of the radiation emitted by the oriented isomeric states, provided that the precession period is of the order of the isomeric lifetime (or shorter). It can be detected in a plane perpendicular to the magnetic field direction. In a typical in-beam experiment, the time-dependent intensity of the emitted γ-rays observed in a detector at an angle θ with respect to the beam axis is given by:

$$\mathrm{I}(t,\theta,\vec{\mathrm{B}}) = \mathrm{I}_0 e^{-t/\tau}\mathrm{W}(t,\theta,\vec{\mathrm{B}}). \tag{3.6}$$

Here τ is the mean lifetime of the nuclear state and $\mathrm{W}(t,\theta,\mathrm{B})$ is the γ-ray angular distribution and its rotation to the external field:

$$\mathrm{W}(t,\theta,\vec{\mathrm{B}}) = \sum_{k=even} \mathrm{A}_k \mathrm{B}_k \mathrm{P}_k cos(\theta - \omega_{\mathrm{L}} t). \tag{3.7}$$

where A_k is the angular distribution coefficient, which depends on the nuclear spin of the state emitting the γ-ray and the multipolarity of the emitted radiation; B_k is the orientation parameter and P_k is the Legendre polynomials.

This technique is based on the measurement of the intensity variation of the γ-rays as a function of time. Taking the intensity difference of two detectors positioned at 90° (See Figure 3.14) with respect to each other in a plane perpendicular to the external magnetic field and normalizing it to their sum gives the standard $\mathrm{R}(t)$ function is defined as:

$$\begin{aligned}
\mathrm{R}(t,\theta,\vec{\mathrm{B}}) &= \frac{\mathrm{I}(t,\theta,\vec{\mathrm{B}}) - \epsilon\mathrm{I}(t,\theta+\pi/2,\vec{\mathrm{B}})}{\mathrm{I}(t,\theta,\vec{\mathrm{B}}) + \epsilon\mathrm{I}(t,\theta+\pi/2,\vec{\mathrm{B}})} = \frac{\mathrm{W}(t,\theta,\vec{\mathrm{B}}) - \epsilon\mathrm{W}(t,\theta+\pi/2,\vec{\mathrm{B}})}{\mathrm{W}(t,\theta,\vec{\mathrm{B}}) + \epsilon\mathrm{W}(t,\theta+\pi/2,\vec{\mathrm{B}})} \\
&= \frac{3\mathrm{A}_2\mathrm{B}_2}{4+\mathrm{A}_2\mathrm{B}_2} cos[2(\theta - \vec{\omega}t)] \\
&= amp_{\mathrm{R}(t)} cos[2(\theta - \vec{\omega}t)].
\end{aligned} \tag{3.8}$$

where $amp_{\mathrm{R}(t)} = 3\mathrm{A}_2\mathrm{B}_2/(4+\mathrm{A}_2\mathrm{B}_2)$ is the oscillation amplitude.

Additionally, the angular distributions for the detectors at 180° with respect to each other are the identical. Thus the $\mathrm{R}(t)$ function can also be obtained by summing them two by two.

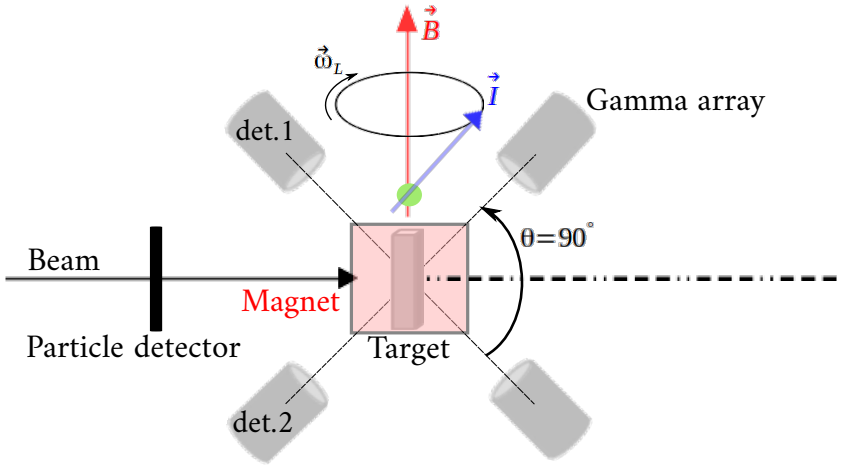

Figure 3.14 – Schematic drawing of TDPAD experimental arrangements.

The in-beam TDPAD method requires a pulsed production of the isomeric state with a period of T_0 greater than the mean lifetime of the excited nuclear state τ ($T_0 > \tau$) in order to preserve the oscillation amplitude from the incoherent superposition of the successive decay intensities. Another requirement is a pulse width of the beam pulses ΔT much smaller than the Larmor period ($\Delta T << 1/\omega_L$).

The R(t) function provides information both on the g factor of the state of interest, through the Larmor frequency, and on the degree of spin alignment A which is related to the R(t) amplitude. The spin alignment A can be calculated as:

$$A = \frac{\sqrt{I(I+1)(2I+1)(2I-1)}}{\sqrt{5}|\alpha_2(max)|} B_2, \tag{3.9}$$

$\alpha_2 = I(I+1) - 3m^2$ is defined in such a way, that $-1 \leq A \leq 1$. For maximum oblate or prolate alignment all nuclei are produced respectively in the lowest $m = 0$ or $\pm 1/2$, or the highest $m = I$ state. The $\alpha_2(m)$ is descibed in Section 2.3.1.2

In order to study the level of spin oriented-ensemble in incomplete fusion/Multinucleon transfert reactions of (6^-) isomeric state in ^{66}Cu and $(9/2^+)$ in ^{65}Ni, the TDPAD method was applied. The amplitude of a R(t) function depends on the position of the detectors with respect to the spin-orientation axis. Using the known g factor of ^{66m}Cu (6^-) and ^{65m}Ni $(9/2^+)$, and the hyperfine field in site, one can determine the level of spin-oriented ensemble.

3.5.2 TDRIV method

The combination between a RIV technique (Recoil In Vacuum) and a good definition of the time, is the definition of a new technique named Time Differential Recoil In Vacuum technique (TDRIV). The time parameter is obtained with using a plunger device, where the states of interest are produced in the target and they decay either before or after the degrader, placed at a well-defined distance.

In the traditional recoil-in-vacuum technique [12], once the excited nuclei emerge from a target foil as ions, they will carry with them one or more electrons. Their nuclear spin I are aligned by the reaction whereas the atomic spin J are oriented randomly. When the ions leave the target and on their way to reach the stopper foil, the hyperfine interaction couples the nuclear and atomic spins and they rotate around the total spin F with a frequency ω_L. This latter is proportional to the g factor. During the flight of the nuclei between target and stopper material, the spin nuclear orientation is periodically reduced. Hence, the angular intensity pattern of the γ-rays emitted in flight is modifiated. After a flight time of excited ions, they arrive to the stopper foil, in that moment, the interaction between the atomic and nuclear spins is turned off and the nuclear spins are blocked at a given direction. Therfore, for a given distance target-stopper foil D, all the nuclei are under the hyperfine interaction for the same time $T = D/v$.

One can vary the distance between the rest foil and target which implies a variation in the interaction time. Therefore, the nuclear orientation can be measured time differentially.

The angular distribution is composed of two parts, called, a "fast" and a "stopped" component. The attenuation coefficient for the stopped ions is :

$$G_k^{stopped}(T) = G_k(T), \tag{3.10}$$

Whereas the ions that decay in flight have an average deorientation coefficient of

$$G_k^{fast}(T) = \frac{\int_0^T G_k(t)\exp(-\lambda t)}{\int_0^T \exp(-\lambda t)\lambda dt} = 1 - b_k(1 - F(T)), \tag{3.11}$$

where $b_k = k(k+1)/(2I+1)^2$ and

$$F(T) = \frac{1 - \exp(-\lambda T)(cos\omega_L T - \omega_L \tau sin\omega_L T)}{(1+\omega_L^2\tau^2)(1-\exp(-\lambda T))}. \tag{3.12}$$

In the limit that T → ∞, the integral attenuation coefficients are obtained

$$G_k(\infty) \equiv G_k^{fast}(\infty) = 1 - b_k \left(\frac{\omega_L^2 \tau^2}{1 + \omega_L^2 \tau^2} \right). \tag{3.13}$$

If ω_L»1, the integral attenuation coefficients approach their hard core value $G_k(h.c) = 1 - b_k$. In the case when stopped and fast peaks cannot be resolved in the γ-ray spectrum, the observed attenuation coefficient is given by the sum of the both terms.

$$G_k^{total} = (1 - \exp(-t/\tau))G_k^{fast} + \exp(-t/\tau)G_k^{stopped} \tag{3.14}$$

In order to apply the TDRIV technique for radioactive beams, Stuchbery et al. [13] proposed a modification as shown in Figure 3.15. The stopper material is replaced by a thin foil in order to reset the electron configuration.

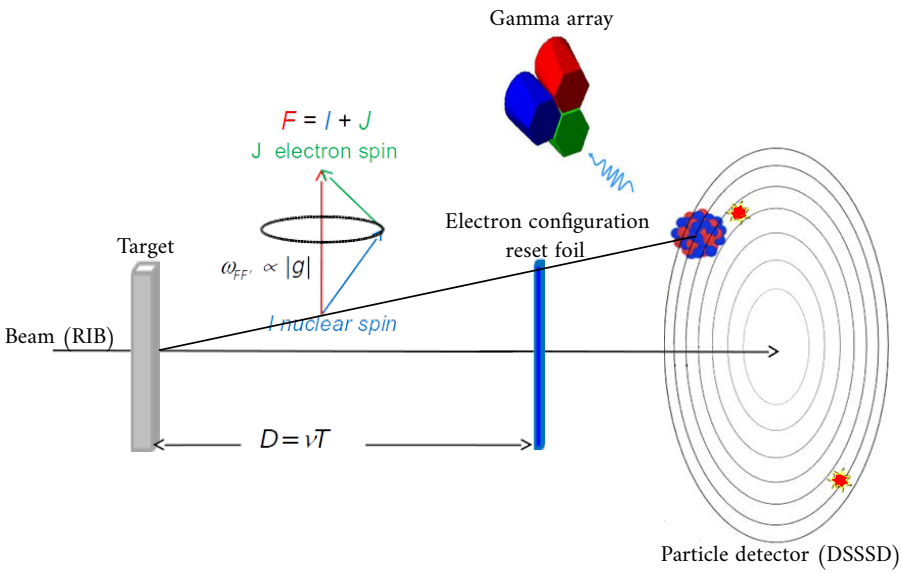

Figure 3.15 – Schematic drawing of TDRIV experimental arrangements.

The new TDRIV method has the same components of the attenuation coefficients as the traditional TDRIV. The ions that decay between the target and the reset foil are referred as ”fast” and those that decay after the reset foil as “slow”. For nuclei that decay before reaching the “reset” foil, the attenuation factor is the same as for the traditional technique. Decays of slow ions beyond the reset foil oscillate as $G_k(T)\bar{G}_k(\infty)$, where T is the flight time and $\bar{G}_k(\infty)$

is the average integral attenuation coefficient for slow ions beyond the reset foil. The fast and slow components of the γ-ray line are not resolved, the net angular correlation shows damped oscillations [14].

When excited nuclei emerged from the target, all possible configurations with lifetimes longer than or comparable to the nuclear lifetime and with up to three electrons in the 1s, 2s, and 2p orbits may contribute to the hyperfine interaction. The main contributions come from configurations with the unpaired 1s electron, which produce high magnetic field at the nucleus. The 1s electron configuration allows for precise determination of the hyperfine field from first principles.

In Horstman et al. work [15], the electronic configurations listed in his Table 2 has been calculated using the General Relativistic Atomic Structure Package codes GRASP2K [15]. Horstman's fields derived from his a_J values and are represented in the Tables 3.6 and 3.7. Horstman in his Eq.(4), defines the hyperfine frequency $\omega_{F,F'}$ as

$$\omega_{F,F'} = F(F+1) - F'(F'+1)\frac{a_J}{2\hbar}g, \tag{3.15}$$

where

$$a_J = \mu_N \frac{\overline{H(0)}}{J}, \tag{3.16}$$

and μ_N is the nuclear magneton, g the nuclear g factor, $\overline{H(0)}$ is the average hyperfine field strength at the nucleus, and J is the angular momentum of the atomic configuration. In his Table 2, Horstman gives a J in units of rad·ps^{-1}. In the Tables 3.6 and 3.7, the definition is

$$a_J = \frac{\mu_N}{\hbar}\frac{\overline{H(0)}}{J}. \tag{3.17}$$

It is convenient to use:

$$\frac{\mu_N}{\hbar} = 4789 \mathrm{G} auss^{-1} s^{-1} = 0.04789 (k\mathrm{T} esla)^{-1} ps^{-1} \tag{3.18}$$

With this definition,

$$\omega_{F,F'} = F(F+1) - F'(F'+1)\frac{a_J}{2}g. \tag{3.19}$$

Configuration	Term	J	a_J (rad · ps^{-1})	$\overline{H(0)}$(kTesla)
H-like ions				
$1s^1$	$^2S_{1/2}$	1/2	2.76	28.81
$2s^1$	$^2S_{1/2}$	1/2	0.35	3.65
He-like ions				
$1s^12s^1$	$^3S_1$	1	1.53	31.95
$1s^12p^1$	$^3P_2$	2	0.71	29.65
$1s^12p^1$	$^3P_1$	1	0.72	15.03
Li-like ions				
$1s^22s^1$	$^2S_{1/2}$	1/2	0.28	2.92

Table 3.6 – Hyperfine fields for H-like, He-like and Li-like Mg ions.

Configuration	Term	J	a_J (rad · ps^{-1})	$\overline{H(0)}$(kTesla)
H-like ions				
$1s^1$	$^2S_{1/2}$	1/2	1.60	16.70
$2s^1$	$^2S_{1/2}$	1/2	0.20	2.09
He-like ions				
$1s^12s^1$	$^3S_1$	1	0.89	18.58
$1s^12p^1$	$^3P_2$	2	0.41	17.12
$1s^12p^1$	$^3P_1$	1	0.42	8.77
Li-like ions				
$1s^22s^1$	$^2S_{1/2}$	1/2	0.15	1.56

Table 3.7 – Hyperfine fields for H-like, He-like and Li-like Ne ions.

3.6 Bibliography

[1] D. Habs et al. *Nuclear Physics A*, 616:29, (1997). 41

[2] P. V. Duppen and K. Riisager. *Journal of Physics G:Nuclear and Particle Physics*, 38:024005, (2011). 41

[3] F. Ames, J. Cederkäll, T. Sieber, and F. J. C. Wenander. The REX-ISOLDE Facility: Design and Commissioning Report. *CERN, Geneva*, (2005). 41

[4] A.N. Ostrowski et al. CD: A double sided silicon strip detector for radioactive nuclear beam experiments. *Nucl. Instr. and Meth*, A:448–480, (2002). 45

[5] P. Reiter et al. The MINIBALL array. *Nuclear Physics A*, 701:209–212, (2002). 47

[6] E.A. McCutchan. Evaluated Nuclear Structure Data File (ENSDF). *Brookhaven National Laboratory*, National Nuclear Data Center, (2018). 47

[7] Nele Kesteloot. *Deformation and mixing of co-existing shapes in the neutron-deficient polonium isotopes*. PhD thesis, KU Leuven. 47

[8] M.J.Berger et al. NIST STandard Reference Database8 (XGAM). *National Institute of Standard and Technology, Gaithersburg, MD.*, (2010). 49

[9] Stefan Thiel. mechanics workshop. *Institut für Kernphysik, Cologne*, (). 53

[10] Goldring G and Hass M. *in Treatise in Heavy Ion Sciences*. dited by D.E.Bromley (Plenum Pres, New York,1985). 60

[11] Brown B. A. *Lecture Notes in Nuclear Structure Physics*. Michigan State University Michigan State University. 60

[12] Goldring G. *In Heavy Ion Collisions*. edited by R. Bock (Amsterdam: North-Holland). 63

[13] Stuchbery A.E. et al. Electron-configuration-reset time-differential recoil-in-vacuum technique for excited-state g-factor measurements on fast exotic beams. *Physical Review C*, 71(047302), (2005). 64

[14] A. Kusoglu et al. Nuclear g-factor measurement with time-dependent recoil in vacuum in radioactive-beam geometry. *Physical Review Letters*, (2015). 65

[15] Horstman R.E., Eberhardt J.L., Doubt H.A., Otten C.M.E., and Van Middelkoop G. Recoil-distance measurements of g-factors for ^{24}Mg(2_1^+) and ^{20}Ne(2^+). *Nuclear Physics A*, 248(2):291–316, (1975). 65

Chapter 4

Results

Contents

4.1 Data analysis

4.1.1 Alignment of the isomeric states in ^{65}Ni and ^{66}Cu

In order, to observe the γ-rays, from the de-excitation of the isomeric states in ^{65}Ni and ^{66}Cu, the entire HPGe ORGAM array at ALTO platform was used. The HPGe detectors were placed at a distance of 180 mm from the target. The energy calibration of the HPGe detectors was performed using an ^{152}Eu source. During the preparation of the experiment, one $LaBr_3$ detectors was added to be used as timing signal (beam off). That signal was afterwards replaced by the beam pulsing signal.

The α particles, expected to be emitted during the nuclear reaction mechanism, were detected by the particle detectors (8-fold segmented annular plastic scintillators) which are positioned into the ORGAM vacuum chamber, and covering angles between $\theta = 30°$ and $\theta = 60°$. The detection of the α particle is a signature of the incomplete fusion reaction mechanism.

A typical γ-ray energy spectrum obtained in the present experiment of all detected γ-rays is shown in Figure 4.2. The level scheme for the ($9/2^+$ in ^{65}Ni and 6^- in ^{66}Cu) isomeric decay is displayed in figure 4.3. The γ-rays were identified from the full projection of the $\gamma-\gamma$ matrix on one axis (see Figure 4.1). The measured γ-ray intensities have been obtained from the singles γ-ray in one HPGe detector. The properties of the levels and the γ-ray transitions of ^{65}Ni and ^{66}Cu are presented in Table 4.1.

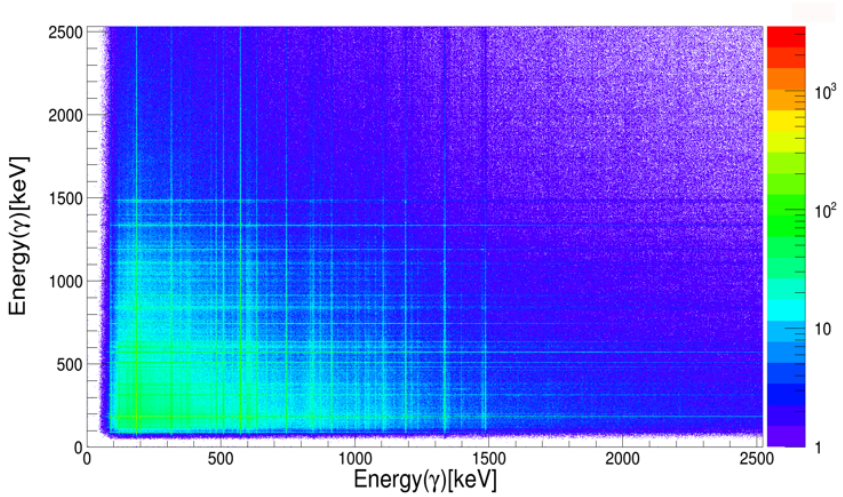

Figure 4.1 – $\gamma-\gamma$ energy matrix in 200-1900 ns time window.

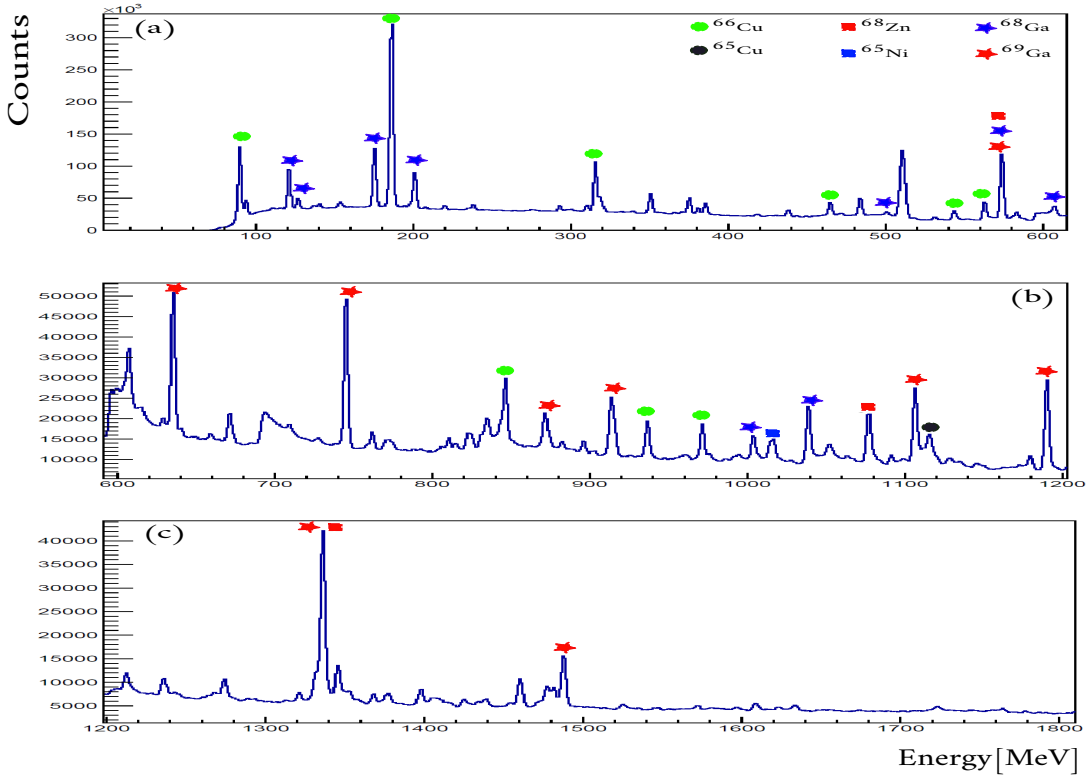

Figure 4.2 – Typical γ-ray energy spectrum in 50-1900 ns time window. Only the most intense γ-rays are marked.

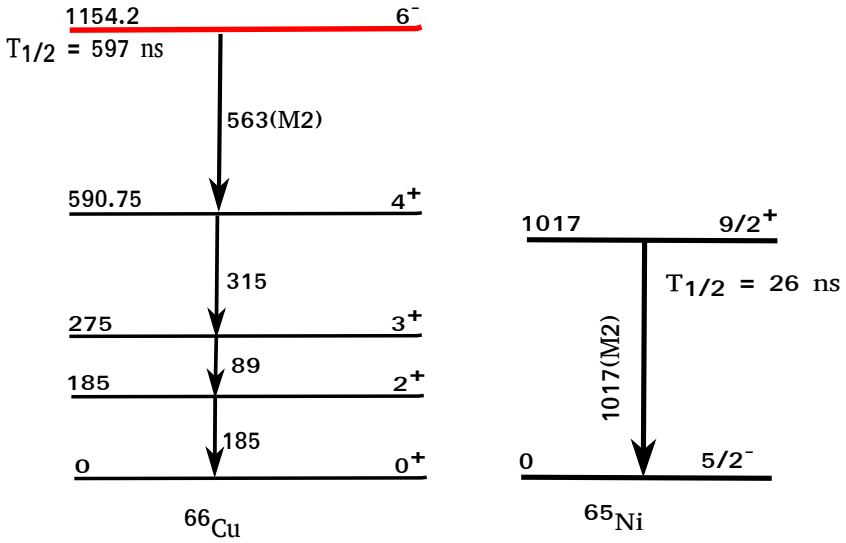

Figure 4.3 – Level Scheme of ^{65}Ni and ^{66}Cu below the $(9/2)^+$ and 6^- isomeric states respectively.

E_γ(keV)	N_γ	reaction & transition	$\frac{\sigma_\gamma(E)}{\sigma_\gamma(175)}$
1017(1)	$2.43\cdot 10^5 \pm 5.89\cdot 10^2$	^{65}Ni : $9/2^+ \rightarrow 5/2^-_{gs}$	22.09 %
1115.53(2)	$2.43\cdot 10^5 \pm 5.70\cdot 10^2$	^{65}Cu : $5/2^- \rightarrow 3/2^-_{gs}$	22.09 %
1424(1)	$6.05\cdot 10^4 \pm 2.39\cdot 10^2$	^{66}Ni : $2^+ \rightarrow 0^+_{gs}$	5.50 %
385(1)	$4.68\cdot 10^5 \pm 8.76\cdot 10^2$	^{66}Cu : $(1)^+ \rightarrow 1^+$	42.55 %
1039.2(3)	$2.36\cdot 10^5 \pm 5.77\cdot 10^2$	^{66}Zn : $2^+ \rightarrow 0^+_{gs}$	21.45 %
93.31(5)	$3.18\cdot 10^5 \pm 6.98\cdot 10^2$	^{67}Zn : $1/2^- \rightarrow 5/2^-_{gs}$	28.91 %
1077.34(2)	$2.21\cdot 10^5 \pm 5.50\cdot 10^2$	^{68}Zn : $2^+ \rightarrow 0^+_{gs}$	20.09 %
438.34(5)	$3.71\cdot 10^5 \pm 7.80\cdot 10^2$	^{69}Zn : $9/2^+ \rightarrow 1/2^-_{gs}$	33.73 %
574.2(1)	$9.43\cdot 10^5 \pm 1.25\cdot 10^3$	^{69}Ga : $5/2^- \rightarrow 3/2^-_{gs}$	85.73 %
175.02(1)	$1.1\cdot 10^6 \pm 1.32\cdot 10^3$	^{68}Ga : $2^+ \rightarrow 1^+_{gs}$	100.00 %

Table 4.1 – Levels and γ-ray transitions of the most intense channels. The efficiency-corrected γ-ray intensities, are normalized to the highest produced channel 175 keV in ^{68}Ga. Spins and parities have been taken from the National Nuclear Data Center (NNDC).

The most intense channels observed during the experiment were coming from the ^{68}Ga, ^{69}Ga and ^{66}Cu isotopes. According to the PACE4 Calculations (see Figure 4.4), the ^{68}Ga, ^{69}Ga channels were associated to fusion-evaporation reaction mechanism with a dominant amount compare to other coming channels like Cu, Ni and Zn. The ^{66}Cu isotope is associated either to fusion-evaporation or transfer reactions. We have seen also a small amount of ^{65}Cu and ^{65}Ni.

The reaction rate, or the number of γ-rays, which were observed in the germanium detector is given by :

$$R = \sigma \cdot I \cdot N \tag{4.1}$$

where σ is the cross-section, I is the incoming beam current from the tandem accelerator, and R represents the the number of counts under the γ-ray peak. The number of target nuclei N can be expressed as $N = \rho N_A/A$. The thickness of the target is represented by the density ρ and is given in grams per unit area, N_A is Avogadro's number and A is the molecular weight of the target material. The experimental setup allows to determine the relative cross-sections

rather easily. The Equation 4.1 can be rearranged to give the relative γ-ray cross-section (σ_γ) in terms of the count rates from experimental data as

$$\sigma = \frac{R}{\epsilon_\gamma \cdot I \cdot N} \tag{4.2}$$

where, ϵ_γ is the relative full energy peak detection efficiency of the detector for the specific γ-ray.

Since the intensity data accumulated during the beam-time at a beam intensity of 10^8 pps, a relative cross-section have been derived for the 385 keV and 1017 keV γ-lines of ^{66}Cu and ^{65}Ni, respectively. The relative cross-section are normalized to the highest produced channel reaction which is ^{68}Ga. The both channels of interest in ^{66}Cu and ^{65}Ni occur a significant amount of statistics, they present 42% and 22% respectively of the cross-section of the most intense reaction channel (see Table 4.1). Comparing with the cross-section calculations from the PACE4 fusion-evaporation code : $\frac{\sigma(^{66}Cu)}{\sigma(^{68}Ga)} = 6.3\%$ and $\frac{\sigma(^{65}Ni)}{\sigma(^{68}Ga)} = 0.0005\%$. One can deduce that the ^{65}Cu and ^{65}Ni channels were not mainly produced from the fusion-evaporation mechanism, they could be associated to the nucleon transfer of proton and/or neutron to the ^{64}Ni target nuclei (incomplete fusion reaction).

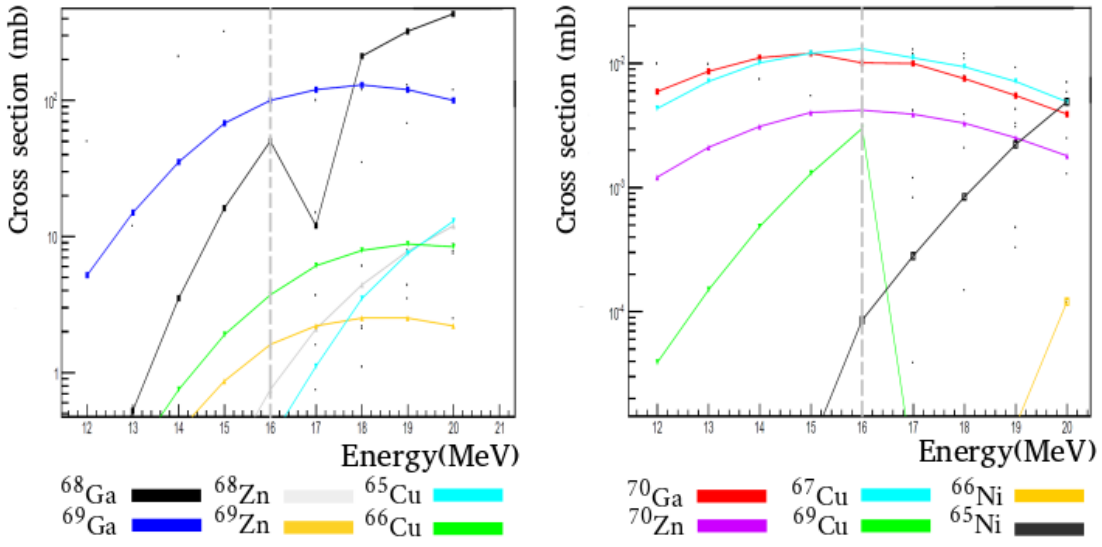

Figure 4.4 – Cross-section calculations with using PACE4 fusion-evaporation code.

The time spectrum of the isomeric decay transitions in ^{65}Ni and ^{66}Cu, with E_γ = 1017 keV and E_γ = 563 keV respectively, are shown in Figure 4.5. The half-life, with statistical uncer-

tainty only, was obtained as $T_{1/2}$ = 24(2) ns and $T_{1/2}$ = 590 (7) ns in ^{65}Ni and ^{66}Cu respectively, which agrees well with the previous measurements ($T_{1/2}$ = 25(1) ns and $T_{1/2}$ = 600 (7) ns) [1] [2].

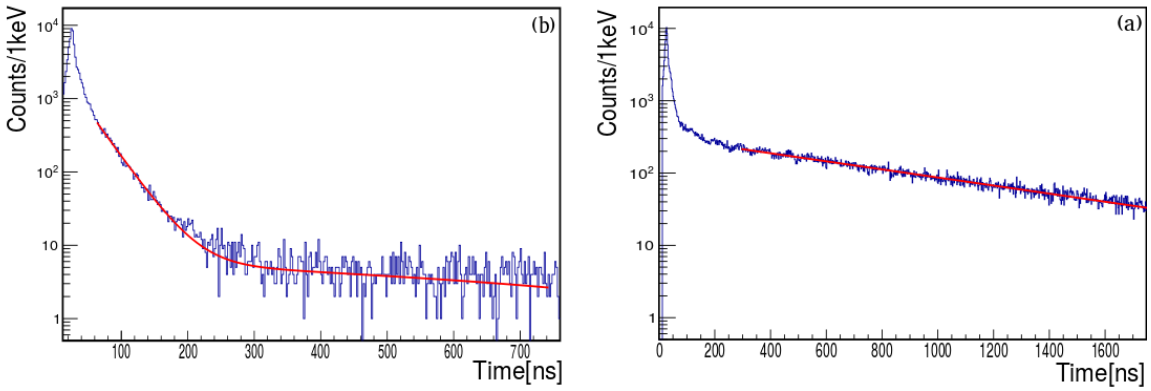

Figure 4.5 – Time spectrum, (a) produced by applying an energy gate E_γ = 563keV on matrix γ-time. Time spectrum (b) produced by applying an energy gate E_γ = 1017 keV on matrix γ-time. The spectra were fitted with a sum of an exponential (expo) and a polynomial of first degree (pol1). The results of fit gave a half-life of ^{65m}Ni to be $T_{1/2}$ = 24(2), and a half-life of ^{m66}Cu to be $T_{1/2}$ = 590(7).

To study the level of the spin orientation of an isomeric decay by applying the TDPAD method, one has to define the time t = 0 identification and select correctly the γ-ray of interest. For that, one can project the energy-time spectra (see Fig 4.6) on the time axis. It means the projection on time axis of the prompt γ-rays flash and all intensities of γ-line decayded from the isomeric states and energy levels. The prompt flash is used for t = 0 identification (see Fig 4.6) and the time spectra for all Ge crystal were properly aligned for their t = 0 as a function of energy.

Energy-gated time spectra were used to construct the experimental R(t) functions for both isomeric transitions in ^{65}Ni and ^{66}Cu. This for the different detector combinations defined in Equation 3.8. The experimental R(t) functions was constructed in two cases : a) for all detected γ-ray without any condition on particles detection and b) with condition on particles detection which means a treatment of a sub-ensemble of nuclear oriented states. We knew also that the R(t) function was defined in Equation 3.8 with the assumptions that the detectors all have the same efficiency and without a contribution from the background to

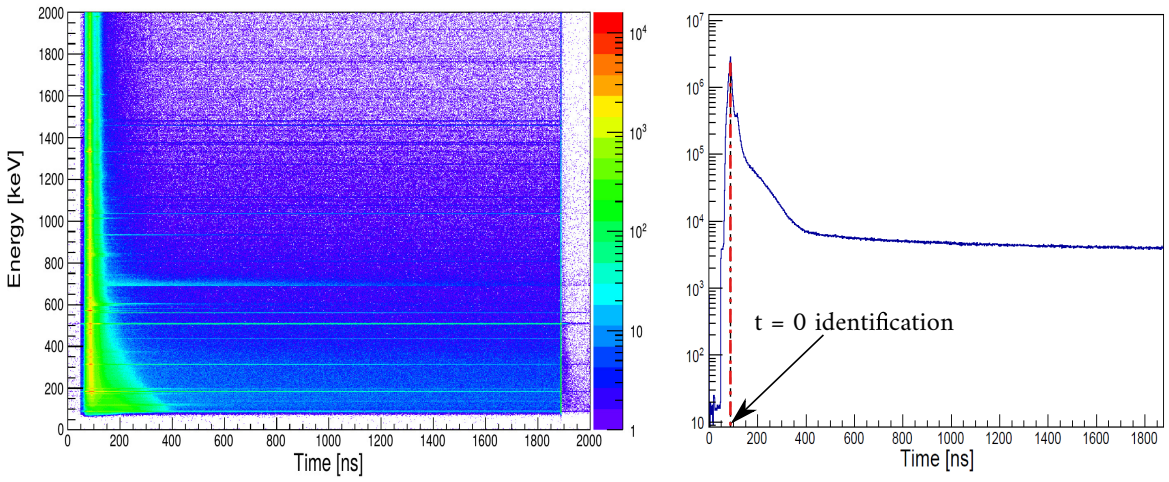

Figure 4.6 – On left two-dimentional histogram of energy vs. time. On right projection of Energy-time matrix on time axis which is used to make t = 0 identification.

the spectra. But, this assumptions are not valid in real life and we have to correct for this. After correcting for the relative efficiency of the 8 Ge crystals, we will obtain the same level of background for the time spectra. then, the experimental R(t) function will be constructed by taking the difference between different detector combinations divided by their sum.

For the 563 keV and 315 keV transitions in ^{66}Cu, the signs of the observed oscillations amplitude are consistent with a pure M2 and (E1) transitions respectively. It allows us to confirm the multipolarity of this transitions. A R(t) function with a good statistics was observed for the 563 keV (M2) and 315 keV (E1) transitions for the HPGe detectors placed at the horizontal plane ($\phi = 90°$) (see Figure 4.7. In Figure 4.8 the R(t) function for the 1017 keV (M2) transition in ^{65}Ni is presented for the same detector combination.

In order to obtain the alignment value, this function was fitted by a theoretical curve using Equation 3.8, with the oscillation amplitude ($amp_{R(t)}$) as free parameter, and its uncertainty was determined using χ^2 minimization procedure. The period of oscillation is propotional to the Larmor frequency which is related to g factor and the magnetic field in the site. In order to fit the R(t) function, one needs to know the g factor of the nuclear state of interest and the strength of the hyperfine field in the site. In this work Geo et al. [3], the g factor of ^{65m}Ni g = -0.294(4) and the value of hyperfine Ni-Ni are well known. In another work the g factor of

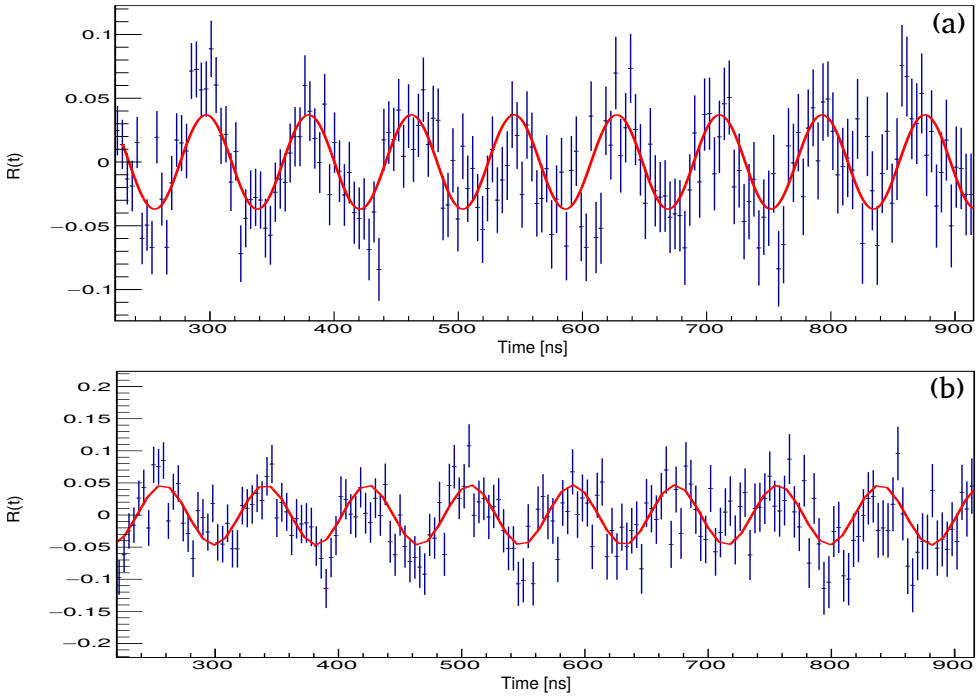

Figure 4.7 – R(t) function, obtained for (a) the transition 315 keV and (b) 563 keV in ^{66}Cu from the HPGe detectors placed at horizontal plan (ϕ=90°).

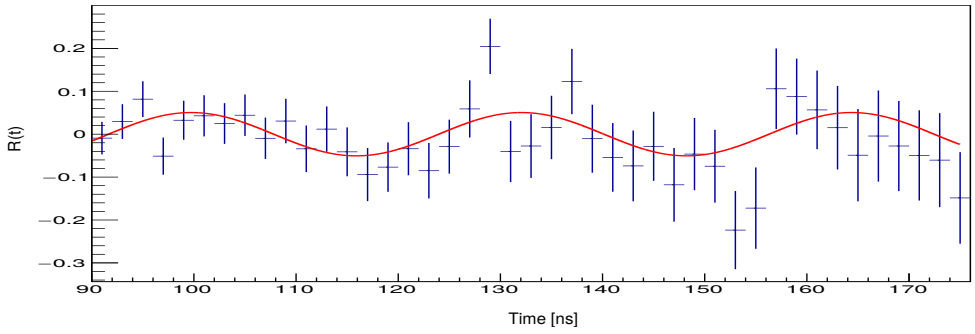

Figure 4.8 – R(t) function, obtained for the transition 1017 KeV in ^{65}Ni from the HPGe detectors placed at horizontal plan (ϕ=90°).

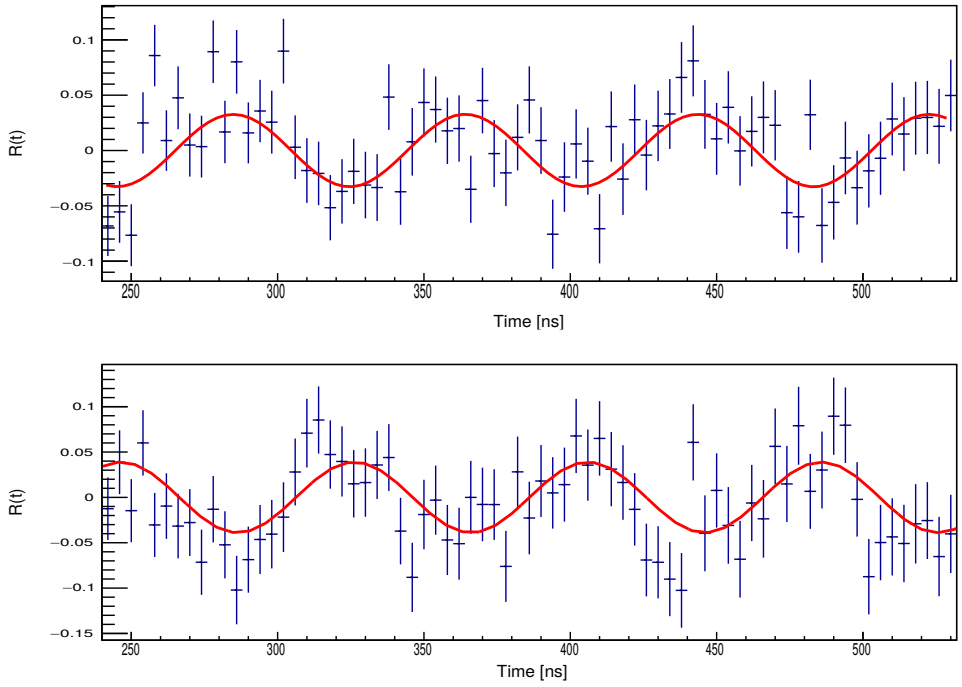

Figure 4.9 – R(t) function, obtained for (a) the transition 315 keV and (b) 563 keV in ^{66}Cu from the HPGe 1 and 19 detectors placed at non-horizontal plan ($\phi \neq 90°$).

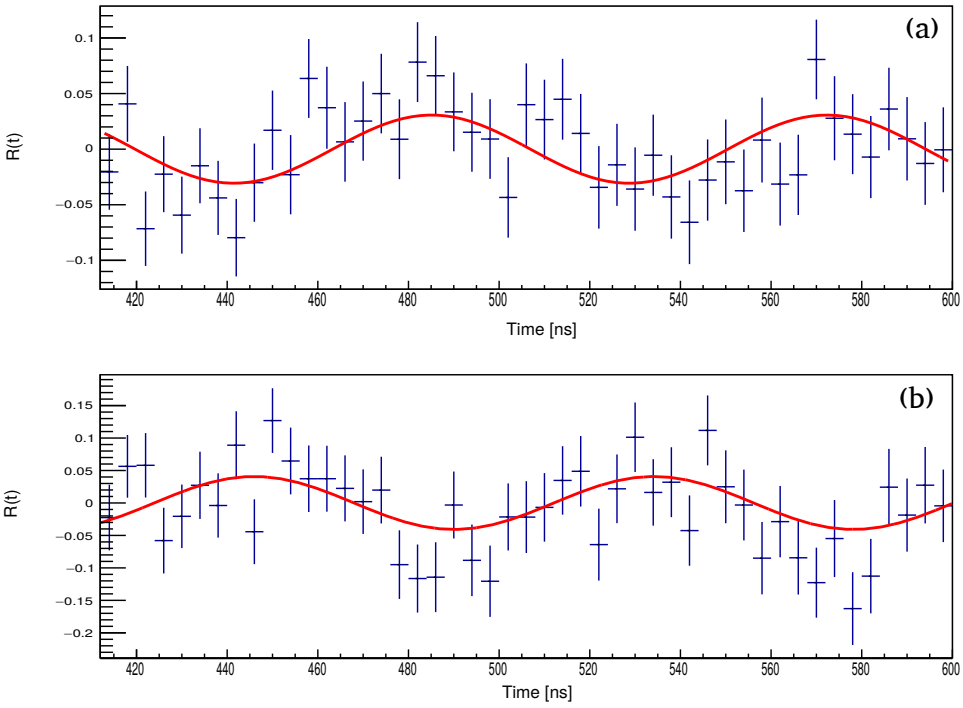

Figure 4.10 – R(t) function, obtained for (a) the transition 315 keV and (b) 563 keV in ^{66}Cu from the HPGe 10 and 18 detectors placed at non-horizontal plan ($\phi \neq 90°$).

^{66m}Cu isotope g = 0.178(2) and the hyperfine Cu-Ni are well determined [4].

The level of spin orientation (B_2 coefficient) was deduced from the amplitude ($amp_{R(t)}$) of the R(t) function (Figures : 4.7, 4.8, 4.9 and 4.10) for 315 keV, 563 keV and 1017 keV γ-ray transitions in ^{66}Cu and ^{65}Ni respectively. The A_2 coefficient is calculated based on the assumption of a pure E1 and M2 transitions as A_2 = -0.403 for the isomeric transition 563 keV (M2), A_2 = 0.313 for the 315 keV (E1) and A_2 = -0.41 for the isomeric transition 1017 keV (M2). The spin orientation values for decay transitions discussed above for different detector combinations are presented in the Tables 4.2, 4.3 and 4.4. By considering all a γ-rays in

Transitions	$amp_{R(t)}$	B_2 coefficient
315 keV	-0.037(2)	-0.150(12)
563 keV	0.042(3)	-0.141(10)

Table 4.2 – The level of spin-orientation in ^{66}Cu determined by using HPGe (ID = 2,8,16 and 22) positionned at horizontal plan (ϕ=90°).

HPGe ID	Transitions	$amp_{R(t)}$	B_2 coefficient
1 and 19	315 keV	-0.034(3)	-0.129(17)
1 and 19	563 keV	0.043(4)	-0.127(15)
10 and 18	315 keV	-0.029(5)	-0.127(20)
10 and 18	563 keV	0.036(6)	-0.126(21)

Table 4.3 – The level of spin-orientation in ^{66}Cu determined by using HPGe positionned at $\phi \neq 90°$.

Transitions	$amp_{R(t)}$	B_2 coefficient
1017 keV	0.05(1)	-0.158(28)

Table 4.4 – The level of spin-orientation in ^{65}Ni determined by using HPGe (ID = 2,8,16 and 22) positionned at horizontal plan (ϕ=90°).

coincidence with particles detected by the segmented annular detectors (see Figure 4.11 and 4.12), one can study rigorously the level of the spin orientation in multi-transfer/incomplete fusion reaction. Hence, the results of spin orientation for decay transitions for the same de-

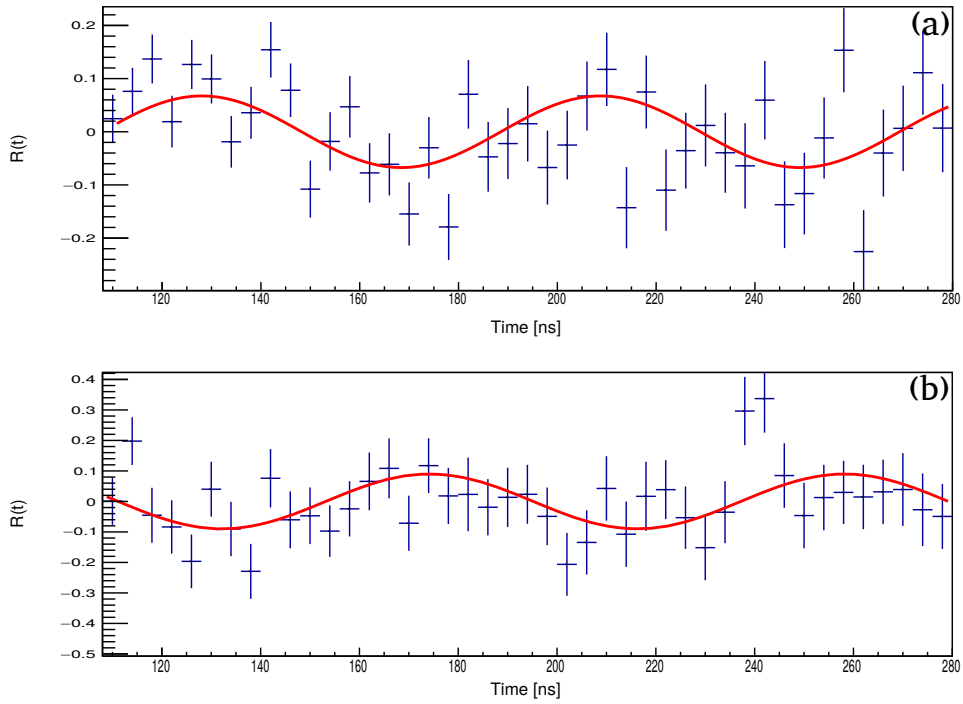

Figure 4.11 – R(t) function, obtained for (a) the transition 315 keV and (b) 563 keV in ^{66}Cu from the particle detectors in coincidence with HPGe detectors placed at horizontal plan (ϕ=90°).

tector combination are presented in the Table 4.5. The alignment of the isomeric ensemble

Transitions	amp$_{R(t)}$	B_2 coefficient
563 keV (^{m66}Cu)	0.09(1)	-0.308(7)
1017 keV (^{m65}Ni)	0.07(2)	-0.227(11)

Table 4.5 – Considering γ-particle coincidences. The level of spin-orientation in ^{66}Cu and ^{65}Ni determined by using HPGe (ID = 2,8,16 and 22) positionned at horizontal plan (ϕ=90°) and 8 fold-segmented particle detectors.

was obtained using Equation 3.9. The deduced amplitude of 0.09(1) (See Figure 4.11(b)) for the 563 keV transition corresponds to A = 14(3)% for ^{66}Cu, and The amplitude of 0.07(2) (see

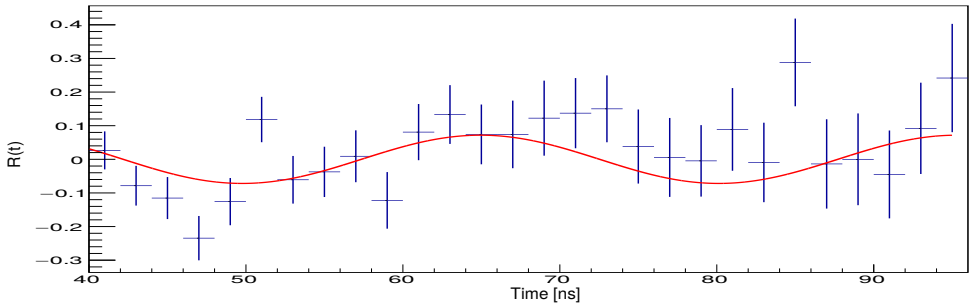

Figure 4.12 – R(t) function, obtained for the transition 1017 KeV in ^{65}Ni from the particle detectors in coincidence with HPGe detectors placed at horizontal plan (ϕ=90°).

Figure 4.12) for 1017 keV transition corresponds to A = 26(2)% for ^{65}Ni. An additional systematic uncertainty of about 2% can be added based on the uncertainty of the magnetic field at the target position. To sum up, the level of spin-orientation in incomplete fusion reac-

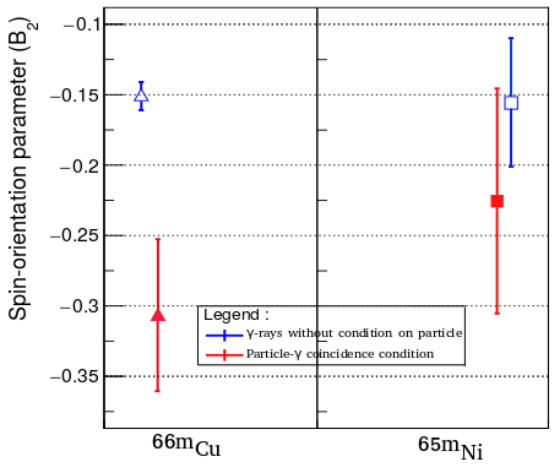

Figure 4.13 – The level of spin orientation (B_2 in ^{66m}Cu and ^{65m}Ni). In blue is shown the obtained value of spin orientation without any condition on particles detection. The reds one show the B_2 with particle-γ coincidence.

tion was studied for two configurations of HPGe detectors, detectors placed on a horizontal plane (ϕ = 90°) and a non-horizontal plane (ϕ ≠ 90°). The results obtained in case of ^{66}Cu are represented. In addition, the degree of spin-orientation was estimated for the total events without any condition on particle detection (only the detected γ-rays), and for γ coming in

coincidence with particle (See Figure 4.13). It can be concluded that a sgnificant amount of spin alignment (~ 20%) is present in multi-transfer/incomplete fusion reaction mechanism. Such an amount of alignment in an incomplete fusion reaction encourages to investigate the nuclear structure by this reaction mechanism. By using this mechanism, there is no limit on the half-time of the nuclear states which we want to investigate. In addtition, one can take advantages of the radioactive beam to study the properties of several neutron-rich nuclei.

4.1.2 g factor of the first excited state in ^{22}Ne

A ^{22}Ne beam was used during one week to perform a general test on the set-up, and to calibrate the plunger device. The idea is to collect enough data to determine the calibration parameters, and induce them later in the final procedure to extract a g factor of the first-excited state in ^{28}Mg. A code written in C/C++ language has been used to convert the data to a "root" format. During the conversion, all particles with low energies are excluded from the analysis by applying a threshold, because they are difficult to make correlation with γ-rays due to the background noise. Each event is recorded and ordered in time and module, constituting a MINIBALL event. However, at this stage there is no correlation established between hits and their types (particles or gammas). When the ADC (particles) and DGF (γ-rays) channels are calibrated, then the prompt and random particle-γ coincidences have to be identified. The time window of difference between the detection of γ-ray and a particle in the same EBIS pulse, is used to determine the particle-γ correlations. From figure 4.14a, the prompt coincidence window is defined by the true coincident events in peak about 300 ns wide. Where, the events outside of the peak (or random events) are recorded from the correlation of γ-rays from the ambient radioactivity with an elastically scattered beam particles. In order to increase the signal/noise ratio a subtraction of these random events is done on the prompt events. Random-coincidence subtraction has been done by setting an appropriate "randoms" gate on the time spectra and subtracting the random coincidences from the total coincidence events. The random gate was applied on the flat parts of the time, normalized to the peak width as shown on Figure 4.14a. Thus the γ-ray background, originating from radioactive decay and/or reactions, was subtracted by the particle-γ coincidence condition. An example of energy spectra of ^{22}Ne is shown in Figure 4.14b. The HPGe (including

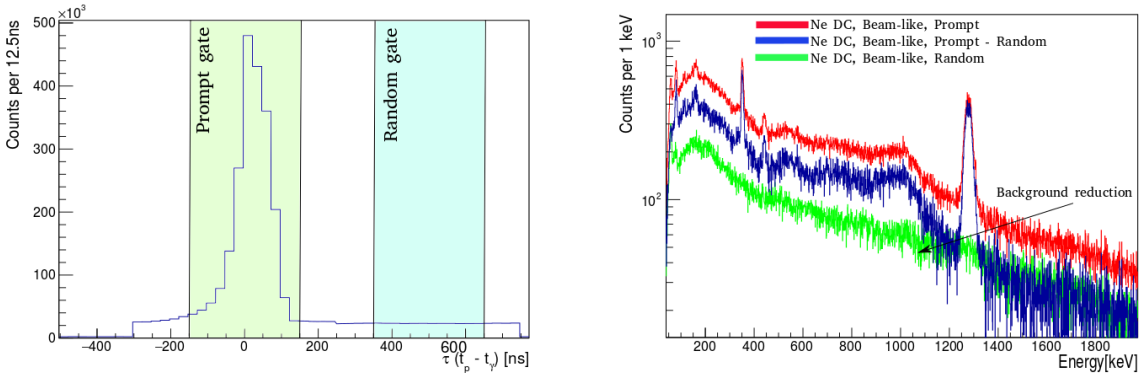

(a) (b)

Figure 4.14 – (a) Time difference Particle-γ for ^{22}Ne with a zoom on the prompt peak and random zone, (b) Energy spectra of ^{22}Ne for the projectile kinematic zone with Doppler correction and background subtruction.

23 cores) energy calibration has been done with ^{152}Eu and ^{133}Ba sources. Thus, one has to check for drifts occurring during the experiment. This is done by shifting the position of the main peak to the initial position for each different run. Figure 4.15 shows that the electronics and detectors are stable and don't have problems with gain drifts.

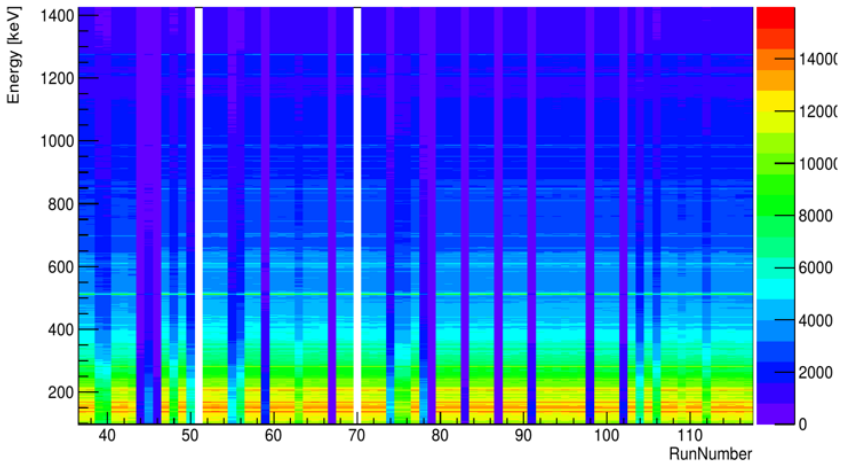

Figure 4.15 – γ-rays energy Vs. number of runs. MINIBALL detectors show a good gain stability throughout the experiment time.

The particle detectors are separated into 4 quadrants segmented in 16 strips on the front and in 12 sectors on the back. Eight spectras of particle energies versus identification number of each segment (16 annulars and 12 sectors) which had to be aligned with respect to each

other see figure 4.16. The figure 4.17shows the distribution of particles detected in the 4

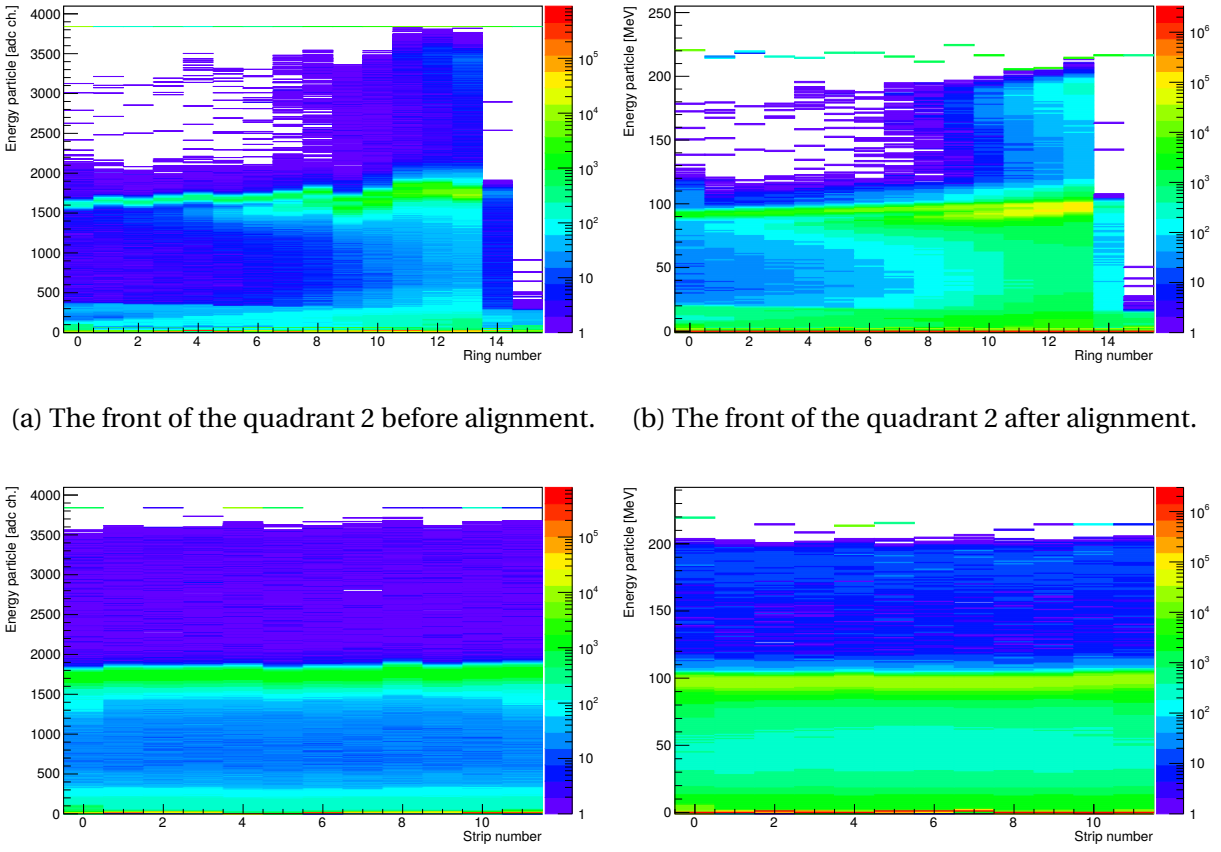

(a) The front of the quadrant 2 before alignment.

(b) The front of the quadrant 2 after alignment.

(c) The back of the quadrant 2 before alignment.

(d) The back of the quadrant 2 after alignment.

Figure 4.16 – Particle energy vs. identification number of the CD detector.

quadrant of CD detector in polar coordinates for the Coulomb excitation reaction of ^{22}Ne with the ^{93}Nb target and ^{181}Ta degrader. One can confirm that the CD detector is well centred along the beam axis and the beam is not deviated to be observed. One can also see that one sectorial strip was not operational during the experiment because it was damaged and/or its bande wire was broken. Another confirmation of the broken segment can be found in Appendix A.3, where, all operational segments were tested by using an α source. During this experiment, the recoil and beam particles are detected by the CD detector. Determining the distance from the CD detector to target will be used in the data analysis to define the coverage angles , in the laboratory frame, of the CD detector. By using an α source of ^{226}Ra, at the target position, we measured the distance between the target and the CD detector. The distances for the CD quadrants were calculated by integrating the highest-energy alpha

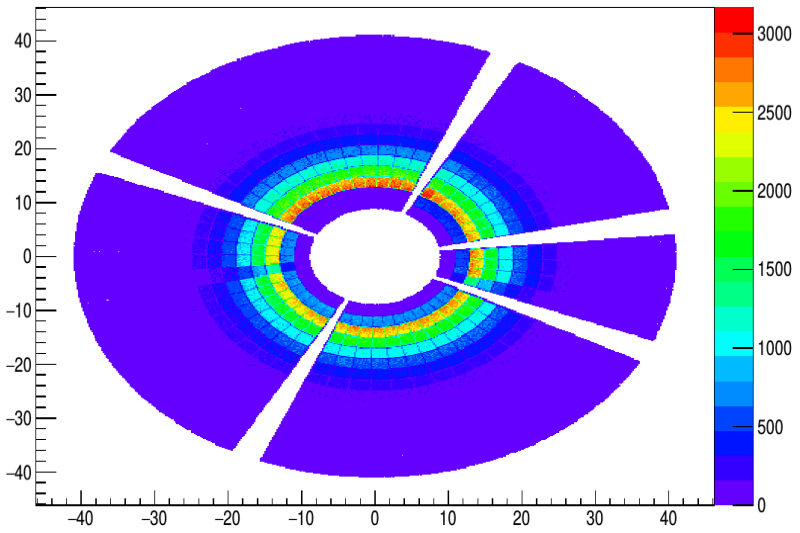

Figure 4.17 – Centering of the beam. The damaged sectorial strip was removed during the data analysis.

peak in the front ring segment (f1 to f16) for each of the four quadrants. The points on figure 4.18 were fitted with solid angle Ω formula as a function of distance against the measured intensity. The used formula to fit data is based on the solid angle included in a cone which is equal to 2π(1-cosθ), where θ is the angle at the top cone. The solid angle under which one sees a disc of inner radius l_{inner} and outer radius l_{outer} located perpendiculary to a distance l_d is:

$$\Omega(sr) = 2\pi \left[\left(1 - \frac{l_d}{\sqrt{l_d^2 + l_{outer}^2}} \right) - \left(1 - \frac{l_d}{\sqrt{l_d^2 + l_{inner}^2}} \right) \right] \tag{4.3}$$

The distances of each quadrant suggest that quadrant 4 is slightly further away from the target (∼ 1 mm) than others quadrants. The fit result gave an average CD-target distance of 34.47(18) mm.

During our experiment we used a plunger setup with its holder target. This latter was shifted with an offset of 1.2 (1) mm from the MINIBALL target holder position. One needs to take into account this offset and correct the CD-target distance to be 33.27(8) mm.

The resulting angles of the CD detector are listed in the Table 4.6. A calibration of the annular and sector strips of CD detectors is performed with an α source of ^{226}Ra. However, in our experiment, the energy range of αs is far from the kinetic energy of the beam particles (∼ 110 MeV). To cover the energy range of our experiment, an additional Coulomb excitation of

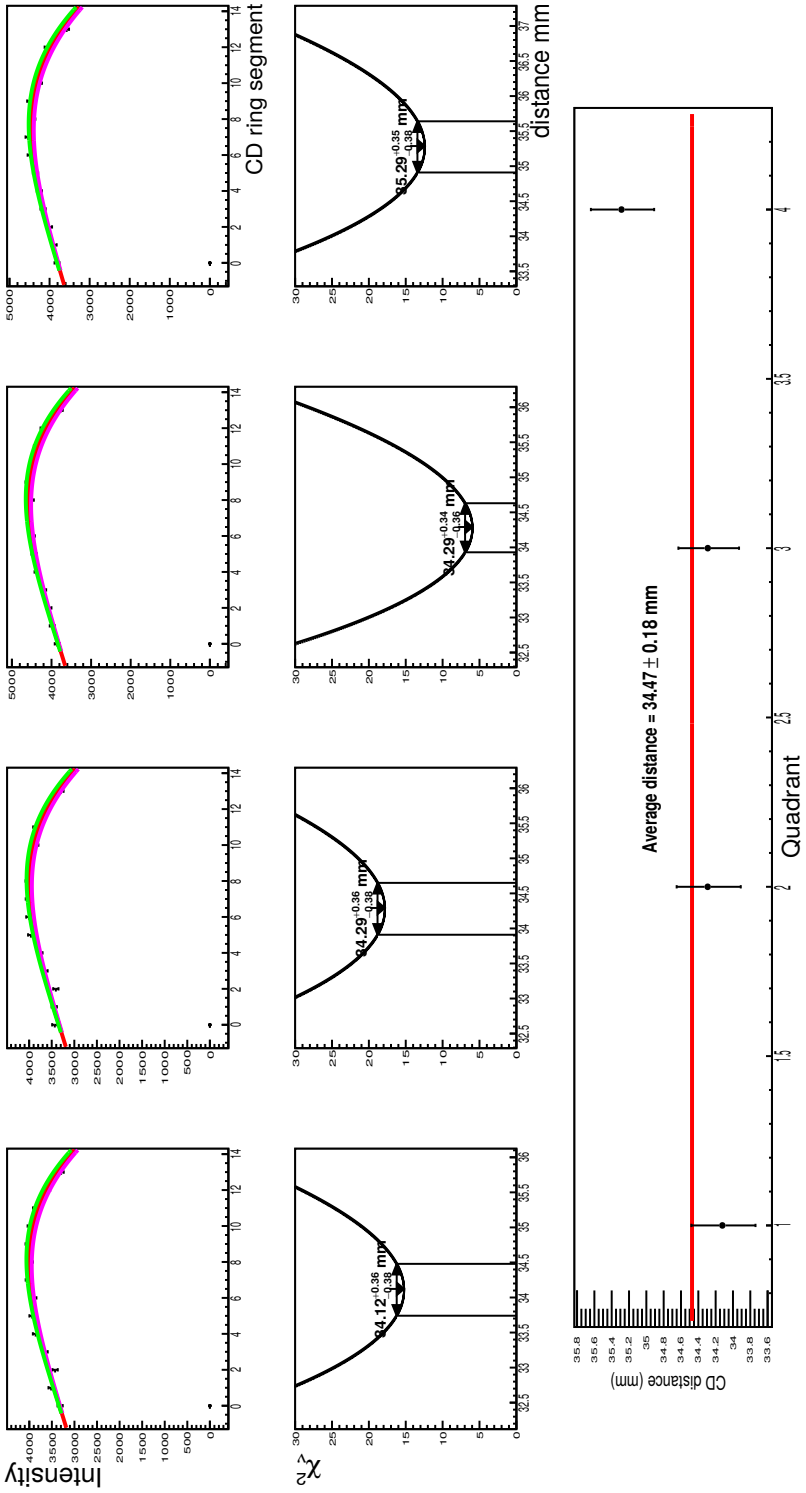

Figure 4.18 – Determination of CD detector-to-target distance. The four figures at the top show for each quadrant the intensity of the alpha in each ring segment. The upper and lower error bars are indicated in green and purple color respectively. The figures at the bottom show the values of reduced χ^2_ν ($\chi^2/\mathrm{N}df$) and the average distance of the four quadrants from the target position.

Annular strip ID	θ_{in}(degree)	θ_{out}(degree)	θ(degree)
15	15.2	18.2	16.67
14	18.3	21.2	19.78
13	21.4	24.2	22.78
12	24.3	27.0	25.65
11	27.1	29.7	28.38
10	29.8	32.2	30.99
9	32.3	34.6	33.46
8	34.7	36.9	35.79
7	37.0	39.0	38.00
6	39.1	41.0	40.08
5	41.1	42.9	42.04
4	43.0	44.7	43.89
3	44.8	46.4	45.63
2	46.5	48.0	47.27
1	48.1	49.5	48.81
0	49.6	50.9	50.26

Table 4.6 – List of angles of each annular strip constituting the CD detector.

^{22}Ne on ^{196}Pt target has been used to properly calibrate the CD detector.

The obtained kinematics, of Coulomb excitation of ^{22}Ne on ^{93}Nb target and ^{181}Ta degrader, has been compared to LISE++ [5] calculations with the incident beam E_{beam} ~ 5.505 MeV/A. The results obtained with LISE++ are shown for different depths of interaction of the target, see figure 4.19. These results are in a good agreement with the experimental values. The resulting kinematics show a good seperation between the projectiles and recoils. A narrow kinematic zone has been used to integrate the γ-ray intensities. The identification particle nature in the CD detector is shown in figure 4.19. A beam-like and target-like spectra, for a restricted kinematics zone indicated on Figure 4.19, are given in Figure 4.20. An example of a γ-ray spectrum used in the g-factor measurement of the first-excited state in ^{22}Ne, is shown

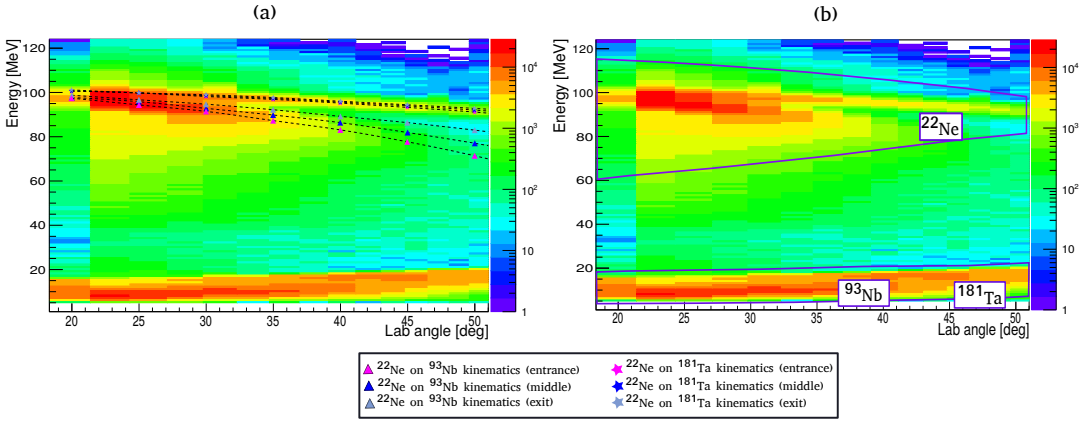

Figure 4.19 – (a) The obtained kinematic for an ^{22}Ne incident beam energy of 5.505 MeV/u on ^{93}Nb/^{181}Ta target/degrader, (b) The restricted gates correspond to the projectile ^{22}Ne and Recoil ^{93}Nb/^{181}Ta kinematics.

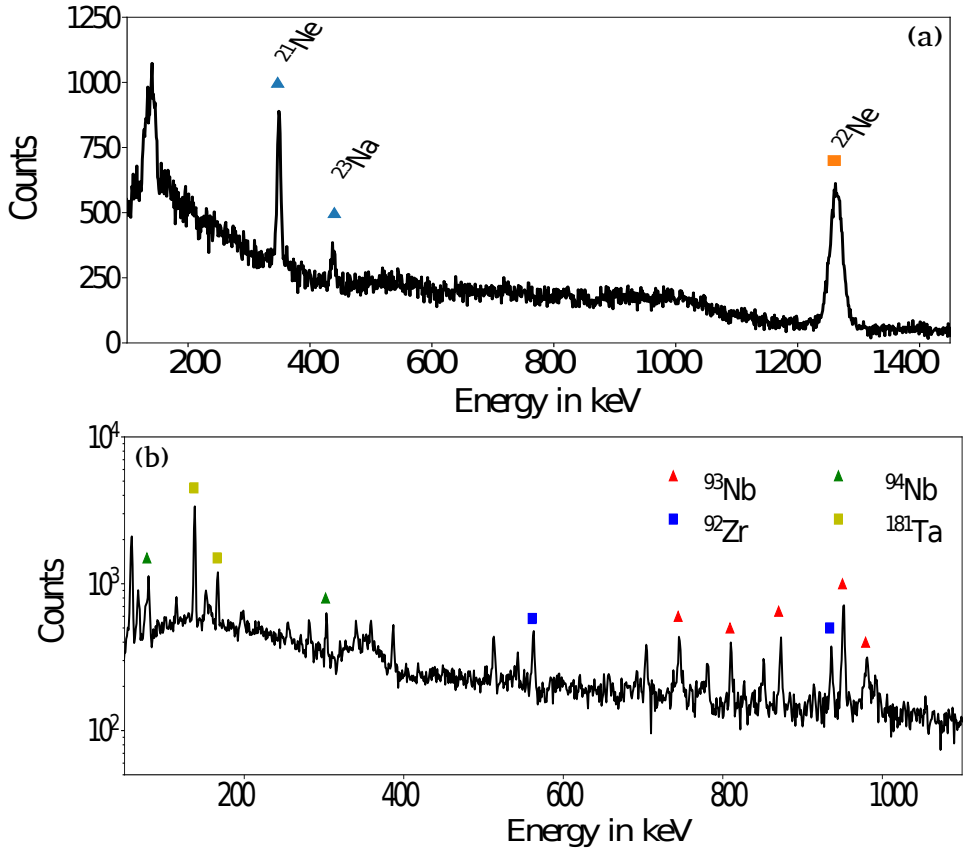

Figure 4.20 – A γ-rays energy spectra, (a) for a beam-like and (b) a target-like Doppler corrected and backgroud subtruction.

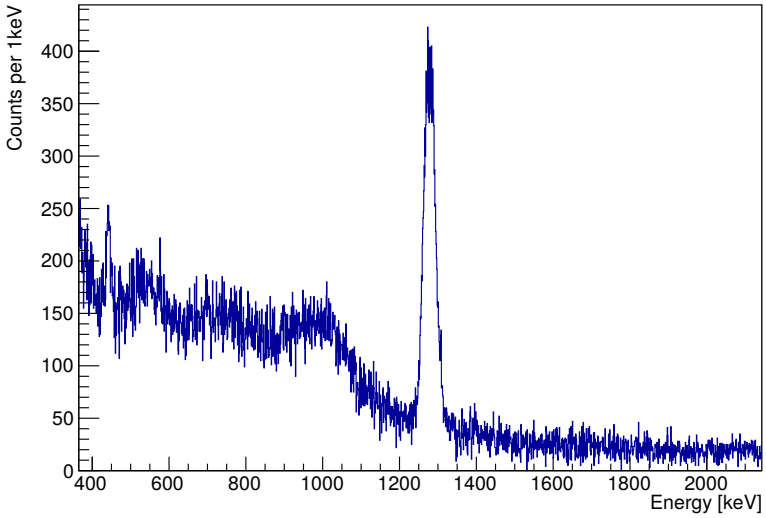

Figure 4.21 – Random-subtracted γ-ray spectrum collected at 1 μm plunger separation, showing the ^{22}Ne $2^+ \rightarrow 0^+$ 1274 keV photopeak. Doppler corrected data for all γ-ray detectors in coincidence with particle detector is shown.

in Figure 4.21. The intensity of the peak, corresponding to the $2^+ \rightarrow 0^+$ transition of ^{22}Ne was determined for all particle-γ combinations.

Doppler effects have an important influence on the nuclear spectroscopy of fast moving ions. Gamma radiation emitted by a nucleus in motion has a different energy than the actual transition energy. The frequency of the rays is lower if the nucleus moves away from the observer, and higher when it moves towards the observer. A good Doppler corrections depends highly on the CD calibration (energy and position). Even the HPGe detector energy and position calibrations have been done carefully, the position resolution of the CD detector stay an important factor to obtain a high quality Doppler corrections. Also, when the beam pass through the target/degrader and the dead layer of the CD detector, it is slowed down. Using the SRIM packages [6], the stopping power calculations have been done for each nucleus of the beam-like by taking into account the beam velocity of each ion before and after passing through the Ta (1.1 mg/cm^2 degrader) and Al (0.7 μ m dead layer) matter.
The relativistic version of the Doppler shift formula for a γ-ray moving with velocity v is :

$$E_{lab} = \frac{\gamma E_0}{1 - \beta cos\theta} \tag{4.4}$$

where E_γ and E_0 ($E = h\nu$) are respectively the measured and the original (body-fixed frame) γ-ray transition energies, and θ is the angle between the detection of the γ-ray and the direction of motion of the ion. The Doppler-corrected spectra in Figure 4.21 were produced using the polar angle information between the HPGe and the particle detectors. Doppler shift of the $2^+ \rightarrow 0^+$ transition of ^{22}Ne at different polar angles is shown in figure 4.22 The black solid line is the Doppler shifted transition of 2^+ state of ^{22}Ne. One can determine the average ion

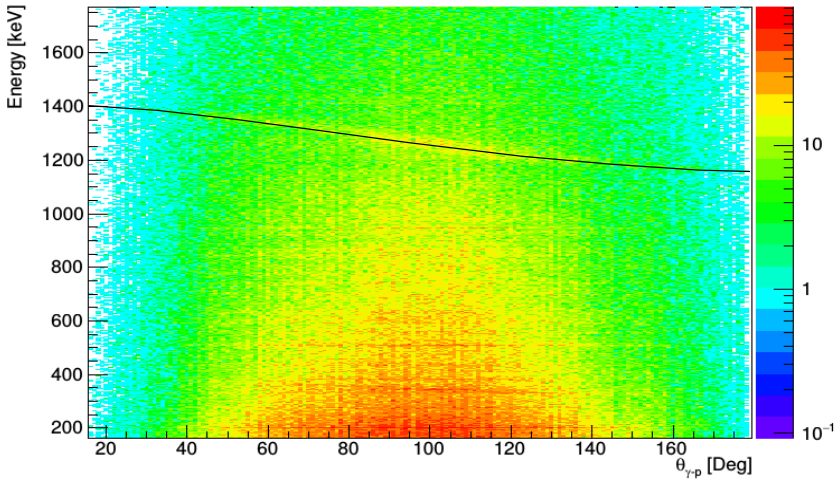

Figure 4.22 – γ-ray versus the angle between the particle and the gamma with Nb target and Ta reset foil for 900 μm distance.

velocities (β) by using the measured Doppler shift of the de-excitating γ-rays. To determine the experimental velocities of the ions after the target we used the longest distances. The reason to use the longest distance is that most of the gamma-ray intensities would be coming for decays between the target and the reset foil. The Doppler shifted excited ^{22}Ne γ-rays for each angle were fitted with Gaussian to determine the peak position and its sigma value. The obtained values were fitted with Equation 4.4 to identify the $\beta = v/c$ value. The longest distance analyzed for the Ta reset foil is (900 μm) for which we got β = 0.0961(14). Using LISE++ physical calculator, one can obtain a value of β = 0.0966.

In order to analyze the data, one can take the ratio of angular correlations, based on Equation 2.56, between the unperturbed W_1(t = 0.2 ps) and the W_2(t = 1.3 ps) at maximum perturbation (See figure 4.23). Then, an experimental particle-γ angular correlations, following Coulomb excitation of ^{22}Ne on ^{93}Nb, have been performed for each individual core in MINI-

BALL combined with 47 sector segmentations of the CD detector (1081 combinations) (See figure 4.24).

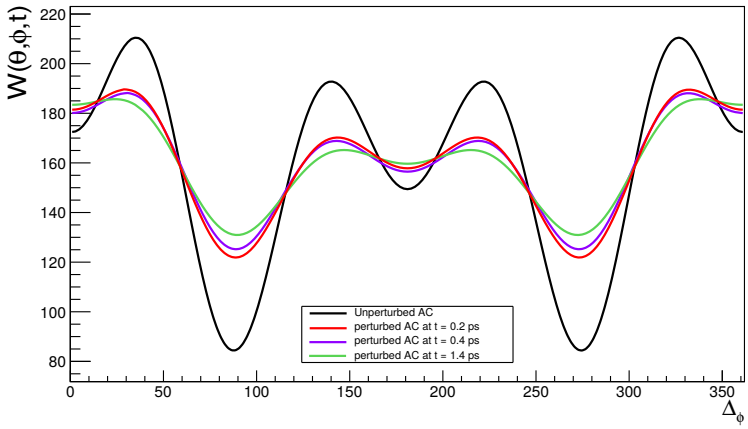

Figure 4.23 – Particle-γ angular correlation for ^{22}Ne excited on Nb target. The unperturbed and perturbed correlations are shown by different colors.

The 1081 time-dependent angular correlations were ordered according to the amplitude of the oscillations and whether the γ-ray intensity should increase, $W^{\uparrow}(T)$, or decrease, $W^{\downarrow}(T)$, with time. Here T is the flight time of the excited ions, related to the target-reset foil separation, D, by $T = D/\langle v cos\theta_p \rangle$, where θ_p represents the emission angles of scattered particles on the front side of the detector particle. The five hundred and seventy eight particle-γ combinations increase in magnitude initially by factors ranging from about (+)0.897% to about (+)10.12%. The remaining 503 particle-γ combinations initially decrease in magnitude by factors between (-)0.011% and (-)28.23%. Ratios of the coincidence γ-ray intensity corresponding to $W^{\downarrow}(T)/W^{\uparrow}(T)$ were performed.

$$R(T) = \left(\frac{W_i^{\downarrow}(T)}{W_i^{\uparrow}(T)} \right) \tag{4.5}$$

The $W^{\downarrow}(T)/W^{\uparrow}(T)$ ratios lost their sensitivity, when a small amplitude of the oscillations are averaged with ratios showing a large amplitude of the oscillations. The data set was therefore analyzed by performing ratios for each experimental distance. The obtained result is shown in Figure 4.25. The n = 357 combinations showing the largest amplitude of the oscillations are labeled "strong postive", while n = 56 ratios showing a moderate amplitude are labeled "intermediate positive", and n = 56 combinations showing a weak amplitude are

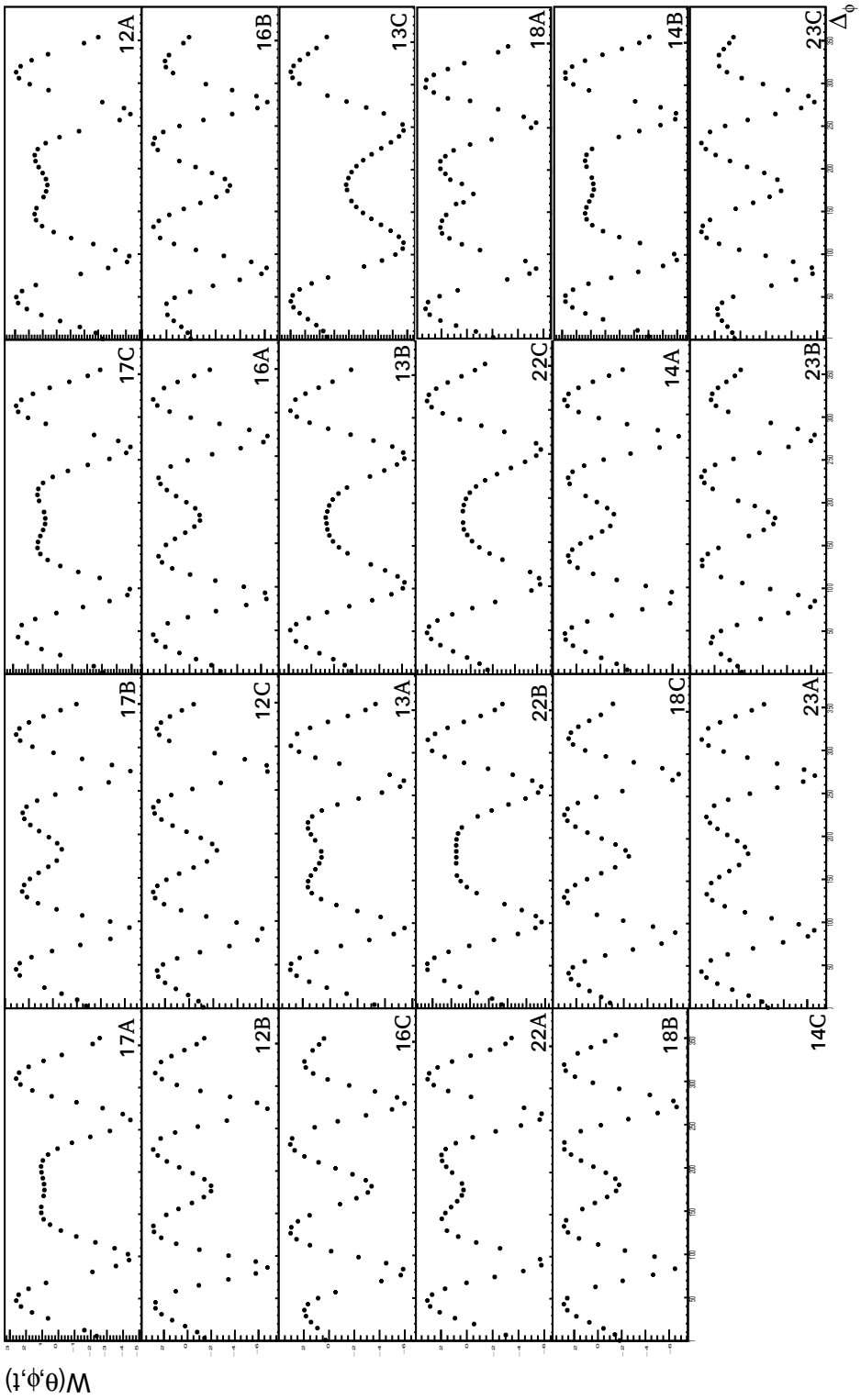

Figure 4.24 – Particle-γ angular correlations for ^{22}Ne excited on Nb target. The angular correlations were calculated at t_1 = 0.1 ps (for unperturbed case) and t_2 = 1.3 ps (for perturbed case). For all HPGe cores combined with 47 sector segmentations, the angular correlation is calculated as : $W(\theta,\phi,t) = [W_1(t_1) - W_2(t_2)]/[W_1(t_1) + W_2(t_2)]$.

labeled "weak positive". A further n = 109 pairs show a small amplitude. Because of the symmetry of the particle-detector and γ-detector arrays, certain particle-γ detector combinations should show the same angular correlations at all times. Ratios of such combinations should show a null effect, labeled "null". One can see that the most important part of the statistics it is collected by the combinations showing the largest amplitude of the oscillations "strong" (33% "negative" and 33% "positive"). The medium and weak combinations show 17% together of the total statistics, and 17% left in null combinations. Therefore, it is obvious to use the "strong" combinations, in order to construct the R(t) function. In the Table 4.7 it is presented the "strong" particle-γ combinations of all HPGe cores and their corresponding number of the segmentation sectors in CD detector. The g factor was determined from the fits to the experimental data, as shown in Figure 4.25.

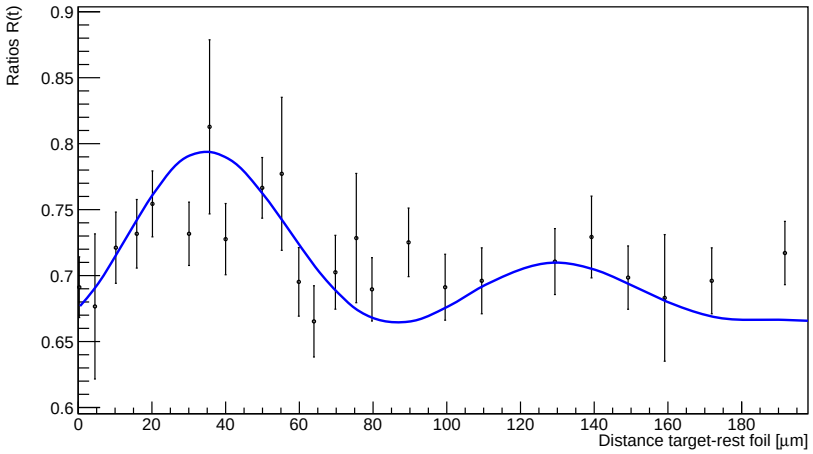

Figure 4.25 – R(t) ratio for 25 target-rest foil distances, and fit code [7] based on detailed parameters of the experiment. The frequency of oscillation gives the g factor.

A. E. Stuchbery's computer code was used to fit the experimental data [7]. This code is developed in order to model in details the experimental parameters. It is based on the given formula in section 3.5.2, equation 2.56 and the Coulomb-excitation calculations [8]. Following the same procedure as for the experimentasl data, the R(t) function are constructed and categorized in "strong", "intermediate", "weak" and "null" combinations. The fitting of the data is similar to the procedure in Kusoglu et al. work [9].

The value of the hyperfine field is evaluated to be $B_{1s}(0)$ = 16.70 kT (see Table 3.7).

The fit of the R(t) function, which has a strong oscillations, gives a g = 0.421(30). This value is

given the only the statistical uncertainties.

Additionally to the statistical errors, the systematic errors are indroduced in the calculation of the incertainty on the final value of the g factor. The systematic errors are given by an uncertainties from the CD detector-to-target distance of about 0.08 mm, from lifetime of first-excited state of interest of about 0.1 ps, and from the velocity β of about 0.0014. The obtained g factor is therefore $g = 0.421 \pm 0.030$ (statistical) $\pm$ 0.020 (systematic) or $g = 0.421(36)$, in good agreement with theory calculations, but diffrent from the previous value, $g = 0.326(12)$ [10].

	Strong		Intermediate		Weak		Null	
HPGeID	(↑)	(↓)	(↑)	(↓)	(↑)	(↓)	(↑)	(↓)
17A	10	16	8	0	6	1	4	2
17B	19	14	1	3	1	1	5	3
17C	15	15	4	1	4	1	4	3
12A	17	16	3	0	3	1	6	1
12B	16	17	4	1	0	5	2	2
12C	21	16	0	1	3	1	1	4
16A	16	17	1	3	3	1	4	2
16B	16	17	1	1	3	2	3	4
16C	18	15	2	3	2	1	3	3
13A	17	15	4	1	2	1	5	2
13B	8	13	0	3	4	2	13	4
13C	6	15	4	0	4	3	4	11
22A	17	14	4	0	2	1	2	7
22B	7	17	3	1	9	1	6	3
22C	9	11	2	1	1	3	14	6
18A	19	13	2	2	1	1	6	3
18B	17	18	1	3	1	0	5	2
18C	19	16	2	0	0	2	4	4
14A	19	16	2	1	1	2	3	3
14B	18	16	3	0	2	0	5	3
23A	18	18	2	1	0	2	3	3
23B	19	17	0	2	2	1	2	4
23C	16	16	3	1	2	2	5	2

Table 4.7 – Combinations between All HPGe cores with sectors of the CD detector (23 cores X 47 sectors). For each combination, the angular correlation Particle-γ show different larger of amplitude. For example, core 17A combined to 10 sectors of CD detector show a positive higher "strong" amplitude (first line).

4.2 Bibliography

[1] J.Bleck, R.Butt, K.H.Lindenberger, W.Ribbe, W.Zeitz. Magnetic Moments, Lifetimes, and γ-Decay of the Lowest 6^- States in ^{64}Cu and ^{66}Cu. *Nuclear Physics A*, 197:620–630, (1972). 74

[2] G.Georgiev et al. g-factor measurement of the $9/2^+$ isomeric state in ^{65}Ni. *J.Phys.(London)*, (G31, S1439), (2005). 74

[3] G. Georgiev et al. g factor of the $9/2^+$ isomeric state in ^{65}Ni from transfer reaction. *The European Physical Journal A*, pages 351–356, (2006). 75

[4] E. LohmannK. FreitagTh. SchaeferR. Vianden. The magnetic hyperfine field at Cu in Fe, Co and Ni and the magnetic moment of the 41 keV, 2^+ state of^{62}Cu. *Hyperfine Interactions*, 77(1):103–110, (December 1993). 78

[5] LISE Group. LISE++ Package. (Jul. 2012). 86

[6] Ziegler, James F.; Ziegler, M. D.; Biersack, J. P. SRIM - The stopping and range of ions in matter. *Nuclear Instruments and Methods in Physics Research*, 268, (Jun. 2010). 88

[7] Stuchbery A.E. (unpublished). computer code TDRIV MODEL. ix, 92

[8] Alder K. and Winther A. Coulomb Excitation. *Academeic Press:New York and London*, page p 303, (1996). 92

[9] A. Kusoglu et al. Nuclear g-factor measurement with time-dependent recoil in vacuum in radioactive-beam geometry. *Physical Review Letters*, (2015). 92

[10] R.E.Horstman, J.L.Eberhardt, P.C.ZalmH.A.Doubt, G.Van Middelkoop. Recoil-distance measurements of the g-factor of ^{22}Ne(2_1^+). *Nuclear Physics A*, 275:237–245, (1977). 93

Chapter 5

Discussion

Contents

5.1 Alignment in incomplete fusion reaction

The results presented in the section 4.1.1 show that the amount of spin alignment is significant in incomplete fusion reactions (A = 14(3)% for ^{66}Cu and A = 26(2)% for ^{65}Ni). Up to now, incomplete fusions reactions have been observed to have their origine from the peripheral collisions. The incomplete fusion mechanism has been extensively studied, however, no clear picture of the process has been drawn. In this thesis, the study of spin alignment was performed with the incomplete fusion reaction induced by a ^{7}Li beam. This type of reaction has widely been employed for γ-rays spectroscopy studies. These studies reported the incomplete fusion reaction as a promising way to offer access to states with a high angular momentum in neutron-rich heavy nuclei. Otherwise, the region of neutron-rich nuclei is inaccessible by standard fusion-evaporation reactions using stable beam-target combinations. A variety of dynamical models have been proposed to describe the products associated with the incomplete fusions reactions. The Break-Up Fusion is one of the proposed models used to fit the experimental data [1]. Indeed, with ^{7}Li-induced incomplete fusion reaction, there is a significant probability of a ^{7}Li beam nucleus breaking up, with a triton being captured while a α is emitted. Dracoulis et al. [2] in their work confirm that in such process it is possible to populate states with a relatively higher angular momentum with using a ^{7}Li-induced incomplete fusions reactions. It has also been shown in Judson's et al. work [3], the excited states in ^{125}Sb with spins up to 23/2 have been studied following the ^{124}Sn(^{7}Li,α2n)^{125}Sb incomplete fusion reaction at beam energy 37 MeV. To sum up, using the incomplete fusion reaction mechanism, there is no limit on the half-time of the nuclear states which we want to investigate. Also, this reaction mechanism allows producing high spin states in final reactions products. Then, one can employ this reaction mechanism at radioactive nuclear beam facilities in order to provide a new opportunity for studying nuclear structure and reaction in a wider degree of freedom of isospin.

In the future, the plan is to employ the incomplete fusion reactions induced by neutron-rich radioactive beams on ^{7}Li target. This type of reaction is defined in inverse kinematics. The information of interest, in an inverse kinematic, can be deduced by studying either the kinematical properties of the heavy residue and/or of the light fragment. Due to forward

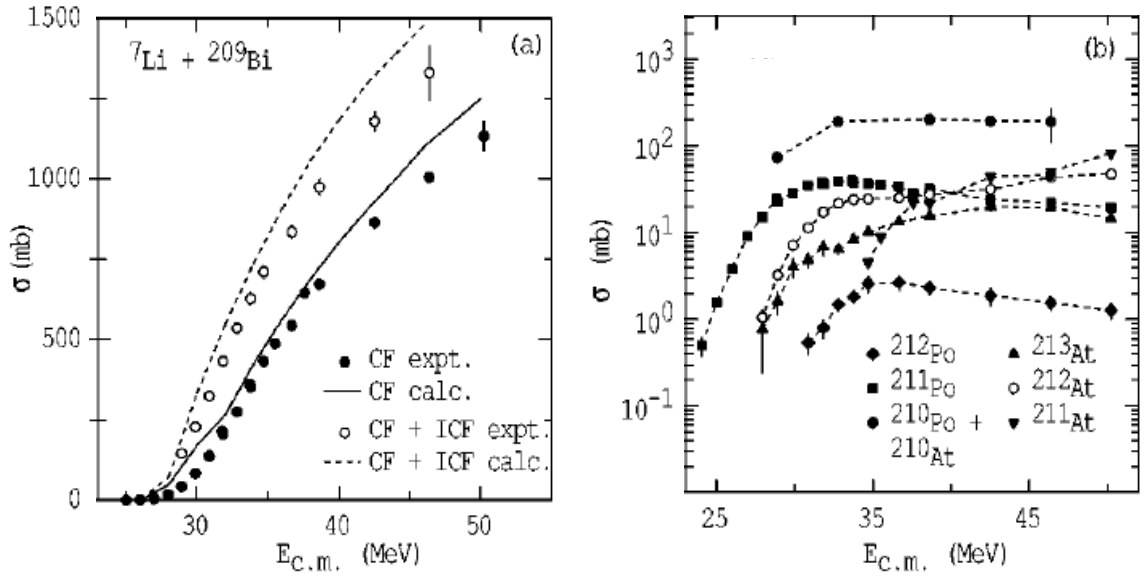

Figure 5.1 – Cross section in incomplete fusion [1].

focusing of the reaction, the detection efficiency of heavy residue is increased and the high velocity allows for use of relatively thick targets, and therefore the yield in inverse kinematics can be maximized by increasing the target-thickness/Z ratios. However, because of the characteristics of the heavy fragment, its detection is only possible if its lifetime is long enough to reach the detection system. Moreover, when the mass of the projectile becomes higher, the angular center of mass resolution which can be obtained becomes rather poor. On another hand, one can measure the energy and diffusion angle of light recoil fragment in order to construct the kinematics of the reaction. In our considered reaction, the neutron-rich radioactive beams on ^{7}Li target that we intend to employ in *g*-factor measurements will allow to populate species in the process associated with the transfer of triton to the beam-like nuclei, and followed by emission of a α particles. The triton and α particles arise from the Break-up process of the weakly bound ^{7}Li (^{7}Li → α + t, binding energy S_{α} = 2.5 MeV). The detection of this α particles allow producing a very clean trigger of the neutron-rich radioactive beams on ^{7}Li reactions mechanism.

A few years ago, B. Fornal et al. [4] proposed to study at REX-ISOLDE the incomplete fusion processes with ^{94}Kr radioactive beam on a ^{7}Li target. The studied reaction channel

^{7}Li(^{94}Kr,αxn) led to the production of the excited ^{97}Rb and then the evaporation of one or two neutrons will populate ^{95,96}Rb nuclei. During this experiment, for a total of four days beam time of ^{94}Kr at 2.84 MeV/nucleon and a beam intensity of $2 \cdot 10^5$ pps on 1.5 mg/cm^2 thick ^{7}LiF target, they collected a total of 10^4 events of $\alpha - \gamma$ coincidences from ^{7}Li(^{94}Kr,αxn) reaction. This experiment demonstrates the feasibility of such study with incomplete fusion reaction induced by a neutron-rich radioactive beam. In *g*-factor experiments, one needs a beam intensity of at least 10^6 pps to apply any technique used in *g*-factor measurement. Today, such demands of intensity and beam energy will be solved using, for example, a radioactive ion beam at HIE-ISOLDE.

From this work, the deduced amount of spin alignment in incomplete fusion reaction and the advantage obtained by using the radioactive ion beam in study of the nuclear structure, further studies will be proposed in the future with the appropriate beam and technique requests for the *g*-factor measurement.

5.2 ^{28}Mg and ^{22}Ne cases

Magnetic moment measurements of the first-excited states in ^{28}Mg can provide a valuable information on the composition of the nuclear wave function. The even-even nuclei with a *sd*-shell were the object of many studies, resulting in elaboration of "universal" *sd* (USD) shell model Hamiltonians [5]. Our experimental *g*-factor will be confronted to theoretical calculation in *sd* model with the USDA and USDB interactions and the corresponding empirical M1 operators. The USDA and USDB interactions update the universal *sd* shell Hamiltonian USD to include an additional data on neutron-rich nuclei.

The nuclear structure in the region around N = 16 is still not well understood. For the neutron-rich oxygen isotopes, the N = 16 shows features of a magic number. This magicity of the N = 16 sub-shell closure is due to the enhancement of the gap between $\nu s_{1/2}$ and $\nu d_{3/2}$ single-particle energies (SPE). By adding protons to the $\pi d_{5/2}$ orbital the SPE of $\nu d_{3/2}$ is moved down, and therefore, the gap is reduced between $\nu s_{1/2}$ and $\nu d_{3/2}$. This reduction of gap is originated from the tensor spin-orbit interaction between the $\nu d_{3/2}$ and $\pi d_{5/2}$ orbitals [6].

The g(2^+) factors of the magnesium isotopes from ^{24}Mg to ^{32}Mg are shown in Figure 5.2. The

shell-model calculations performed with USDB interaction predict that the g-factor of the first-excited state in ^{26}Mg to be almost double that the value calculated for the ^{24}Mg. From the recent measurements, the g factor of the first-excited state in the N = Z nucleus ^{24}Mg is near g = 0.5 [7], and a new measurement for ^{26}Mg at the Australian National University confirm the predictions of the shell-model calculations. Although the previous results are in good agreement with USDB shell model, the model breaks down when the so-called island of inversion is approached. For the ^{32}Mg is indicated on figure 5.2 that the sd model space predicts a g-factor value for the first-excited state g = + 1.6. However, Otsuka et al. used more realistic calculations in $sdpf$ model space and give a g = + 0.32, much smaller than the sd-shell model value [8]. For ^{30}Mg a g-factor is determined with the $sdpf$ model space to be also smaller than the sd-model value.

The measured ground-state g-factors of the odd-nuclei magnesium isotopes are mainly determined by the odd nucleon and are insensitive to the configuration of the core. Indeed, the measurement of $1/2^+$ ground-state moment in ^{31}Mg is well predicted by USDB shell model calculations, however, the USDB calculations push the $1/2^+$ state at an excitation energy above 2 MeV and it lost its character as ground-state in ^{31}Mg [9]. In parallel, the measurement of the first-excited 2^+ state moments is announced to be more sensitive to any configuration mixing close to the Island of Inversion than the ground states of the odd-A nuclei in this region.

Furthermore, the (2_1^+) states in ^{30}Mg is expected to contain a pf admixtures than the ground states. With the last result of ^{26}Mg with a g-factor value falling below the USDB calculations, it is necessary to go for more precise g-factors measurements on ^{26}Mg (2_1^+) state, and also on ^{28}Mg (2_1^+) state. A TDRIV experiment has been approved to run at ALTO (Orsay) to improve the precision on the ^{26}Mg g-factor. Therefore, the determination of how the g-factor of the first-excited states evolves as ^{32}Mg is approached, helps us to better understand the evolution of orbitals around the Island of Inversion region.

Finally, the g-factor of the 2_1^+ state of ^{28}Mg is sensitive to the $\nu d_{3/2}$ orbital position and the limit of the Island of Inversion on the chart of nuclides.

The $\nu s_{1/2}$ subshell is closed in ^{28}Mg which gives a $g(2_1^+)$ ~1, however, it is predicted that with the universal sd-shell interactions the g-factor varies between 0.680 and 0.737 with the USDA and USDB hamiltonians[10]. This variation can be interpreted by the change of the $\nu d_{3/2}$ SPE

position. The USDB Hamiltonian gives a better rms deviation, however, there is little difference in the wavefunctions of stable nuclides. One can make reference to USD and USDA to give an estimation of the theoretical uncertainty in the effective Hamiltonian. This uncertainty affects the g-factor at the level of ± 0.001.

In order to obtain a precise measurement of the g-factor, a run with a stable ^{22}Ne beam under the same conditions as with the radioactive ^{28}Mg would allow calibrating the entire system. The excitation energy of the 2_1^+ state in ^{22}Ne, and its lifetime allow applying a TDRIV measurement. As the first g-factor measurement on stable ^{24}Mg isotope at ALTO (Orsay), this experiment has also validated the new TDRIV method at HIE-ISOLDE at CERN. The fit of the R(t) function, with a complex code developed by A.E. Stuchbery [11], gives a D_0 offset value for the R(t) function to be 8 µm. This result will allow determining with a high precision the absolute target-degrader distance. Later, the obtained calibration parameters will be used to fit the constructed R(t) function of ^{28}Mg, which will improve the uncertainty on g-factor measurement with the radioactive beam.

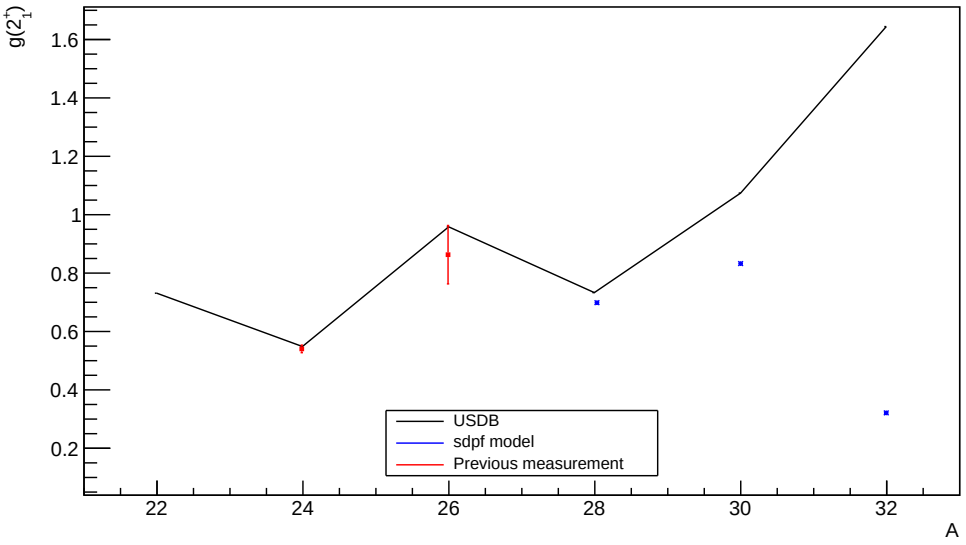

Figure 5.2 – g-factor of the first-excited state from ^{24}Mg to ^{32}Mg nuclei in the *sd* shell calculation (USDB in red and sdpf model in bleu) compared to the experimental measurements.

Finally, the g-factors of the first-excited state for N = Z + 2 nuclei in the *sd* shell calculation, with the USDB interaction and the corresponding empirical M 1 operators, are dis-

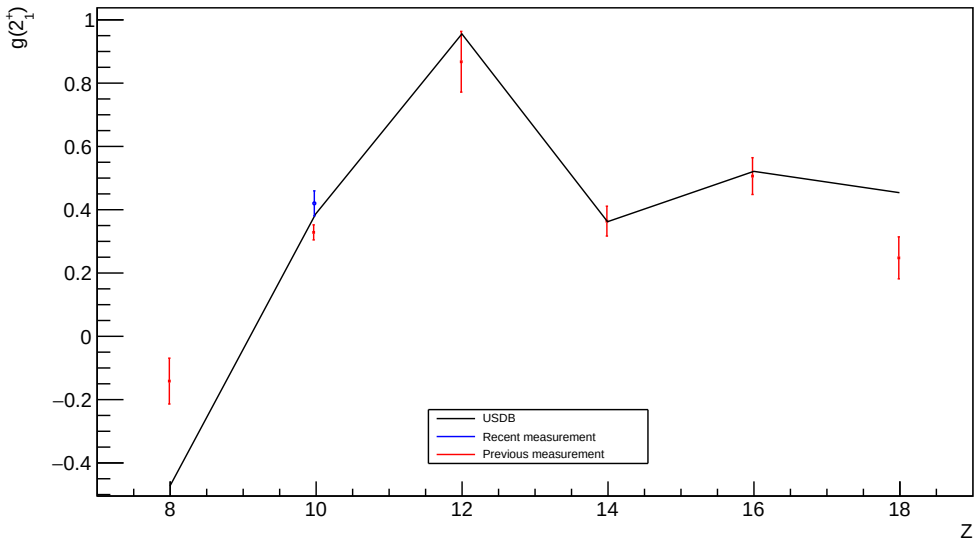

Figure 5.3 – g-factor of the first-excited state for N = Z + 2 nuclei in the *sd* shell calculation compared to the experimental measurements.

played in Figure 5.3. In an earlier paper it has been shown that the measurement lead to four mutually consistent values for the g-factors of ^{22}Ne :g_1 = 0.303 ±0.020, g_2 = 0.351 ±0.032, g_3 = 0.352 ±0.030 and g_4 = 0.329 ±0.023 [12]. As is evident from Figure 5.3, the experimental values for ^{18}O and ^{22}Ne are not in agreement with the values from the theory. Applying a TDRIV method on^{22}Ne a new level of precision is reached. As it is shown on Figure 5.3, the new measurement is in agreement with theoretical calculations $g(2^+)$ = 0.39. Shell-model calculations predict that the g-factor of the first-excited state in the N = Z + 2 nucleus ^{22}Ne is increased from g = 0.325, given by the literature. Our experiment confirms these predictions with a $g(2)^+$ = 0.421(36).

5.3 Bibliography

[1] M. Dasgupta, D. J. Hinde, K. Hagino, S. B. Moraes, P. R. S. Gomes, R. M. Anjos, R. D. Butt, A. C. Berriman, N. Carlin, C. R. Morton, J. O. Newton, and A. Szanto de Toledo. Fusion and breakup in the reactions of ^{6}Li and 7Li nuclei with ^{209}Bi. *Phys. Rev. C*, 66(041602(R)), (2002). ix, 97, 98

[2] G. D. Dracoulis, A. P. Byrne, T. Kibédi, T. R. McGoram and S. M. Mullins. Incomplete fusion as a spectroscopic tool. *Journal of Physics G: Nuclear and Particle Physics*, (). 97

[3] D. S. Judson, A. M. Bruce, M. J. Taylor, G. D. Dracoulis, T. Kibédi, A. P. Byrne, K. H. Maier, P. Nieminen and J. N. Orce. Microsecond isomers in 125Sb. (). 97

[4] B. Fornal et al. Gamma spectroscopy of n-rich ^{95,96}Rb nuclei by the incomplete fusion reaction of ^{94}Kr on ^{7}Li:. *Experiment proposal*. 98

[5] B. Alex Brown and W. A. Richter. New "USD" Hamiltonians for the *sd* shell. *Phys. Rev. C*, 74(034315), (2006). 99

[6] Takaharu Otsuka, Rintaro Fujimoto, Yutaka Utsuno, B. Alex Brown, Michio Honma, and Takahiro Mizusaki. Magic Numbers in Exotic Nuclei and Spin-Isospin Properties of the NN Interaction. *Phys. Rev. Lett*, 87(082502), (2001). 99

[7] A. Kusoglu et al. Nuclear g-factor measurement with time-dependent recoil in vacuum in radioactive-beam geometry. *Physical Review Letters*, (2015). 100

[8] T.OtsukaM.HonmaT.MizusakiN.ShimizuY.Utsuno. Monte Carlo shell model for atomic nuclei. *Progress in Particle and Nuclear Physics*, 47:319–400, (2001). 100

[9] W. A. Richter, S. Mkhize, and B. Alex Brown. *sd*-shell observables for the USDA and USDB Hamiltonians. *Phys. Rev. C*, 78(064302), (2008). 100

[10] G.Georgiev et al. Nuclear moment studies of short-lived excited states towards the Island of Inversion. g-factor of ^{28}Mg (2^+) using TDRIV on H-like ions. . *Proposal to the ISOLDE and Neutron Time-of-Flight Committee*. 100

[11] Stuchbery A.E. (unpublished). computer code TDRIV MODEL. 101

[12] R.E.Horstman, J.L.Eberhardt, P.C.ZalmH.A.Doubt, G.Van Middelkoop. Recoil-distance measurements of the g-factor of ^{22}Ne(2_1^+). *Nuclear Physics A*, 275:237–245, (1977). 102

Chapter 6

Conclusions

Contents

6.1 Summary and conclusions

Using an incomplete fusion reaction mechanism, with a stable ^{7}Li beam impinging on a ^{64}Ni target, we determined a high degree of spin alignment. By applying a Time-Dependent Perturbed Angular Distribution method (TDPAD) an amount of spin alignment was obtained : A = 14(3)% for ^{66}Cu and A = 26(2)% for ^{65}Ni. This result opens a way to perform g-factor measurements with radioactive ion beam guided towards light-A targets, to study the nuclear structure of nuclei far from the stability line.

The present work demonstrates also the feasibility of the g-factor measurements of the short-lived first-excited states. Knowing that the majority of theoretical models are based on g-factor measurement of the ground-state, the first-excited state will allow to test this models and apply a good test on the purity of the wave function and its configuration. A robust method called Time-Dependent Recoil-In-Vacuum method (TDRIV) was applied on the first-excited state in ^{28}Mg. It allows to study N = 20 nuclear structure around the Island of Inversion, where the shell-gap can change significantly as a function of the number of protons.

The present results on ^{22}Ne allow to calibrate the whole system and determine the absolute target to rest foil distance, which allow to determine the g-factor in ^{28}Mg with a high precision.

In summary, we have validated a new method for measuring the g-factors of excited nuclear states with lifetimes in the picosecond regime. Measurements on stable isotopes like ^{22}Ne can reach new levels of precision and test nuclear model in ways that were not previously possible. We have obtained a different value of the $g(2_1^+)$ = 0.421(36), compared to the given value in literature $g(2_1^+)$ = 0.325(30). In the previous experiment, the g-factor measurement in ^{22}Ne was determined with a diffrent method named Transient Field (TF). This measurement required much stronger transient field to determine a g-factor with a good precision. Also, in this work the ^{22}Ne was used only to calibrate and to test the system before the use of the radioactive beam.

6.2 Perspectives

Knowing that the TDRIV method was designed for application to radioactive beams, the present work is the proof of application of this method with a radioactive ^{28}Mg beam. The successful first time application of the TDRIV method prepares the way for a future measurement on the neutron-rich nucleus ^{32}Mg in the island of inversion.

As mentionned in the previous section, the g-factor in ^{22}Ne is different from the given value in literature. The obtained value is unexpected and requires more investigations. Then, the obtained calibration parameters from the g-factor measurement in ^{22}Ne will be applied to the analysis of ^{28}Mg in order to extract the g-factor value of the first-excited state.

The determination of the g-factor of the first excited state in ^{28}Mg is still under investigation. During the experiment and due to some technical difficulties, the recorded statistic was very low for the case of the ^{28}Mg and the g-factor will need to be carefully determined.

Finally, we plan to employ the incomplete fusion reaction mechanism using radioactive beams, to study the properties of neutron-rich nuclei in inverse kinematics.

Appendix A

Appendix

A.1 Theoretical

A.1.1 Solid angle correction factor

The solid angle can be widened by increasing detector size or reducing distance between the source and the detector, then the count rate is increased, these manipulations necessarily reduce observed anisotropies by averaging over part of the correlation.
The observed angular correlation from finite size of γ-ray detector differs from the ideal correlation expected for point detectors. The attenuation factor Q_k is necessary to correct for the effect of the finite solide angle $d\Omega = sin\beta d\beta d\Phi$ of the detectors on the angular correlations. Q_k for a given detector depends on the γ-ray energy. In addition, they depend on the detectors used and their geometry, and the source-to-detector distance. The attenuation facor for a single detector is evaluated as:

$$Q_k = \frac{J_k}{J_0}, \tag{A.1}$$

where

$$J_k = \int P_k(cos\beta)(1 - e^{\tau x(\beta)})sin\beta d\beta. \tag{A.2}$$

For a coaxial detector, the β is the angle between the propagation direction of the γ-ray and the detector symmetry axis as shown in Figure A.1, τ is the γ-ray absorption coefiicient, and P_k are the Legendre polynomials. When x(β) is the path length through the detector traversed by the radiation incident on the crystal at an angle β with the axis, the absorption is propo-

tional to $(1-e^{\tau x(\beta)})$.

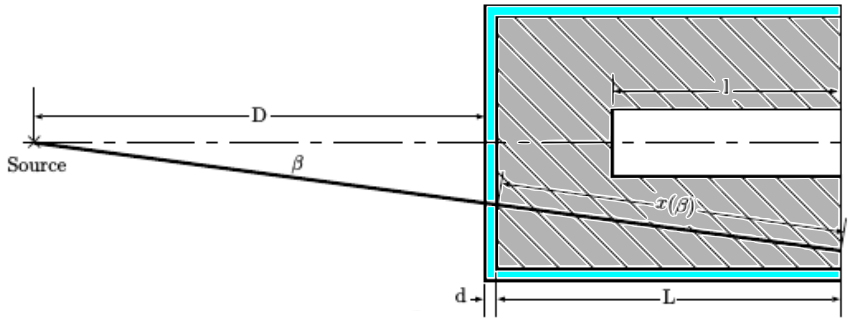

Figure A.1 – Geometry of source-detector configuration for calculation of solid angle correction for coaxial detectors.

A.1.2 Wigner-D matrix

The Wingner-D matrices can be related to spherical harmonics in a special case:

$$\mathrm{D}^{k*}_{q0}(\Delta\phi,\theta_\Upsilon,0)=(-1)^q\sqrt{\frac{4\pi}{2k+1}}\mathrm{Y}^k_{-q}(\theta_\Upsilon,\Delta\phi), \tag{A.3}$$

where $\mathrm{Y}^k_{-q}(\theta_{\Upsilon,\Delta_\phi})$ is the spherical harmonic. Applying the Condon-Shortley phase convention, the spherical harmonics can be defined as:

$$\mathrm{Y}^m_l(\theta,\phi)=(-1)^m\sqrt{\frac{(2l+1)(l-m)!}{4\pi(l+m)!}}\mathrm{P}^m_l(cos\theta)e^{im\phi}, \tag{A.4}$$

where $\mathrm{P}^m_l(cos\theta)$ are the associated Legende functions. For $m=0$ these are equal to the Legendre polynomials $\mathrm{P}_l(cos\theta)$.

The angular correlation only depends on ϕ through the difference $\Delta\phi=\phi_\Upsilon-\phi_p$. The statistical tensor has following relation:

$$\mathrm{B}_{kq}(\theta_p,\phi_p)=\mathrm{B}_{kq}(\theta_p,0)e^{-iq\phi_p}=\mathrm{B}_{kq}(\theta_p)e^{iq\phi_p} \tag{A.5}$$

The dependence of B_{kq} on ϕ is given by a rotation matrix and the exponential can be expressed in the difinition of the spherical harmonic:

$$\begin{aligned}\mathrm{Y}^m_l(\theta_\Upsilon,\phi_\Upsilon)e^{-iq\phi_p}&=(-1)^m\sqrt{\frac{(2l+1)(l-m)!}{4\pi(l+m)!}}\mathrm{P}^m_l(cos\theta_\Upsilon)e^{im\phi_\Upsilon}e^{-iq\phi_p}\\&=\mathrm{Y}^m_l(\theta_\Upsilon,\phi_\Upsilon-\phi_p)\end{aligned} \tag{A.6}$$

A.2 Experimental

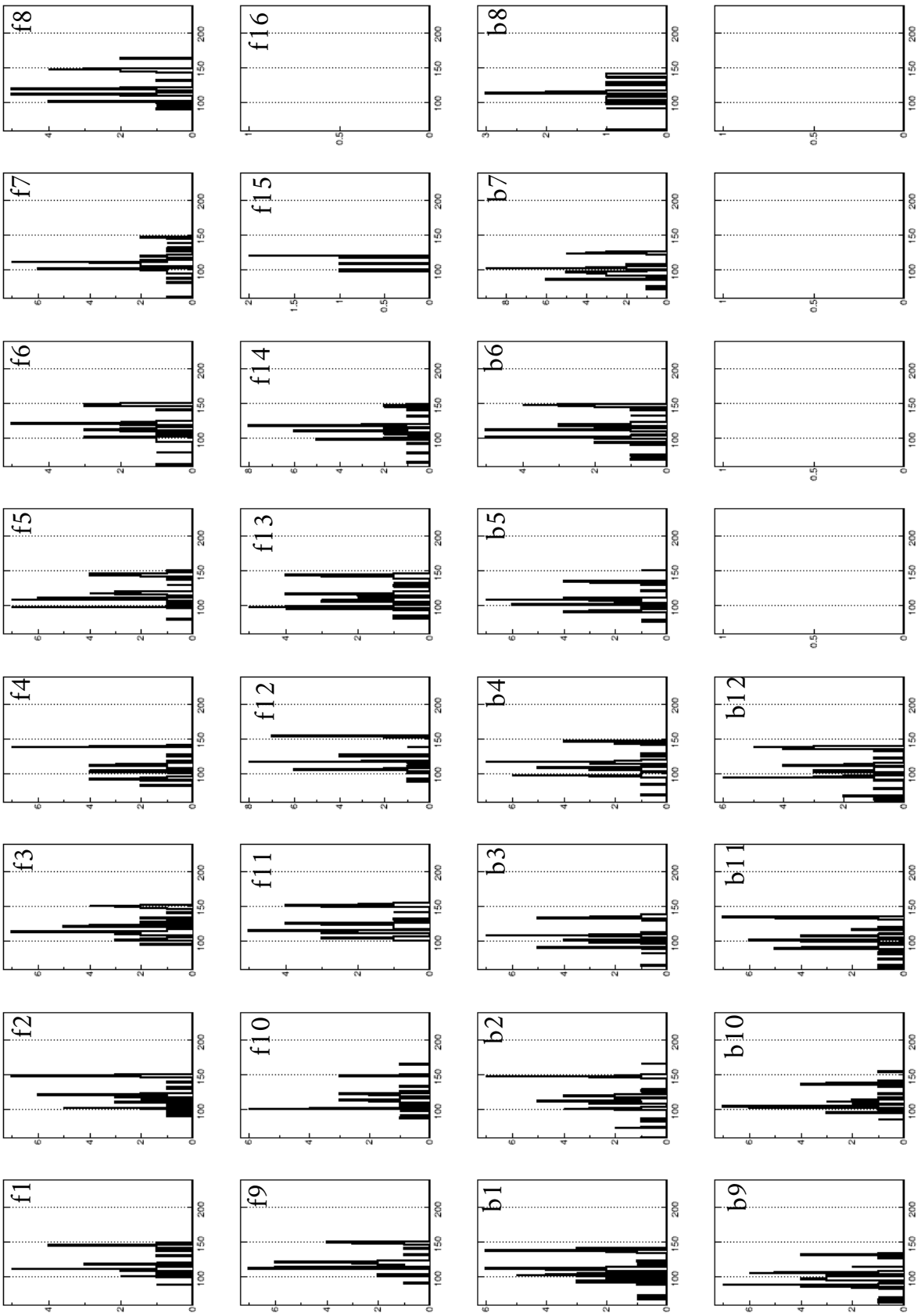

Figure A.2 – α energy recorded in each segment of quadrant 1 by using α-source ^{226}Ra.

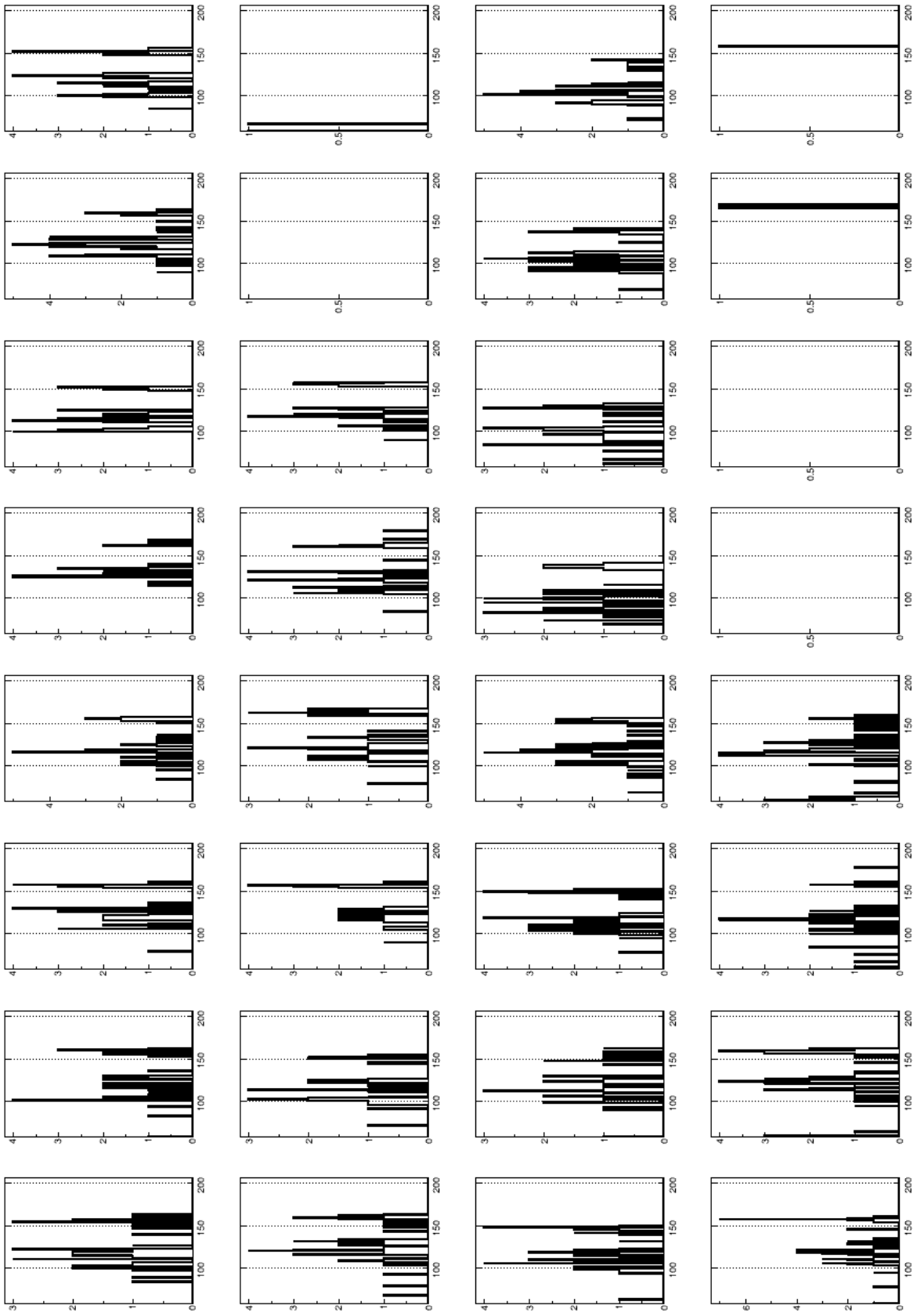

Figure A.3 – α energy recorded in each segment of quadrant 2 by using α-source ^{226}Ra.

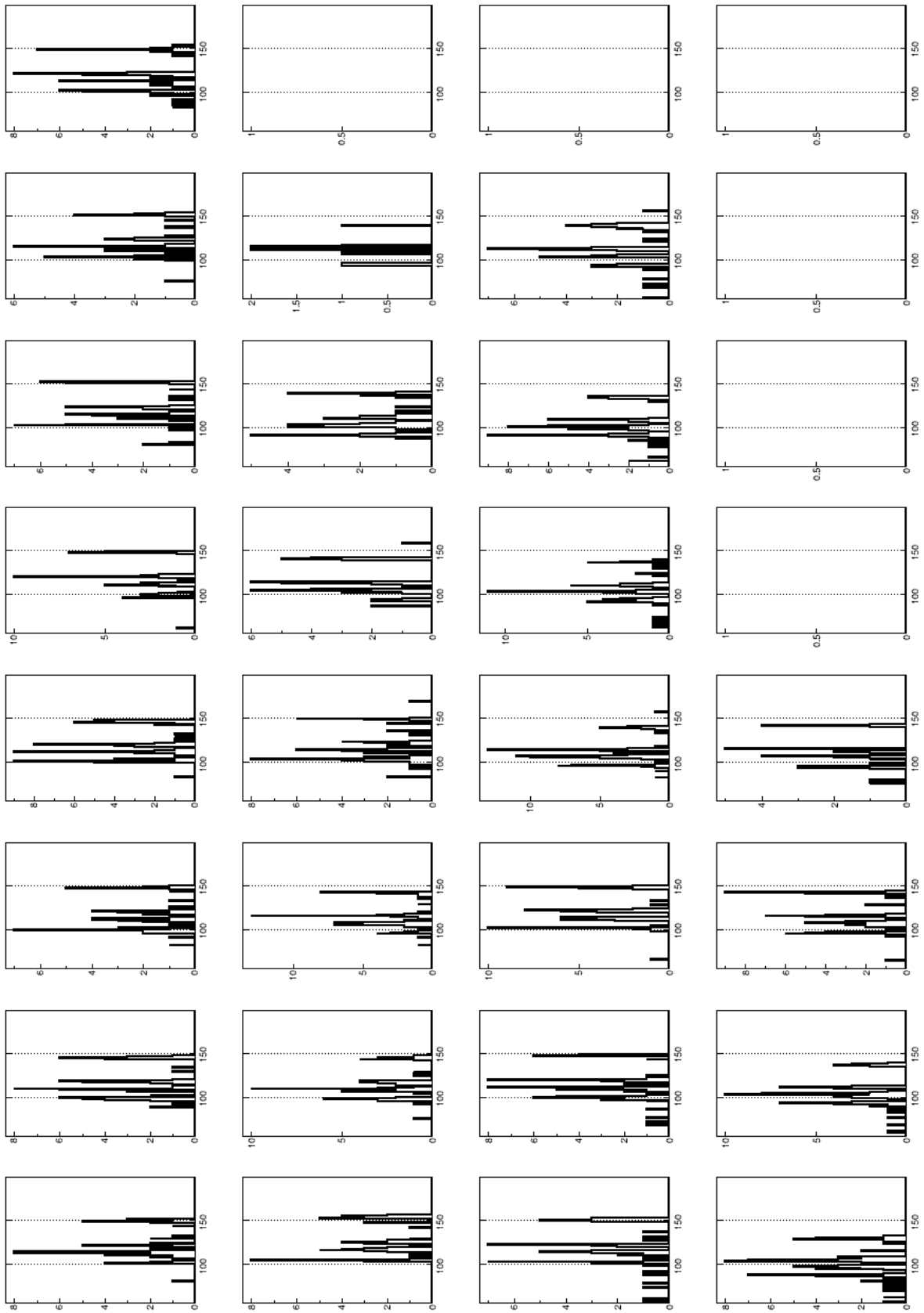

Figure A.4 – α energy recorded in each segment of quadrant 3 by using α-source ^{226}Ra.

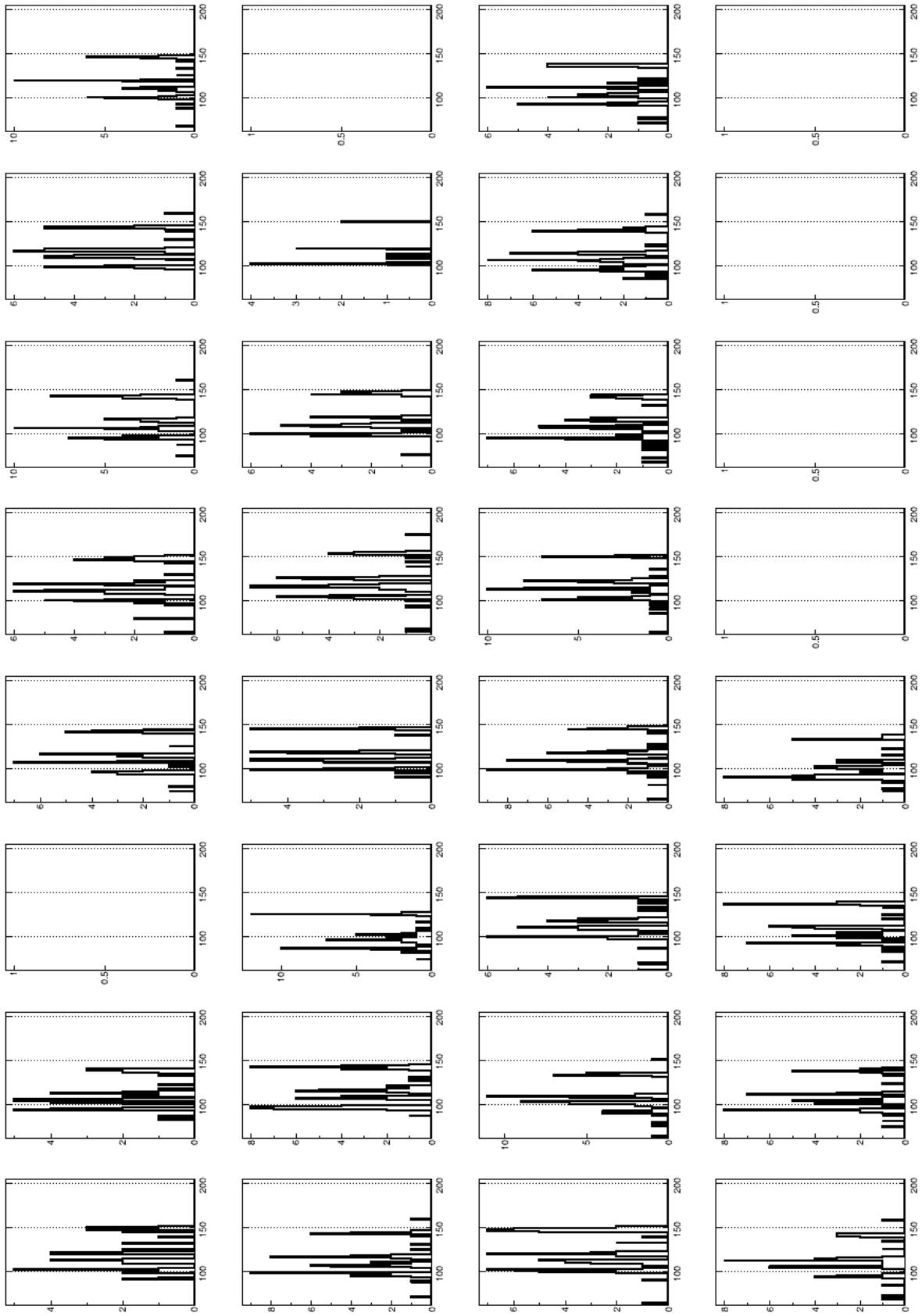

Figure A.5 – α energy recorded in each segment of quadrant 4 by using α-source ^{226}Ra.

A.3 Résumé en Français

Les atomes sont constitués d'un petit noyau massif, chargé positivement, entouré d'électrons qui gravitent autour du noyau à une distance cent mille fois supérieures à sa dimension. Les noyaux, au centre de l'atome, sont des systèmes quantiques avec un nombre Z de protons, un nombre N de neutrons et A = N + Z le nombre total de nucléons.

L'étude des données nucléaires, de plus en plus nombreuse et précise, confirme que certaines combinaisons de protons et de neutrons donnent des noyaux avec une très haute énergie de liaison. Les physiciens les appellent des noyaux magiques. C'est le cas des noyaux à 2, 8, 20, 28, 50, 82 ou 126 protons et/ou neutrons. Une explication de ces nombres magiques est donnée par une approche microscopique basée sur le modèle en couche, qui suppose que le noyau peut être décrit comme quelques nucléons de valence interagissant avec le champ moyen créé par un noyau inerte formé par les nucléons restants. De nombreuses données expérimentales qui ne pouvaient pas être expliquées par ce modèle de couches ont été comprises en considérant les noyaux comme un objet présentant des phénomènes collectifs. Néanmoins, le modèle en couche reste l'un des modèles essentiels utilisés pour la description des noyaux jusqu'aux masses intermédiaires. L'unification des modèles collectifs et du modèle en couche a été rendue possible par les travaux de Bohr et Mottelson, qui ont permis l'interprétation de phénomènes collectifs à partir des mouvements de particules uniques. Juste après les développements de la théorie microscopique de la supraconductivité de Bardeen, Cooper et Schrieffer, Bohr Mottelson et Pines ont finalement suggéré l'analogie entre le spectre du noyau et ceux du milieu supraconducteur, impliquant une composante d'appariement dans l'interaction entre les nucléons dans le noyau. Il est donc pertinent de s'intéresser à la manière dont les nucléons qui le composent interagissent les uns avec les autres. D'un point de vue théorique, une description microscopique de la structure et des réactions nucléaires est nécessaire à l'interprétation des nombreux phénomènes de la physique nucléaire.

La force fondamentale qui colle les nucléons ensemble provient de la théorie de la chromodynamique quantique (QCD), qui caractérise la forte interaction entre les nucléons. Cepen-

dant, la forme exacte de cette interaction n'est pas encore connue. En étudiant l'interaction nucléon-nucléon, on voit qu'elle se caractérise par une force répulsive à courte portée 0.4 fm (les nucléons sont maintenus à une certaine séparation moyenne) et par une force attractive au-delà de 1 fm. Dans ce cadre, des expériences de diffusion nucléon-nucléon ont été réalisées pour éclairer cette interaction. Les expériences de diffusion proton-deutons permettent de déterminer les propriétés de l'interaction nucléon-nucléon en dehors du milieu nucléaire, appelée aussi "interaction nue", dont nous savons qu'elle est différente de celle qui existe à l'intérieur du milieu nucléaire avec de nombreux nucléons. De plus, une description du noyau est basée sur le traitement du problème à N corps. L'utilisation de cette interaction nucléon-nucléon pour l'étude de la structure nucléaire est complexe, car les calculs se heurtent rapidement à des limitations théoriques et numériques en raison des nombreux degrés de liberté à traiter.

Actuellement, un modèle adéquat pour reproduire les phénomènes nucléaires, comprenant la description des états fondamentaux, des modes collectifs, ainsi que la description des réactions nucléaires, n'est pas encore bien établi. Pour les noyaux avec des masses moyennes à lourdes, les modèles les plus efficaces permettant de décrire la structure et la dynamique nucléaires sont la méthode de la densité d'énergie nucléaire (EDF), également appelée champ moyen autocohérent. Basé sur une énergie fonctionnelle empirique (par exemple Skyrme ou Gogny), il permet une description microscopique des mouvements collectifs de nucléons dans le noyau et lors de réactions nucléaires.
Les noyaux stables sur la vallée de stabilité dans la carte des nucléides montrent un certain rapport protons sur neutrons avec $N/Z \sim 1.0$ pour les noyaux plus légers. Les noyaux qui ont un excès de protons ou de neutrons sont instables et ces noyaux sont caractérisés par $N/Z > 1$. Les nucléides avec $N/Z >> 1$ sont appelés exotiques.

L'étude de ces noyaux est d'une importance capitale car leurs propriétés révèlent des caractéristiques nouvelles et inattendues qui contribuent à approfondir nos connaissances du système nucléaire. En effet, les mesures expérimentales ont mis en évidence l'affaiblissement de certains nombres magiques et l'apparition de nouveaux nombres magiques dans certaines régions de la carte des nucléides. L'une de ces régions se trouve à N = 20 autour de

^{32}Mg et on l'appelle "l'îlot d'inversion". Différentes expériences ont étudié les noyaux à N = 20 dans l'îlot de l'inversion, révélant une déviation de la systématique attendue, interprétée comme un signe d'une modification de la fermeture de la couche N = 20. Les mesures sur ^{32}Mg ont confirmé cette hypothèse. Ainsi, l'énergie du premier état excité est de 885 keV, ce qui est très faible par rapport à ce que l'on attend pour un noyau magique et suggère que le gap énergétique est soit affaibli, soit disparu. Pour cette raison, il est nécessaire de mesurer les propriétés nucléaires de base telles que les masses, la durée de vie nucléaire, les schémas d'excitation, les moments statiques et dynamiques. Ces propriétés peuvent être comparées à des modèles théoriques afin de tester ces modèles et d'améliorer l'efficacité des interactions théoriques.

L'interaction électromagnétique joue un rôle important dans l'investigation des noyaux. Une méthode très utile pour étudier les propriétés des noyaux, qui consiste à mesurer l'interaction de leur distribution de charge et de courant avec un champ électromagnétique externe bien connu. L'interaction électromagnétique est très bien comprise et nous permet donc de faire des mesures indépendantes du modèle. De plus, une "sonde" électromagnétique perturbe très peu le noyau car le champ électromagnétique a une faible influence sur les nucléons à l'intérieur du noyau.

La mesure d'un moment dipolaire magnétique (μ) implique soit la mesure de l'énergie d'interaction, (effet Zeeman), du moment magnétique interagissant avec un champ magnétique externe ou interne (hyperfine), ou de la précession d'un spin nucléaire (ou d'un moment dipolaire magnétique) aligné dans un champ magnétique. La quantité la plus souvent mesurée est le facteur g. Le facteur g et le moment dipolaire magnétique sont liés par $\mu = g \cdot I$ où I est le spin nucléaire. Le facteur g est un outil puissant dans l'étude des excitations nucléaires, car il est sensible à la configuration d'un état nucléaire avec une particule indépendante. Il révèle quelles sont les configurations et la position des orbites avec une particule indépendante, et peut-être utilisé comme une sonde rigoureuse pour explorer le caractère proton-neutron des états nucléaires.

Il y a quarante ans, les mesures du facteur g de l'état fondamental et des états isomères

n'étaient limités qu'aux noyaux stables ou aux noyaux proches de la ligne de stabilité β. Les noyaux proches de la ligne de stabilité β se situent généralement du côté de la vallée de stabilité où se trouve le déficit en neutrons, car la production des noyaux s'est principalement effectuée dans des réactions de fusion-évaporation. Au cours des deux dernières décennies, cette limitation a été surmontée par la création d'installations post-accélérateurs (telle que le CERN en Suisse) produisant des faisceaux d'ions radioactifs (RIB). Il est devenu possible d'explorer les régions du paysage nucléaire au-delà de la vallée de la stabilité.

Une mesure du facteur *g* sur des noyaux exotiques avec les RIBs est plus difficile que des mesures avec des faisceaux stables. L'intensité du faisceau du RIB est inférieure de plusieurs ordres de grandeur à celle des faisceaux stables. Cette faible intensité diminue le rendement en rayons gamma et augmente donc l'incertitude statistique de la mesure. Ce problème peut être compensé par l'utilisation des multi-détecteurs à haute efficacité offrant une couverture large en angle solide. De plus, les RIB peuvent être contaminés par des ions indésirables. La production et la sélection des noyaux exotiques d'intérêt en quantité suffisante ($> 10^6$ pps) ont permis de multiplier les tentatives de mesure du facteur *g* des noyaux d'intérêts. Par conséquent, des nouvelles méthodes ont été développées pour mesurer le facteur *g*. La mesure du facteur *g* d'un état est basée sur l'interaction de ce moment nucléaire avec un champ magnétique. L'effet se manifeste par une modification de la distribution angulaire du rayonnement associé. Plusieurs méthodes existent pour étudier le moment magnétique de l'état d'intérêt, en fonction de sa durée de vie. Dans cette thèse, deux techniques différentes sont utilisées:
- Le recul des ions dans le vide en fonction du temps (TDRIV) pour les états de courte durée (picosecondes),
- La distribution angulaire perturbée des rayonnements gamma en fonction du temps (TDPAD) pour les états ayant une durée de vie relativement longue (quelques ns ou plus).

Alors que les aimants de laboratoire peuvent fournir des champs magnétiques de l'ordre de Tesla pour les états isomères avec des durées de vie de centaines de ns ou plus, des champs magnétiques hyperfins sont nécessaires pour fournir des champs magnétiques puissants (quelques KTesla) pour les états avec des durées de vie de l'ordre de picoseconde. La méthode

TDPAD est utilisée pour mesurer le facteur g des isomères. Cette méthode a été largement utilisé dans les réactions de fusion-évaporation. La première expérience de démonstration de principe TDPAD avec une réaction de fragmentation, pour une énergie de faisceau E = 500 MeV/u, a été réalisée dans le cas de ^{43m}Sc. Une quantité importante d'alignement a été observée.

La première partie de ma thèse porte sur l'étude de l'orientation du spin nucléaire qui peut être produit par un mécanisme de réaction de fusion incomplète. Les processus de fusions incomplètes sont principalement les interactions entre ions lourds qui se produisent autour de la barrière Coulombienne. Les avantages de la fusion incomplète sont la population d'états à spin plus élevé, les états non-yrast, peu de canaux de réaction ouverts et un changement de Z entre le faisceau et les produits de la réaction.
Une expérience a été réalisée à ALTO à Orsay, en France. Le but de cette expérience était d'étudier l'orientation du spin nucléaire dans une réaction de fusion incomplète en utilisant un faisceau de ^{7}Li sur une cible de ^{64}Ni comme dans les réactions de transfert (^{7}Li, α pn) et (^{7}Li, α n). Dans ce cas, le niveau d'orientation du spin nucléaire a été déterminé en appliquant la méthode TDPAD aux états isomères dans le ^{65m}Ni et dans le ^{66m}Cu.

La deuxième partie de mon travail a été consacrée à la mesure du facteur g du premier état excité 2^+ dans les ^{28}Mg, ce qui indiquerait la position de l'orbite $\nu d_{3/2}$ à N = 16, définit la limite de la région de l'îlot d'inversion et imposer un test fort au modèle en couche dans cette région. Cette étude améliorera nos connaissances dans cette région et ouvrira la voie à des études similaires vers ^{32}Mg. L'expérience a été réalisée à HIE-ISOLDE au CERN. Un faisceau riche en neutrons de ^{28}Mg a été post-accéléré jusqu'à la plate-forme du MINIBALL, sur une cible de ^{93}Nb située dans une chambre à réaction au centre du spectromètre MINIBALL. L'état d'intérêt a été peuplé par l'excitation Coulombienne. Dans ce cas, le facteur g du premier état excité 2^+ dans ^{28}Mg a été étudié en appliquant la nouvelle méthode TDRIV, adaptée aux faisceaux radioactifs.

En utilisant un mécanisme de réaction de fusion incomplète, avec un faisceau stable de ^{7}Li atteignant une cible de ^{64}Ni, nous avons déterminé un degré élevé d'alignement de spin.

En appliquant une méthode de distribution angulaire perturbée en fonction du temps (TDPAD), on a obtenu une quantité d'alignement de spin: A = 14 (3)% pour ^{66}Cu et A = 26 (2)% pour ^{65}Ni. Ce résultat ouvre la voie à des mesures de facteur g avec un faisceau d'ions radioactifs guidés vers des cibles avec des masses légères, afin d'étudier la structure nucléaire de noyaux éloignés de la ligne de stabilité.

Le présent travail démontre également la faisabilité des mesures du facteur g des états 2_1^+ de courte durée. Sachant que la majorité des modèles théoriques sont basés sur la mesure de facteur g de l'état fondamental, le premier état excité permettra de tester ces modèles et d'appliquer un bon test sur la pureté de la fonction d'onde et sa configuration. Une méthode robuste appelée méthode de recul des ions dans le vide en fonction du temps (TDRIV) a été appliquée sur le premier état excité à ^{28}Mg, afin d'étudier la structure nucléaire N = 20 autour de l'îlot d'inversion, où le gap d'énergie entre les couches peut changer de manière significative en fonction du nombre de protons.
Les résultats de ce travail sur le ^{22}Ne permettent d'étalonner l'ensemble du système et de déterminer la distance absolue entre la cible et la feuille de dégradeur, ce qui permet de déterminer le facteur g dans ^{28}Mg avec une grande précision.

En résumé, nous avons validé une nouvelle méthode de mesure des facteurs g des états nucléaires excités ayant une durée de vie dans le régime de picoseconde. Les mesures sur des isotopes stables tels que ^{22}Ne peuvent atteindre de nouveaux niveaux de précision et tester le modèle nucléaire d'une manière qui n'était pas possible auparavant. Nous avons obtenu une valeur différente de $g(2_1^+)$ = 0,421 (36), par rapport à la valeur donnée dans la littérature $g(2_1^+)$ = 0,325 (30). Dans l'expérience précédente, la mesure du facteur g dans le ^{22}Ne a été déterminée à l'aide d'une méthode différente appelée champ transitoire (TF). Cette mesure nécessitait un champ transitoire beaucoup plus fort pour déterminer un facteur g avec une bonne précision. De plus, dans ce travail, le ^{22}Ne n'était utilisé que pour calibrer et tester le système avant l'utilisation du faisceau radioactif.

Sachant que la méthode TDRIV a été conçue pour une application aux faisceaux radioactifs, le présent travail est la preuve de l'application de cette méthode avec un faisceau radioac-

tif de ^{28}Mg. La première application réussie de la méthode TDRIV ouvre la voie à une future mesure sur le noyau riche en neutrons ^{32}Mg dans l'îlot d'inversion. Comme mentionné dans la section précédente, le facteur g de ^{22}Ne est différent de la valeur donnée dans la littérature. La valeur obtenue est inattendue et nécessite davantage d'investigations. Ensuite, les paramètres d'étalonnage obtenus à partir de la mesure du facteur g dans ^{22}Ne seront appliqués à l'analyse de ^{28}Mg afin d'en extraire le facteur g du premier état excité. La détermination du facteur g du premier état excité dans le noyaux ^{28}Mg est toujours sous investigation. Au cours de l'expérience et en raison de certaines difficultés techniques, les statistiques enregistrées étaient très basses pour le cas des ^{28}Mg et le facteur g devra être soigneusement déterminé.

Enfin, nous prévoyons d'utiliser le mécanisme de réaction de fusion incomplète en utilisant des faisceaux radioactifs pour étudier les propriétés des noyaux riches en neutrons dans la cinématique inverse.

université PARIS-SACLAY | ÉCOLE DOCTORALE PHENIICS

Titre : Étude de l'orientation du spin nucléaire dans les réactions de fusion incomplète. Mesure du moment magnétique des états 2^+ dans les noyaux ^{22}Ne et ^{28}Mg.

Mots clés : Structure des noyaux exotiques, Techniques TDRIV & TDPAD, Moment magnétique nucléaire.

Résumé : La mesure des moments magnétiques nucléaires est d'une grande importance pour bien comprendre la structure nucléaire. Le moment magnétique est sensible à la nature de la particule indépendante. Le développement des faisceaux radioactifs post-accélérés permet aujourd'hui d'étudier les moments magnetiques des niveaux excités des noyaux exotiques éloignés de la ligne de stabilité. Cependant, la mesure des moments magnétiques des noyaux radioactifs nécessite le développement des nouvelles méthodes fiables. Le développement réussi de telles méthodes ouvrirait la possibilité de découvrir de nouveaux phénomènes de structure nucléaire.
L'étude présentée dans cette thèse est formée de deux expériences. La première expérience a été réalisée à ALTO à Orsay, en France. L'une des principales exigences pour mesurer un moment magnétique nucléaire est de produire un ensemble avec des spins orientés. Ce dernier peut être produit par un mécanisme de réaction approprié et une interaction de spin nucléaire avec le milieu environnant. Le degré d'orientation dépend du processus de formation et du mécanisme de réaction. Le but de cette première expérience était d'étudier le niveau d'orientation du spin nucléaire dans un mécanisme de réaction de fusion incomplete. Le résultat de l'expérience démontre la possibilité d'obtenir un alignement du spin dans une réaction de fusion incomplète d'un ordre de 20%. Ce mécanisme de réaction, avec une telle quantité d'alignement de spin, a le potentiel d'étudier la région riche en neutrons avec des faisceaux radioactifs. La deuxième expérience, et l'essentiel de la thèse, a été réalisée à HIE-ISOLDE au CERN. Cette expérience visait à obtenir des informations de haute précision sur le facteur g d'un état de courte durée. Une nouvelle méthode TDRIV (Time-Differential Recoil In Vacuum) a été appliquée pour la première fois avec des faisceaux radioactifs post-accélérés. Le faisceau de ^{22}Ne a été utilisé pour calibrer le système, ainsi qu'avec son facteur g connu du premier état excité permet de déterminer la distance absolue entre la cible et le dégradeur. Les résultats et la procédure d'analyse détaillée sont présentés, et seront utilisés pour déterminer le facteur g du premier état excité dans un noyau de ^{28}Mg (E_x = 1474 (1) keV, $T_{1/2}$ = 1,2 (1) ps).

Title : Study of the nuclear spin-orientation in incomplete fusion reactions. Measurement of the magnetic moment of the 2^+ states in ^{22}Ne and ^{28}Mg.

Keywords : Structure of exotic nuclei, TDRIV and TDPAD techniques, Nuclear magnetic moment.

Abstract : Knowledge of the nuclear magnetic moments is of great importance for understanding of nuclear structure. Since they give access to the nuclear wave function. Thus, the magnetic moment is sensitive to the single-particle nature of the valence nucleons. The development of radioactive beam facilities allows nowadays studying nuclear spins and moments of nuclei with extreme isospin, which are far from the stability line. However, this measurement requires the development of more sensitive methods to discover new nuclear structure phenomena. One of the main requirements in order to measure a nuclear magnetic moment is to produce a spin-oriented ensemble. The latter can be produced by suitable reaction mechanism and nuclear spin interaction with the surrounding environment. The degree of the orientation depends on the formation process and reaction mechanism. The study outlined in this thesis is formed by two experiments. The first experiment was performed at ALTO facility in Orsay, France. The aim was investigating the level of nuclear spin orientation from the incomplete fusion reaction mechanism. Two reaction channels were studied: the isomeric states in ^{65m}Ni ($I^\pi = 9/2^+$, E_x = 1017 keV, $T_{1/2}$ = 26 ns) , and^{66m}Cu ($I^\pi = 6^-$, E_x = 563 keV, $T_{1/2}$ = 600 ns) with the Time-Dependent Perturbed Angular Distribution (TDPAD) method. The result of the experiment demonstrates the possibility of obtaining a large spin alignment of order of $\sim$ 20 %. This reaction mechanism, with such an important amount of spin alignment has potential near radioactive beam facilities to study the neutron-rich region with inverse kinematics reactions. The second experiment, which consitutes the main part of the thesis, was performed at HIE-ISOLDE at CERN. This experiment aimed to obtain high precision g-factor information on a very short-lived picosecond state. The Time Differential Recoil-In-Vacuum (TDRIV) method was applied for the first time using post-accelerated radioactive beams. The g-factor measurement was performed for the first-excited state in ^{28}Mg (E_x = 1474(1) keV, $T_{1/2}$ = 1.2(1) ps). Since the lifetime of the state is of the order of picoseconds, its g-factor can be measured only via the spin precession of the nucleus in an extremely strong magnetic field (kT). Such fields can only be produced at the nucleus by hyperfine interactions. In order to obtain a high precision on a g-factor measurement, a TDRIV calibration experiment was performed with a stable ^{22}Ne beam. Using the known g-factor of the first-excited state in ^{22}Ne allows to determine the absolute target-to-degrader distance. The results and detailed analysis procedure are presented, and will be used to determine the g-factor of 2^+ state in ^{28}Mg from the recorded data.

Université Paris-Saclay
Espace Technologique / Immeuble Discovery
Route de l'Orme aux Merisiers RD 128 / 91190 Saint-Aubin, France